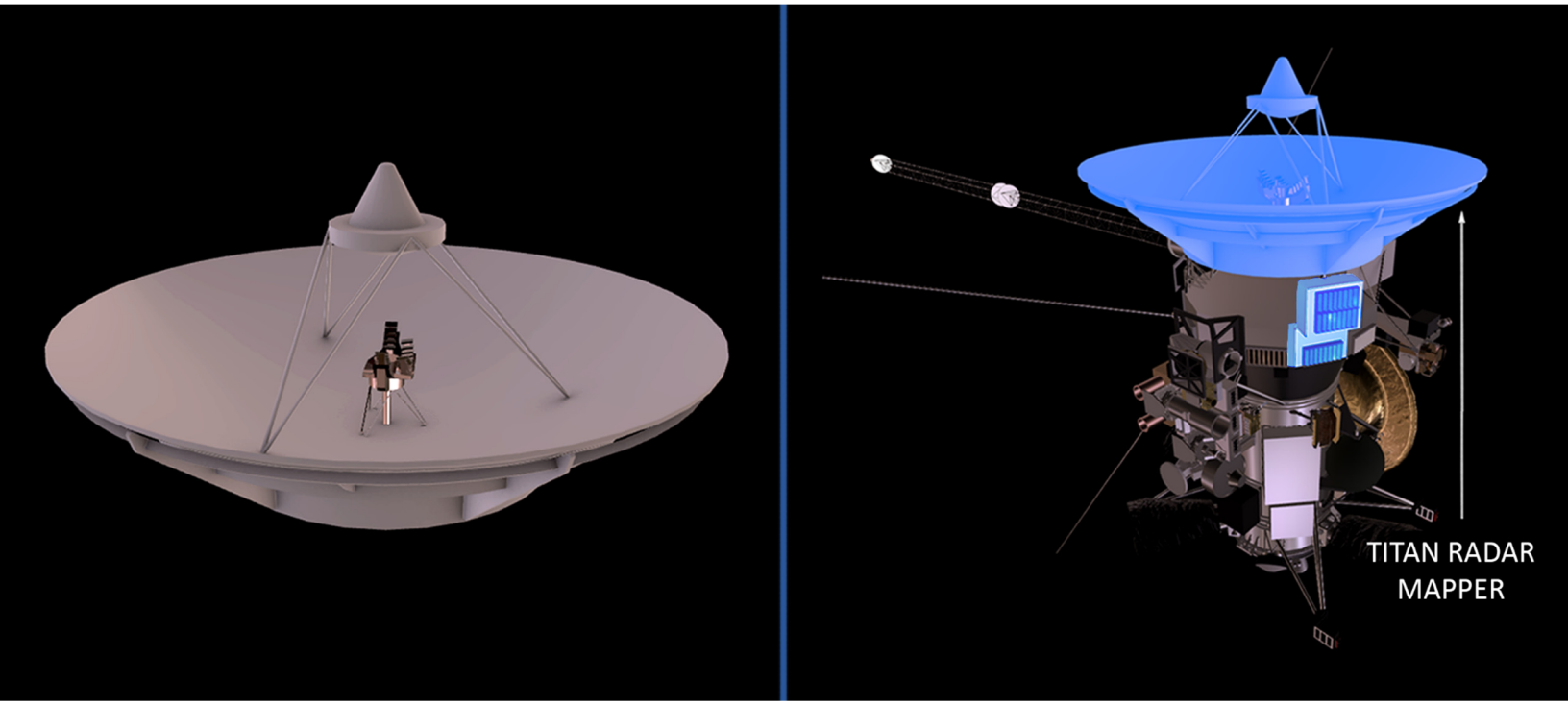

TITAN RADAR MAPPER

The Titan Radar Mapper (RADAR) Instrument investigated Saturn, its rings and moons, but it was primarily built to study Saturn's moon Titan, which has a thick atmosphere that hides its surface. The **science objectives** of RADAR were to perform Synthetic Aperture Radar (SAR) imaging, altimetry, scatterometry, and radiometry of Titan's surface to determine the distribution of lakes and seas, investigate the geologic features and topography of the solid surface of Titan, and acquire data on non-Titan targets (Saturn, rings, icy satellites). RADAR bounced radio waves at microwave frequencies off Titan's surface, and created images of the surface by recording slight differences in the reflected signal's arrival time and wavelength back at the spacecraft. RADAR detected how smooth or rough surfaces are, making it useful for studying Titan's methane seas.

The RADAR used the spacecraft's high-gain antenna (HGA) and its associated five-beam Ku-band feed assembly to send radar transmissions (at a wavelength of 2.2 cm, equivalent to a frequency of 13.8 GHz) toward targets and capture reflected radar signals and blackbody radiation. In its altimetry mode, the RADAR could also measure the height profile of terrain beneath the spacecraft.

CONTENTS

Figures

Tables

EXECUTIVE SUMMARY

Throughout the Cassini mission, Titan Radar Mapper (RADAR) obtained Synthetic Aperture Radar (SAR) images, altimetry, scatterometry, and (passive) radiometry of Titan, Saturn, some of the icy satellites, and Saturn's rings. Over the course of the mission, the Radar Science Team planned, commanded, processed, and archived these datasets. Taken together with other Titan-observing Cassini instruments' data, their analysis has produced many scores of discoveries: we have revolutionized our understanding of Titan, which despite its low temperatures has shown its surface to be unexpectedly Earth-like, both in terms of observed features and the geologic processes that formed them. These include mountains, sand dunes, oceans and lakes, rivers, and a complex hydrologic system where the working fluid is primarily methane. Analysis of repeat SAR coverage was a major contributor to the conclusion that there is a subsurface ocean within Titan. Radar observations of Saturn have improved microwave observations by nearly an order of magnitude and revealed deeper structure than was previously thought possible. Icy satellite data have been used to explore hemispheric dichotomies or regional anomalies and, where higher spatial resolution was possible, to examine specific areas of interest—in particular of Enceladus. Microwave scans of Saturn's rings suggest that particles in the A-ring, B-ring, and C-ring may be highly porous, and that the rings may be very young—perhaps less than 150 million years. Both passive and active radar data from Cassini's last orbits of Saturn, still under analysis, promise to provide new information about particle size distribution and its variation across the rings.

Radar observations of Saturn have improved microwave observations by nearly an order of magnitude and revealed deeper structure than was previously thought possible.

To rank the team's discoveries is difficult, both because of their wide variety and because discoveries often involve analyses of more than one instrument's data. After some debate we have developed these top ten major new facts resulting at least in part from radar data. The body of this report explains these in detail.

1. Titan's surface is dynamic and Earthlike, with an active hydrological cycle that includes several large seas, hundreds of lakes, and numerous rivers and channels.

2. Titan's surface is relatively young, perhaps hundreds of millions of years, with few impact craters identified.

3. A band of linear sand dunes, likely made of organic material, stretches across most of Titan's equator.

4. Titan's seas have depths of 100s of meters; the liquid in them is remarkably pure methane-ethane-nitrogen.

5. A large, previously identified feature known as Xanadu is not elevated relative to surrounding terrain as previously suspected. It seems to be younger and rougher than the rest of Titan and it likely has a high content of highly fractured water ice bedrock.

6. Titan is internally differentiated, and has an outer ice shell, a subsurface ocean, a high pressure layer at the base of the ocean, and a deep rocky interior.

7. Liquid is transported from one Titan hemisphere to the other, resulting in more lakes that are currently dry in the south.

8. Cryovolcanism exists or has recently existed on Titan. Several surface features have been identified as likely cryovolcanic vents.

9. By probing its ammonia at depth, radiometric data have revealed deeper structure in Saturn than was previously thought possible.

10. The south pole of Enceladus has the brightest radar backscatter of any planetary surface in the solar system, suggesting a retroreflective near surface, for reasons that remain puzzling but appear to be linked in some way to the presence of the E-ring.

RADAR Instrument Summary

The Titan Radar Mapper (henceforth RADAR[1] [Elachi et al. 2004]) was one of twelve instruments aboard the Cassini spacecraft. It was developed by NASA's Jet Propulsion Laboratory (JPL), the Italian Space Agency (ASI), and the Cassini Radar Science Team, primarily to reveal the surface of Titan but also to explore Saturn, its rings and the icy satellites. Nearly opaque at most visible and near-infrared wavelengths, Titan's atmosphere is transparent at RADAR operating wavelength of 2.17 cm (Ku-band). RADAR had four operating modes: SAR imaging, altimetry, scatterometry, and radiometry. In its SAR mode, used at altitudes under ~4,000 km, RADAR imaged surfaces of Titan and Saturn's icy satellites and rings in various modes, including SAR at incidence angles from 15 to 35 degrees and spatial resolutions varying as low as 350 m, sufficient to identify major structures and to make geologic maps. SAR images characterize the surface roughness at scales near the radar wavelength, to surface slopes at the scale of the radar resolution, and to dielectric properties of the constituent materials. In addition, microwaves can penetrate many wavelengths into some materials on Titan. But for the most part, SAR images are observationally similar to optical images and allow us to identify major structures and geomorphologic units. Altimetry results when the antenna is pointed within a fraction of a beam width (0.35 deg) of nadir resulting in a range resolution of approximately 30 m and spatial resolution depending on altitude. The altimetry data have two broad applications. First, the aggregate of all data define an absolute geoid for Titan and constrain any rotational or tidal bulge. Second, relative topographic profiles from each RADAR

[1] In this report, we distinguish radar, a microwave sensing technique, and RADAR, an instrument aboard the Cassini spacecraft.

pass characterize landforms (e.g., impact craters, mountains), yielding important constraints on geophysical models. Altimetry was obtained over 2% of Titan's surface, in some cases measuring the depth and absorption of liquids.

An amplitude monopulse comparison technique called SARTopo [Stiles et al. 2009] added an additional 5% topographic coverage using SAR data [Corlies et al. 2017]. The SARTopo technique depends on the precise manner in which the location and magnitude of each SAR pixel are affected by variation in surface height between each of the five antenna beams (feeds) [Elachi et al. 2004]. The technique estimates surface heights from observed differences between beams. Cassini's antenna had multiple beams, so that some points on the ground were observed from two different beams. For different beams, the mislocation error due to surface height is the same, but the miscalibration error is different and of opposite sign. Nonzero surface heights, therefore, result in apparent differences in pixel positions between overlapping single beam SAR images. In addition, altimetry was able to obtain depths of several lakes and seas [Mastrogiuseppe et al. 2014]. Scatterometry is obtained by pointing the transmitter off-nadir, but processing the echoes using the real aperture rather than the synthetic aperture. The data indicate the backscatter efficiency at various incidence angles at relatively low resolution (real aperture resolution depends on range to

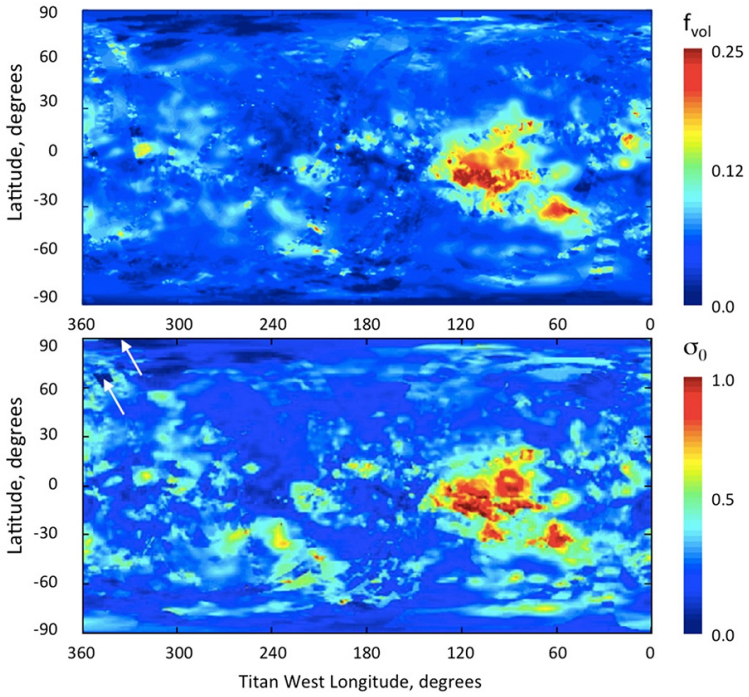

Figure RADAR-1. Predicted and observed maps of scattering from Titan's surface. The upper panel is a map of the volume scattering parameter f_{vol} for a simple surface model composed of a smooth dielectric interface separating free space from an inhomogeneous and isotropically scattering subsurface. The f_{vol} is the probability that a photon entering the surface (as determined by the effective dielectric constant) scatters and escapes from the subsurface before it is absorbed. The map of f_{vol} reconciles the maps of effective dielectric constant and emissivity and predicts the overall magnitude of the scattering. The lower panel is a global mosaic of Titan's normalized radar cross-section from all real aperture data through T71 [Wye 2011], showing the actually observed scattering. The white arrows in the upper left-hand corner indicate two small regions that were not mapped.

surface). Scatterometry coverage is near-global (Figure RADAR-1); it can be used as a basemap for SAR and as a broad characterization of global terrains. As an independent constraint on surface roughness, scatterometry data are an important complement to radiometry data in order to constrain surface composition. Used as a passive microwave radiometer, RADAR collected near-global measurements (Figure RADAR-2) of Ku-band brightness temperature with an accuracy of 1 K [Janssen et al. 2016]. Radiometry data produce polarized brightness temperatures of the observed scene, obtained from the antenna temperature measurements. The microwave brightness temperature of a solid surface depends on many properties besides physical temperature; e.g., emission angle, polarization, dielectric constant, porosity, surface, and subsurface roughness, etc.

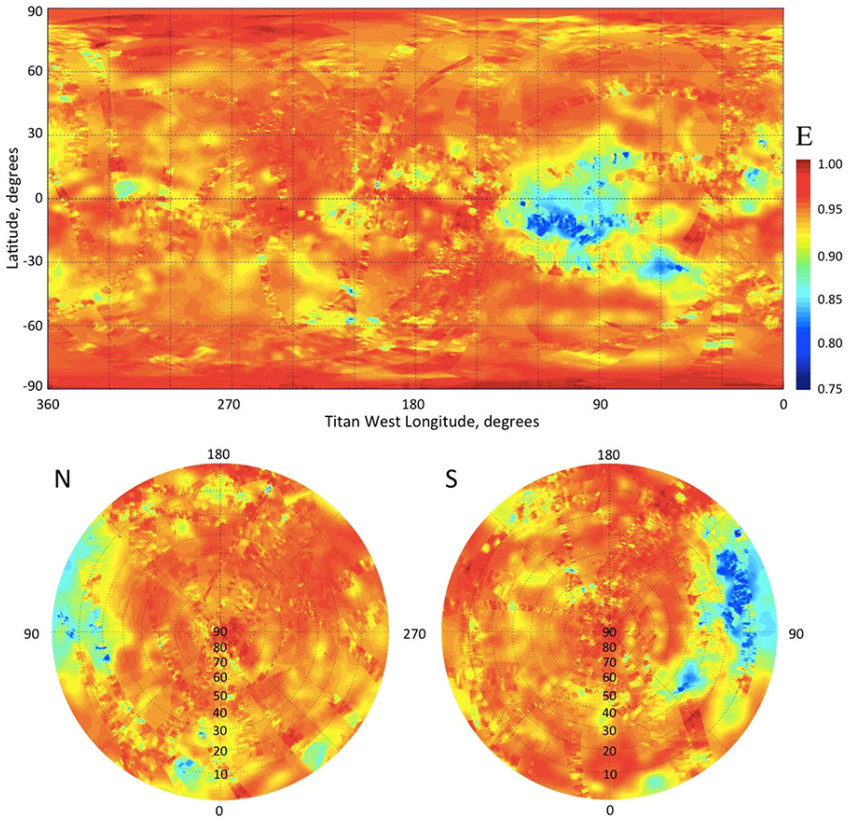

Figure RADAR-2. Global mosaic of emissivity of Titan at the 2 cm wavelength of the Cassini RADAR. This is the final result of the brightness temperature mapping of Titan incorporating all radiometric data obtained from Titan passes, a nearly 10-year span. The brightness temperature was measured as a function of position, polarization and time over a wide range of geometries and ranges, and calibrated to about 1% absolute accuracy using Huygens probe and Composite Infrared Spectrometer (CIRS) temperature measurements as described in Janssen et al. [2016]. The polarization data were used to construct a global mosaic of effective dielectric constant, enabling the conversion of all measured brightness temperatures to their equivalent values at normal incidence. The data were then folded into a massive least-squares solution for the seasonally varying brightness temperature distribution of Titan over the time scale of the observations. Comparison with surface temperature measurements obtained in the infrared (IR) using Kirchhoff's law then enabled the construction of the emissivity map shown. Note that Xanadu, the equatorial region centered on 100 W longitude, is extremely cold and non-emissive, characteristic of a high content of highly fractured water ice bedrock.

KEY OBJECTIVES FOR RADAR INSTRUMENT

The key RADAR science objectives are listed below, and discussed in further detail in the section entitled RADAR Science Results.

Titan Science

Surface units

TN1a: Determine the types, composition, distribution, and ages of surface units and materials, most notably lakes (i.e., filled vs. dry & depth; liquid versus solid & composition; polar versus other latitudes and lake basin origin).

CSM: T_AO4: Titan surface characteristics and internal structure—determine the physical state, topography, and composition of the surface; infer the internal structure of the satellite.

TC1a: Determine seasonal changes in the methane-hydrocarbon hydrological cycle—of lakes, clouds, aerosols, and their seasonal transport.

Internal structure

TN1b: Determine internal and crustal structure—liquid mantle, crustal mass distribution, rotational state of the surface with time, intrinsic and/or internal induced magnetic field.

TN2b: Determine icy shell topography and viscosity.

TN2c: Determine the surface temperature distribution, cloud distribution, and tropospheric winds.

Saturn Science

SN1b: Observe the aftermath of the 2010–2011 storm. Study the life cycles of Saturn's newly discovered atmospheric waves, south polar hurricane, and rediscovered north polar hexagon.

Ring Science

RN1c (R_AO2): Determine structural and compositional variations at high resolution across selected ring features of greatest interest, using remote and in situ observations.

Icy Satellite Science

IN1a: Determine the presence of an ocean at Enceladus as inferred from induced magnetic field and plume composition, search for possible anomalies in the internal structure of Enceladus as

associated with plume sources, and constrain the mechanisms driving the endogenic activity by in situ observations and remote sensing.

IN1c: Determine whether Dione exhibits evidence for low-level activity, now or in recent geological time.

I_AO1: Icy satellite geology and history—determine the general characteristics and geological histories of the satellites.

RADAR Science Assessment

Table RADAR-1 contains an assessment of RADAR science based on the objectives in the original Announcement of Opportunity (AO) and the Cassini Traceability Matrix (TM) developed for the Equinox and Solstice missions.

Table RADAR-1. Matrix of RADAR science objectives. Green color indicates that RADAR data with sufficient quality were obtained during the Cassini mission to contribute to a given science objective.

RADAR Science Objectives	AO and TM Science Objectives	RADAR Science Assessment	Comments
Titan Science			
Surface units	TN1a, CSM:T_AO4, TC1a		
Internal structure	TN1b, TN2b, TN2c		
Saturn Science	SN1b		
Icy Satellite Science			
Enceladus plumes	IN1a		
Dione	IN1c		Data acquired, not yet analyzed
Satellite geology and history	I_AO1		
Ring Science	RN1c (R_AO2)		

RADAR Science Results

Titan Science

In its 13-year presence at Saturn, Cassini made a total of 127 passes by Titan, some as close as 950 km. Forty-eight of these were used by RADAR, with one lost in downlink—for a detailed description of results from individual flybys, see Lorenz et al. [2018]. SAR coverage was limited by both Cassini's orbital path, which used Titan for gravity assists, and by intense competition among instruments for observation time—resulting in a seemingly random set of strips 100–200 km wide (Figure RADAR-3). However, the swaths were well distributed in latitude and longitude, allowing for an emerging global picture of the surface. Aerial SAR coverage at the end of the mission was

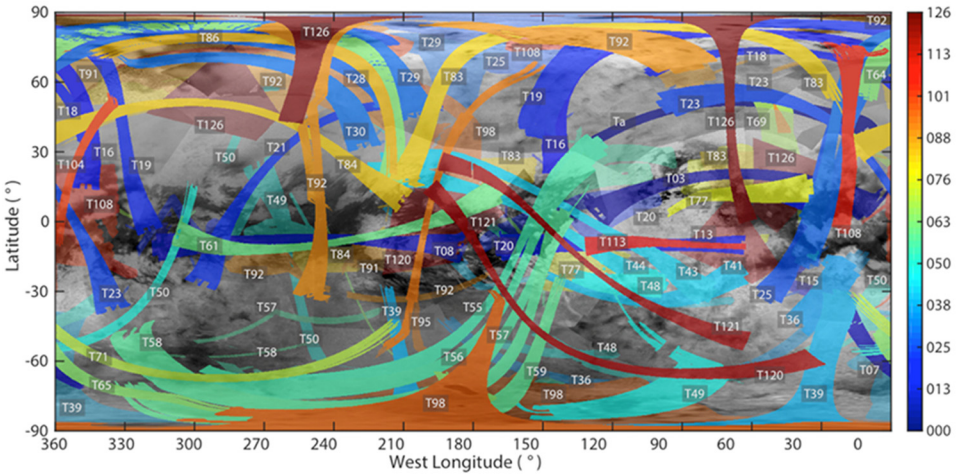

Figure RADAR-3. Combined Titan SAR coverage from the entire Cassini mission. Swaths are shown over an ISS basemap.

46% using nominal SAR mode and 74% including coarser-resolution (>1.5 km) HiSAR. Repeat images were obtained over 14% of the surface, and 1.5% was covered four or more times [Lorenz et al. 2018]. Real-aperture scatterometry and passive radiometry data exist over the entire surface, at varying resolutions.

Together with near-infrared and mid-infrared images taken by other Cassini instruments—Visual and Infrared Mapping Spectrometer (VIMS) [Brown et al. 2004] and the Imaging Science Subsystem (ISS) [Porco et al. 2004]—RADAR has given us an opportunity to discover a new world that is both Earth-like and unearthly. We find familiar geomorphology in its mountains, dunes, rivers, and seas, but note that these features are composed of unfamiliar materials. In this section, we review RADAR's contributions to geology, hydrology, and surface-atmospheric interaction in an attempt to summarize our knowledge of Titan at the end of the Cassini mission.

Interior

Static and time-varying gravity field measurements [Iess et al. 2010, 2012], rotational dynamics measurements [Stiles et al. 2008, 2010; Lorenz et al. 2008a; Meriggiola et al. 2016], and shape models [Zebker et al. 2009a; Mitri et al. 2014; Corlies et al. 2017] have been used to infer the interior structure of Titan. Magnetic field measurements have shown that an intrinsic magnetic field is not present on Titan [Wei et al. 2010]. The determination of the rotational dynamics from Cassini RADAR SAR images has been key to constraining the interior structure of Titan. As described in the previous section, Cassini RADAR SAR coverage of Titan is dependent on orbit dynamics and competition for observation time. As a result, SAR swaths appear somewhat randomly distributed with coincidental overlaps (with only a few exceptions). Where overlap occurs, and assuming that the same surface features appear in both images, it is possible to determine how quickly Titan has rotated between observations and thus estimate Titan's pole location and spin rate [Stiles et al. 2008, 2010], analogous to previous work using Magellan SAR imagery to estimate the spin model of Venus [Davies et al. 1992]. First, a set of recognizable landmarks observed in two different SAR

images are obtained at different times located in a Titan centered inertial, non-rotating (J2000) reference frame. Pixels chosen in each SAR image corresponding as closely as possible to the same point on the landmark are aligned, using several techniques to minimize landmark mismatches. The spin state parameters are estimated by minimizing the misregistration error—that is, the apparent movement in Titan body-fixed coordinates of the landmarks between observation times. Feature mapping is much more robust for radar than for passive optimal imagery, because radar geolocation is independent of spacecraft pointing knowledge except that the general direction (within 10 degrees or so) must be known to exclude mirror ambiguities. Accurate radar pixel locations in inertial space depend only on the accuracy of the measurement of delay, Doppler shift, spacecraft velocity and position, and presumed target body topography. Nearby SARTopo [Stiles et al. 2009] measurements of topography help determine more precisely variations in feature locations in inertial space. Using similar methodology and a more extensive set of observations, Meriggiola et al. [2016] also provided a rotational model of Titan estimating the spin pole location, the spin rate, the precession, and the nutation. Further, these authors show that the pole location is compatible with the Cassini State 1 (a dynamical equilibrium wherein the spin axis, the orbit norma,l and the normal to the invariable plane are coplanar).

Stiles et al. [2008] and Meriggiola et al. [2016] have provided an estimate of Titan's obliquity (0.31°). The obliquity together with the quadrupole moment of the gravity field (J2 and C22) measurements [Iess et al. 2010, 2012] constrain the moment of inertia of Titan. These results were used by Bills and Nimmo [2011] to estimate the radial mass distribution of Titan and, when combined with the low-degree gravity field derived from Cassini spacecraft Doppler tracking data [Iess et al. 2010], suggest that Titan's outer shell is mechanically decoupled from the deeper interior. Bills and Nimmo [2011] and Meriggiola et al. [2016] find that the estimated obliquity is compatible with a deep interior decoupled from the outer ice shell by a global subsurface ocean. Note that Lorenz et al. [2008a] interpreted the initial indication in Stiles et al. [2008] of nonsynchronous rotation as indicating a subsurface ocean, drawing on predictions of atmospheric angular momentum exchange with a decoupled shell by Tokano and Neubauer [2005]. However, the spin state determination has significant degeneracy between nonsynchronous rotation and precession of the spin pole, and subsequent observations seem to favor synchronous rotation. Thus, the conclusion of Lorenz et al. [2008a] of an internal global ocean indicated by RADAR spin measurements remains correct, but for perhaps the wrong reasons. The presence of a subsurface ocean inferred from the rotational dynamics of Titan is consistent with the large tidal response of Titan (tidal Love number $k_2 = 0.589 \pm 0.150$) [Iess et al. 2012; Mitri et al. 2014]. In agreement with this scenario, the Permittivity, Wave and Altimetry (PWA) instrument on board Huygens' probe measured a Schumann-like resonance, also suggesting the presence of a subsurface ocean [Bèghin et al. 2012]. In summary, the gravity, topography and rotational dynamics measurements in combination with thermal-evolution models indicate that Titan is internally differentiated (Figure RADAR-4), and has an outer ice shell, a subsurface ocean, a high pressure layer at the base of the ocean, and a deep rocky or rock-ice mix interior [Hemingway et al. 2013; Mitri et al. 2014; Tobie et al. 2014].

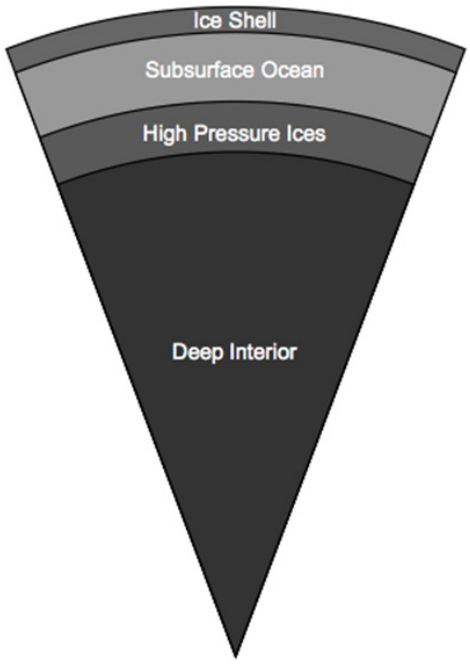

Figure RADAR-4. Possible present-day structure of Titan's interior showing that Titan is internally differentiated with a deep rocky or rock-ice mix core.

Global shape

RADAR observations using both the altimetry and SARTopo modes reveal Titan's global shape and yield insights to its interior structure. The roughly 60 satellite-derived elevation surface traces—Figure RADAR-5 [Zebker et al. 2009a]—show that Titan's polar radius is less than, and the equatorial radii are greater than, predicted by its gravity field. Best-fitting solutions are shown in Table RADAR-2.

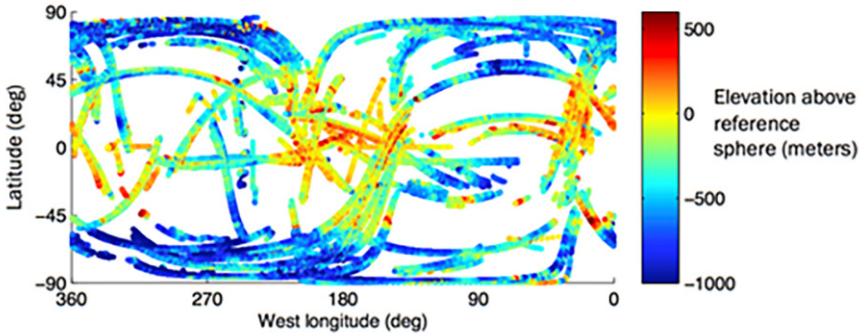

Figure RADAR-5. Cassini measurements of Titan surface height above a reference sphere of 2575 km radius. As expected, the shape is dominantly triaxial ellipsoidal, with topographic lows near the poles and topographic highs at the prime-meridians and anti-meridians. However, the polar flattening is greater than expected for a hydrostatic body, meaning the equatorial topography stands higher than expected and the polar depressions are lower than expected, suggesting that the depth to the subsurface ocean is smaller at the poles than at the equator.

Table RADAR-2. Titan gravity and shape triaxial ellipsoids (m).

	Gravity	Elevations	Difference
a axis	2574875 ± 7.3	2575124 ± 26	−249
b axis	2574716 ± 7.4	2574746 ± 45	−30
c axis	2574660 ± 4.5	2574414 ± 28	246
a translation	0.8 ± 5.6	69.8 ± 6.2	
b translation	0.1 ± 5.6	68.3 ± 8.0	
c translation	1.7 ± 3.9	45.8 ± 6.4	
Mean eq. rad.	2574795	2574761	−34
Hydrostatic ratio (a-c)/(b-c)	3.83	2.14	

The hydrostatic ratio (a-c)/(b-c), which is exactly 4 for a spin-locked satellite in hydrostatic equilibrium, for Titan's figure is observed to be only 2.14 [Zebker et al. 2009a; Corlies et al. 2017]. The hydrostatic ratio obtained from the third-degree gravity observations is 3.83—that is, the gravity field reflects approximate hydrostatic equilibrium. While the gravity field is consistent with a hydrostatically relaxed body, Titan's figure is not. If both of these data constraints pertain, Titan's interior does not conform to a set of spherically symmetric shells, as these data imply that the average satellite density at the equator is less than at the poles. If Titan has a vast interior ocean of liquid water, then some ice layers (less dense than liquid water) are thinner at the poles than the equator. A simple model satisfying both sets of data and assuming isostatic compensation (Figure RADAR-6) could be the result of uneven heat dissipation in Titan's interior, such as may result from tidal interaction with Saturn or its other moons.

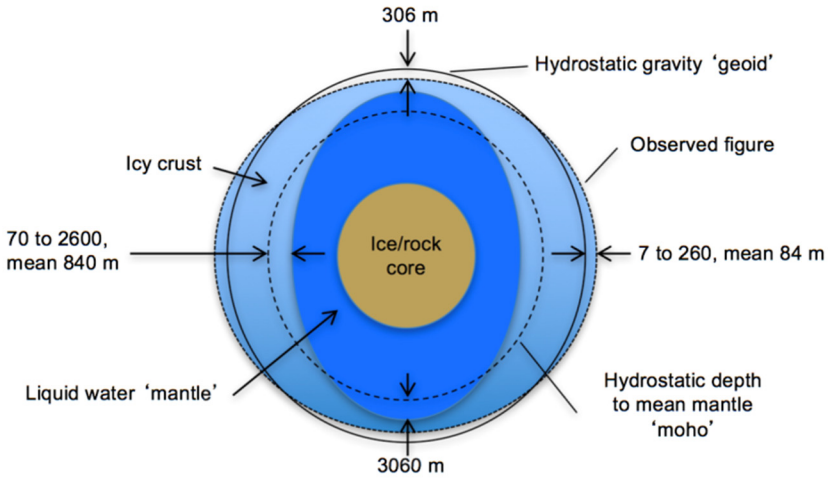

Figure RADAR-6. Model consistent with Cassini gravity and figure measurements, assuming isostatic compensation. The thinner ice shell (exaggerated for visibility in the figure) at the poles could result from uneven heat dissipation within Titan from tidal interactions, and the relatively shallower geoid at the poles is one explanation for the preponderance of lakes at the most northern and southern latitudes. The shallower geoid allows mobile liquids to lie closer to the surface.

Another simple model explaining the overly oblate topographic figure assumes that there is greater precipitation of hydrocarbon snow or loosely packed hydrocarbon particulates at the equator than at the poles, perhaps with a net equatorward transport from the poles, which would also be consistent with the data. This could account for increased distance from the surface to the planet center at the equator if sufficient material were so transported. We note that this is consistent with the observation of 100 m tall dune structures near Titan's equator (see the section entitled Dunes), so that poorly consolidated material may indeed collect there to a greater extent. Several hundred meters of deposition at the equator would match the mean equatorial radii of both models, but precipitation would have to preferentially occur in the sub- and anti-Saturnian directions, which seems unlikely.

Further comparisons of the gravity and shape observations constrain the depth of any outer ice shell enclosing a global subsurface ocean [Zebker and Wong 2016]. While the exact value varies depending on how the spherical expansion is constrained, the observed gravity to topography ratio is 0.070 for the third order terms and 0.042 for fourth order [Zebker and Wong 2016]. These imply ice shell thicknesses of 327 and 187 km, respectively, a factor of ≥2 more than the 100 km expected from thermal models [Sohl et al. 2003; Nimmo and Bills 2010]. The Zebker and Wong solution yields a tidal Love number h_{2t} of about 0.5, and a basal heat flow of 2.5 mW/m^2. This would suggest that heat from Titan's core is lower than often assumed, hence the amount of radiogenic material in the core is likely less as well. These data also constrain the depth of Titan's mantle and density of its core, placing added restrictions on its composition and evolution. Supposing that Titan has an undifferentiated ice/rock core beneath the ocean, and that the moment of inertia is most likely in the range 0.33–0.34 [Iess et al. 2010], then a 200 km crust estimate from above and Titan's well-known mean density of 1.88 g cm^{-3} implies an ocean depth and core density ranging from 308 km and 2.74 g cm^{-3} (MOI = 0.33), to 226 km and 2.55 g cm^{-3} (MOI = 0.34).

The Cassini-Huygens mission has revealed the surface of Titan in unprecedented detail, enabling us to discern different geomorphological units on the surface … .

Composition and surface and subsurface properties

The Cassini-Huygens mission has revealed the surface of Titan in unprecedented detail, enabling us to discern different geomorphological units on the surface (see the section entitled RADAR Science Results), constrain the relative times of emplacement of these units, and place constraints on composition. Titan has an ice shell (Figure RADAR-4), but water ice signatures are not easily detected due to atmospheric scattering and absorption that hamper the observations and the presence of complex organic molecules on the surface. The extended, dense, and hazy N_2-CH_4 dominated atmosphere shields the surface from direct optical observations, except at certain wavelengths where the methane absorption is weak. These methane atmospheric windows [McCord et al. 2006] are exploited by the Cassini VIMS to obtain compositional information of the top few microns of the surface, as discussed in the section entitled Surface. Composition from

VIMS and RADAR, while RADAR can probe the surface and subsurface scattering properties, and hence place additional constraints on composition.

SURFACE AND SUBSURFACE SCATTERING PROPERTIES

Compared to the surface of the Moon or Earth, the off-nadir radar response from most of Titan's surface is quite strong at Ku-band. This indicates that more complex processes than simple surface scattering, such as a significant volume scattering component, have to be considered [Elachi et al. 2005; Wye et al. 2007; Paganelli et al. 2007; Janssen et al. 2016]. Indeed, given the low Titan surface temperatures and the low loss tangent of analogs of materials relevant to Titan's surface, signals from Cassini RADARs Ku-band instrument should penetrate the surface down to a depth ranging from a few decimeters for an organic and compacted near-surface, to several meters for a pure water ice near-surface [Paillou et al. 2008a], and thus have multiple opportunities to be scattered. The RADAR observations of Titan are consistent with subsurface volume scattering processes, in addition to pure surface scattering. Analysis of Cassini scatterometer and radiometer measurements obtained simultaneously (see Figure RADAR-7) are best fit using models where volume scattering, enabled by the low material losses, is enhanced by coherent backscatter processes [Zebker et al. 2008; Janssen et al. 2011].

Janssen et al. [2016] further advance that a regionally enhanced degree of volume scattering is indicative of a higher abundance of water ice in the near-surface. This is because water ice is more transparent to microwaves than common organic materials, allowing for more opportunities for scattering. This would be consistent with about 10% of Titan's near-surface being water ice-rich while the composition of the remaining terrains is dominated by more absorbing organic materials, likely byproducts of the intense atmospheric photochemistry [Lorenz et al. 2008b; Hörst 2017]. The regions that contain a high degree of volume scattering include mountainous terrains, impact craters, fluvial and fan-like features, all of which possibly correspond to highly fractured or unconsolidated sedimentary materials derived from erosion. Many of these materials could also have originated from cryovolcanism, in which the radar signature could be explained by a strong volume scattering effect in a thick water-ammonia ice layer using a two-layer scattering model [Paillou et al. 2006]. Radar-bright sinuous channels in the southwest of Xanadu (see section entitled Xanadu), showing very large radar cross-sections, are also consistent with the presence of icy, low-loss, rounded scatterers, acting as efficient natural retro-reflectors [Le Gall et al. 2010].

Weaker radar reflectors such as Titan's dunes are most likely organic in nature (as also supported by VIMS—for example, Barnes et al. [2008], Soderblom et al. [2009], and Clark et al. [2010]). However, we note that these features exhibit somewhat high backscatter at large incidence angles compared to Earth analogs, which suggests even aeolian sediments may contain centimeter-scale gravels producing a significant volume scattering component [Paillou et al. 2014]. Features interpreted as mega-yardangs were observed on Titan, and they also exhibit a much brighter radar signature than their terrestrial analogs, indicating that additional scattering processes, such as volume scattering, occur in those materials as well [Paillou et al. 2016].

Lastly, and of particular interest, is the case of Titan's methane-dominated lakes, where radar waves can penetrate down to several thousand wavelengths (at least 150 m) and be subsequently backscattered by the bottoms of a lake or seabed [Mastrogiuseppe et al. 2014]. These results are consistent with recent laboratory investigations of the electrical properties of liquid hydrocarbons [Mitchell et al. 2015].

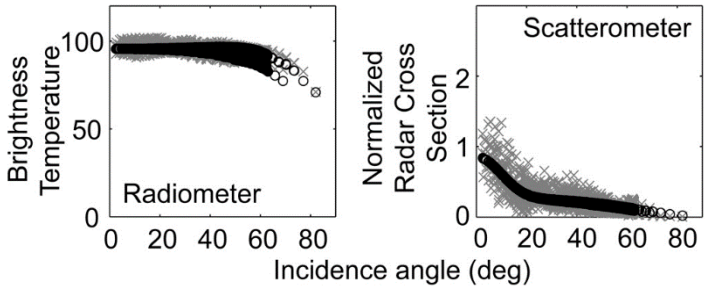

Figure RADAR-7. Angular dependence of radiometer (left) and scatterometer (right) measurements of a portion of Titan's surface. Grey X's are observations, while black circles are modeled values assuming both surface and volume scattering terms. Both sets of curves fall off slowly with incidence angle, indicative of significant volume scattering.

Surface composition from VIMS and RADAR

A combination of RADAR and near-infrared multispectral imaging data—VIMS—is a powerful way to distinguish and categorize geomorphological features into units with distinct chemical compositions (that remain to be identified). Spectroscopic observations of Titan's surface are severely hindered by the presence of an optically thick, scattering and absorbing atmosphere, allowing direct investigation of the surface within only a few spectral windows in the near-infrared. Based on the 1.29/1.08 μm, 2.03/1.27μm, and 1.59/1.27 μm band ratios measured by VIMS at low to moderate latitudes, three main spectral units were initially distinguished on the surface of Titan: 1) bright material mainly distributed in the topographically high and mid-latitude areas; 2) blue material adjacent to the bright-to-dark boundaries; and 3) brown material that correlates with radar-dark dune fields [Barnes et al. 2007; Soderblom et al. 2007; Jaumann et al. 2008].

Even though these spectral units are distinct, their actual compositions remain elusive. A number of chemical species was proposed to exist on the surface of Titan, but only a few absorptions were unambiguously detected from remote-sensing observations carried out by VIMS during Cassini flybys. A methane-ethane dominated composition seems to be present in the polar lakes and seas of Titan—for example, Brown et al. [2008], and Lunine and Lorenz [2009]. IR spectroscopy, microwave radiometry and scatterometry are sensitive to the physical structure of the surface to a different extent and at different scales. IR spectroscopy measurements are used to determine surface composition, but they are also affected, down to depths of micrometers, by the physical properties of the surface material like roughness, photometric geometry, and porosity.

Correlations between near-infrared and microwave data of Titan's surface are useful to gather a broader understanding of surface properties. These were quantified at coarse spatial resolution

by Tosi et al. [2010a], who applied a multivariate statistical analysis to an aggregated dataset made up of infrared spectra acquired by VIMS at spatial resolution of tens of km together with scatterometry and radiometry data measured by RADAR. This technique allowed for the identification of regional surface units at equatorial to mid-latitudes. Some of these units matched both the major dark and bright features seen in the ISS mosaic of Titan [Porco et al. 2005; Turtle et al. 2009], whereas other units showed boundaries not apparent from the visible and near-infrared remote-sensing data set. In particular, while dark equatorial basins are very similar to each other in terms of infrared and microwave reflectance at this spatial scale, the major bright features do not share the same characteristics.

A comprehensive investigation of Titan's surface features using the VIMS and RADAR-SAR datasets at the best available spatial resolution is still the best approach to characterize geomorphologic units using both spectral and morphologic characteristics. For example, the correlation between the 5 μm bright materials and RADAR empty lakes suggests the presence of sedimentary or organic-rich evaporitic deposits in dry polar lakebeds [Barnes et al. 2011a; MacKenzie et al. 2014]. Langhans et al. [2012] extensively studied the morphology, distribution, and spectral properties of Titan’s fluvial valleys showing that these are mostly associated with the bright surface unit.

In recent years, several investigators have applied radiative transfer models in addition to comparison between datasets—for example, Hirtzig et al. [2013]; Solomonidou et al. [2014]; Lopes et al. [2016]. These studies allow definition of both the surface and the atmospheric contributions from VIMS spectral imaging data after performing the appropriate pixel selection of areas of interest with the help of SAR data.

The application of radiative transfer analyses to the VIMS Titan data yields extracted weighted surface albedos in the seven methane windows, which have been tested against a variety of Titan candidate ice and organic constituents to provide constraints on the possible material present in various geomorphological units [Solomonidou et al. 2018]. An updated material library is used based on Bernard et al. [2006], Brassé et al. [2015], and the Grenoble Astrophysics and Planetology Solid Spectroscopy and Thermodynamics (GhoSST) database (https://ghosst.osug.fr). This library includes several materials at different grain sizes, such as ices of acetylene (C_2H_2), ethylene (C_2H_4), ethane (C_2H_6), propane (C_3H_8), cyanoacetylene (HC_3N), water (H_2O), ammonia (NH_3), methane (CH_4), and carbon dioxide (CO_2), in addition to spectra of laboratory tholins [Bernard et al. 2006; Brassé et al. 2015], and spectra of dark materials such as asphalite, kerite, different types of anthraxolite and amorphous carbon, which have been proposed to lower the total surface albedo of Titan’s surface—[Lellouch et al. 2006; GhoSST database].

Considering the different grain sizes, the library consists of 148 different constituent possibilities that can also be mixed. By using this constituent library, spectral simulations are made and an iterative process is used to obtain the best fit to the observations, bearing in mind that there is no unique solution for the whole mixtures. With these and other caveats, Solomonidou et al. [2018] have derived constraints on the possible major constituent for each geological unit and reported a latitudinal dependence of Titan’s surface composition with water ice being the major

constituent at latitudes poleward of 30° N and 30° S, while Titan's equatorial region appears to be dominated by a very dark organic material, possibly aromatic in character [Clark et al. 2010]. The surface albedo differences and similarities among the various geomorphological units also have implications for the geological processes that govern Titan's surface and interior (e.g., aeolian, cryovolcanic, tectonic).

Surface geology

MAJOR GEOLOGIC UNITS AND MAPPING

SAR data have been used since the early days of the mission to interpret different types of terrains (Figure RADAR-8) [Stofan et al. 2006; Paganelli et al. 2007, 2008; Lopes et al. 2010]. More recent work used not only SAR data but added correlations with data from other RADAR modes (altimetry, SARTopo, scatterometry, and radiometry), and also from VIMS and ISS to provide sufficient information on Titan's surface to distinguish the major types of terrain units [Malaska et al. 2016a; Lopes et al. 2016]. Also see Lopes et al. [2019] for the recently produced global geologic map. These data were also used to establish the major geomorphologic unit classes on Titan and their ages using contacts between units. In order of total surface area, the classes of units are: plains, dunes, mountainous/hummocky terrains, labyrinth terrains, lakes, and impact craters. The oldest units are the mountainous/hummocky and the labyrinth terrains; it is not possible with currently available data to differentiate the relative ages of these two oldest types of terrain. The mountainous/hummocky terrains consist of mountain chains and isolated radar-bright terrains. The labyrinth terrains consist of highly incised and dissected plateaus with medium radar backscatter. The plains are younger than both mountainous/hummocky and labyrinthic unit classes. Dunes and lakes of liquid hydrocarbons are the youngest unit classes on Titan. Additionally, we have identified individual features such as crater rims, channels, and candidate cryovolcanic features. Crater rims and candidate cryovolcanic features are locations more likely to expose materials from the icy crust, while the hummocky/mountainous materials are thought to be exposed remnants of the icy crust.

Characterization and comparison of the properties of the unit classes and individual features with data from radar radiometry, ISS, and VIMS provide information on their composition and possible provenance and shed light on the interconnection between the interior, the surface, and the atmosphere. Both microwave emissivity and VIMS are helpful in characterizing the units, although both have different penetration depths with microwave emissivity penetrating 10s of cm into the surface, while infrared-based responses such as VIMS and ISS, penetrate only the top surface coating, on the order of microns. Microwave emissivity data infer that the hummocky/mountainous terrains and impact crater rim features have relatively low emissivity (and greater radar scattering) in radiometric data, consistent with more water ice near the surface (Figure RADAR-2). The undifferentiated plains, dunes, labyrinth terrains, and lakes all have high emissivity (lower radar scattering) in radiometric data, which is consistent with low-dielectric organic materials.

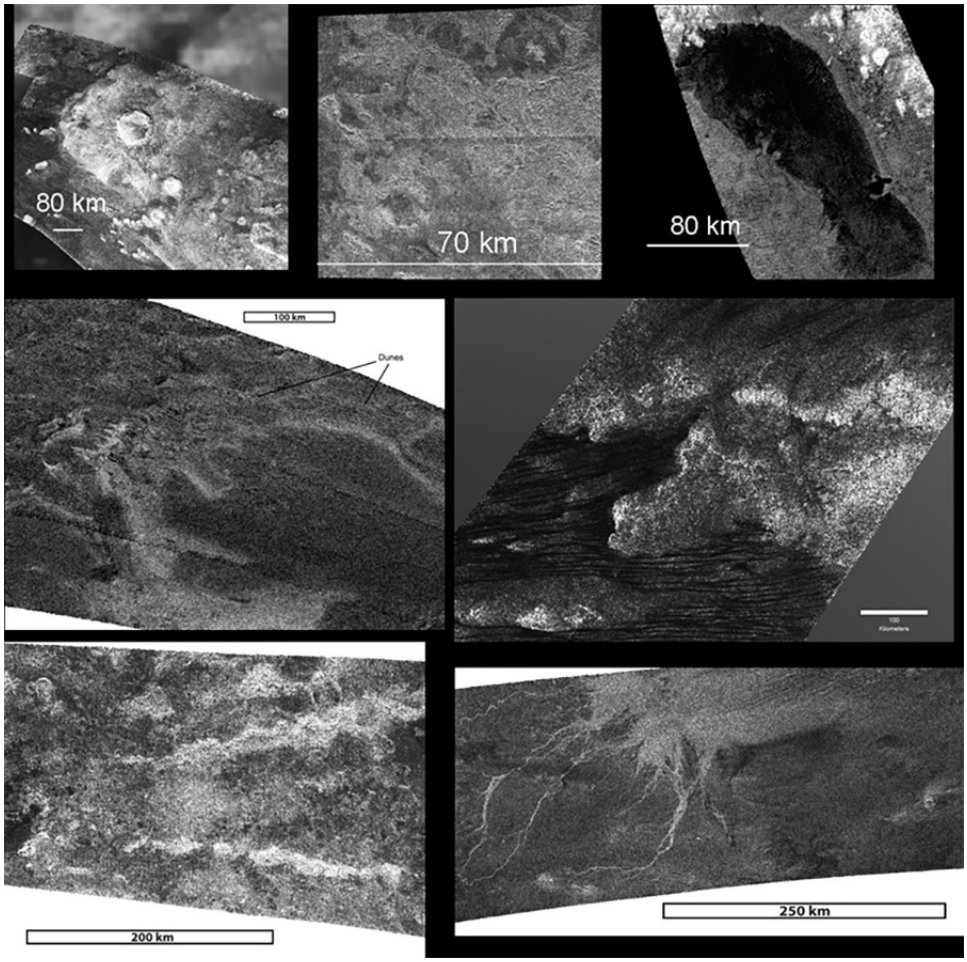

Figure RADAR-8. Examples of geologic features on Titan. Top row from left: Sinlap crater with its well defined ejecta blanket. Middle: Crateriform structure (suspected impact crater) on Xanadu. Right: Ontario Lacus near Titan's South Pole. Middle row, left: Bright (high radar backscatter) deposit Winia Fluctus abutting darker undifferentiated plains, the dunes indicated by arrows overlie part of deposit. Middle row, right: Dunes abutting against hummocky and mountainous terrain. Bottom left: Mountains (radar bright) in the equatorial region. Right: Elivagar Flumina, interpreted as a large fluvial deposit, showing braided radar-bright channels that overlie radar-dark undifferentiated plains.

Spectral coatings of the terrain units were described in Solomonidou et al. [2018] and discussed in the section entitled Surface Composition from VIMS and RADAR. From this analysis, three groups of compositional mixtures are reported, which include the major geomorphological units mentioned there: water ice, tholin, and a dark component. The units with spectral responses most similar to water ice are the labyrinth terrains and a number of different types of plains such as the streak-like, the scalloped, and the undifferentiated plains that are concentrated at the higher parts of the mid-latitudes. The impact crater ejecta and the alluvial fans are part of a different compositional group in which a tholin-like material is dominant. The units covered with an unknown dark constituent are the hummocky/mountainous terrains, the variable plains, the dunes, and the undifferentiated plains that are close to the equator and possibly contaminated by dune material

[Lopes et al. 2016; Solomonidou et al. 2018]. Since microwave radiometry and VIMS are global datasets (at lesser spatial resolution than SAR), we can also use these correlations to infer global distributions of regions not covered by SAR. This is particularly important as SAR data did not provide complete coverage of Titan at the end of the Cassini mission.

PLAINS

Plains are the most widespread type of terrain on Titan [Lopes et al. 2016]. Although there are several different types of plains, by far the most extensive are the Undifferentiated Plains, first mapped by Lopes et al. [2010]. These are vast expanses of radar-dark terrains that appear fairly uniform in SAR images, with no major topographic units, and are for this reason often referred to as blandlands. Lopes et al. [2016] mapped the distribution of the Undifferentiated Plains using SAR swaths up to flyby T92 (July 2013) and found that these terrains are located mainly at mid-latitudes. Their gradational boundaries and paucity of recognizable features in SAR data make geologic interpretation challenging, so Lopes et al. [2016] used all the RADAR datasets available, plus VIMS and ISS, to examine and evaluate different formation mechanisms including: (i) cryovolcanic origin, consisting of overlapping flows of low relief; or (ii) sedimentary origins, resulting from fluvial/lacustrine or aeolian deposition, or accumulation of photolysis products created in the atmosphere. Their analysis showed that exposure of Undifferentiated Plains in the lower mid-latitudes are consistent with a composition predominantly containing organic rather than icy materials and formed by depositional and/or sedimentary processes, unlike the undifferentiated plains in the higher mid-latitudes, which are consistent with water ice [Solomonidou et al. 2018]. The study concluded that aeolian processes played a major part in the formation of the Undifferentiated Plains, though other processes (fluvial, deposition of photolysis products) are likely to have contributed, possibly in differing proportions depending on location. However, the distribution of Undifferentiated Plains, both at local and global scales, is consistent with aeolian deposition being the major process contributing to their formation.

Spectral differences between the Plains and Dunes seen in VIMS data imply that the materials, at least on the top layers of the surface, are not exactly the same. Spectral differences in terms of surface albedo values between locations of Undifferentiated Plains [Lopes et al. 2016; Solomonidou et al. 2018] show that Plains at lower latitudes (closer to the dune seas) are more spectrally similar to dune materials, suggesting that they are related and supporting the idea that dune materials are transported by wind to mid-latitudes [Malaska et al. 2016a]. The Undifferentiated Plains located at lower mid-latitudes (and therefore closer to the equatorial dunes) appear to be composed predominantly of organic materials, which may have been cemented by an organic substance and/or wetted by methane, causing them to become spectrally different from dune materials, at least at a surficial level. Work by Malaska et al. [2016a] and Lopes et al. [2016] suggests that the plains deposits may be derived from modified dune materials—thus tying two of the major geomorphologic units together. If the Undifferentiated Plains materials are mainly the result of aeolian deposition but contain liquids due to methane rain or fluids transported by channels, this could explain why they show relatively high emissivity (lower global dielectric constant, less efficient volume scattering) as well as why they are free of observable dunes (reduced sediment mobility). It would also be consistent with the high level of degradation of craters

found at mid-latitudes, potentially due to efficient erosion by fluvial, pluvial, or subsurface flow activity [Neish et al. 2016].

DUNES

One of the youngest and most areally extensive geomorphologic units on Titan consists of sand dunes [Lorenz et al. 2006]. These appear as long, narrow, and SAR-dark features against a SAR-brighter substrate or interdune (Figure RADAR-9), presumably because dune sands are smooth to RADAR at the 2.17 cm Cassini SAR wavelength. The dunes are generally 1–2 km wide, spaced by 1–4 km and can be over 100 km long [Lorenz et al. 2006; Radebaugh et al. 2008]. Limited measurements of heights from radarclinometry suggest they are 80–130 m [Neish et al. 2010]. They are grouped together in large dune fields, or sand seas, equatorward of ± 30° latitude. The Titan's dunes interact with topographic obstacles, seen as SAR-bright and generally isolated mountains, in a way that indicates general W-E transport of sand; they pile up on the west side of obstacles, divert in their azimuth around the obstacles, and are sparser on the east side [Radebaugh et al. 2010]. Their size, general morphology and relationship with underlying terrain and obstacles, and their style of collection are nearly identical to large, linear dunes in Earth's sand seas of the Sahara, Arabia and Namibia [Lorenz et al. 2006; Radebaugh et al. 2008; Le Gall et al. 2011; Le Gall et al. 2012]. Such dunes on Earth typically form under bimodal winds [Fryberger and Dean 1979; Tsoar 1983]. A more recent model calls on a dominant, slightly off-axis wind and a secondary wind causing sand flux down the dune long axis [Courrech du Pont et al. 2014; Lucas et al. 2014].

Figure RADAR-9. Sand dunes on Titan appear as long, narrow, and SAR-dark features against a SAR-brighter substrate or interdune. Dunes on Titan as seen by the Cassini SAR, wavelength 2.17 cm, with spatial resolution of 350 m in the Belet Sand Sea, from the T61 (August 2009) swath on the equatorial leading hemisphere, at 11° S, 255° W. Dune surfaces are generally smooth and absorbing to SAR and thus typically, as here, appear as SAR-dark lines against a rougher and/or fractured, and thus radar- bright substrate, unless the RADAR is pointed directly at a dune face, in which case it appears as a thin, SAR-bright line. Occasionally the radar incidence is such as to give bright glints from dune slopes. The open arrows indicate the direction of SAR illumination and incidence angle. Figure from Radebaugh et al. [2013].

Regardless of whether the classical (bimodal) or fingering-mode dune growth mechanisms applies, a fundamental challenge raised by the RADAR observations of the dunes is the eastward direction of growth and sand transport [Lorenz et al. 2006; Radebaugh et al. 2010]. This contrasts with expectations that low-latitude near-surface winds should generally blow to the west. The solution appears to be that the dunes reflect strong but infrequent eastward winds, either associated with vertical mixing in the atmosphere at equinox leading to strong westerly gusts [Tokano 2010] or methane rainstorms having a similar effect [Charnay et al. 2015]. Additionally, convergence of the meridional transport predicted in models—for example, Lucas et al. [2014] can further explain why Titan's dunes are confined within ±30° latitudes, where sediment fluxes converge—see also Malaska et al. [2016a].

Titan's dune sands are not only dark to SAR but they are also some of the darkest materials seen by ISS [Porco et al. 2005; Karkoschka et al. 2017] and have a low albedo and "red" slope as seen by VIMS, thus comprising the VIMS dark brown spectral unit [Soderblom et al. 2007; Barnes et al. 2008; Clark et al. 2010; Rodriguez et al. 2014]. Volume scattering within the dunes is very low, consistent with smooth, homogeneous surfaces in general, and lacking large voids or clasts [Janssen et al. 2009; Le Gall et al. 2011], although modeling by Paillou et al. [2014] suggests shallow surface ripples and some volume scattering. The observations indicate the dunes cannot be composed of water ice, but rather must be made of organics, ultimately derived from photolytic processing of methane in the upper atmosphere, and precipitation to the surface [Lorenz et al. 2006, 2008a; Soderblom et al. 2007]. Sand sources could include river channels, as on Earth [Radebaugh 2013], low-latitude evaporite deposits, which can show similar VIMS properties [Barnes et al. 2011a]; or the mid-latitude blandlands, though it is more likely that sands are being transported there from the equatorial regions [Lopes et al. 2016; Malaska et al. 2016a]. The extent of the dunes indicates that sand has been generated on Titan in great volumes and transported by wind, and that processes have acted on the surface long enough to produce extensive and morphologically consistent landforms [Radebaugh 2013].

Gathering all exploitable SAR and HiSAR images since the start of the Cassini mission, Rodriguez et al. [2014] built a global map of the dune coverage available at that time, accounting for observations from TA to T92 flybys (from October 2004 to July 2013) and more than 30 individual RADAR SAR and HiSAR swaths. They evaluated that dunes cover 13 ± 2% of the 58.1% of Titan's surface observed with SAR and HiSAR, considering only those images having sufficient spatial resolution to identify individual dunes—that is, excluding HiSAR swaths with a resolution coarser than 2 km/pixel. In terms of latitudinal distribution, 99.6% of the imaged dunes are found within the equatorial belt (within ±30° latitudes—61.3% of which has been imaged after flyby T92. The overlapping of a VIMS global mosaic and the global distribution of dunes as seen by the RADAR highlights the strong correlation between the dunes and a specific infrared unit spectrally compatible with complex solid organics (the dark brown unit). This allowed an extrapolation of the dune geographic distribution to the entire spatial extent of the VIMS dark brown unit, even in locations where dunes are not seen because of lack of RADAR coverage, and extending the previously estimated total surface area of Titan covered by dunes up to ≈17% (≈14×10^6 km^2, 1.5 times the surface area of the Sahara desert on Earth), the same as early estimates from Lopes et al. [2010]. A simple calculation of the volume—for example, Lorenz et al.

[2008b]—indicates that dunes are a major surface reservoir of organics, probably originating from the atmosphere.

In addition to dunes, there are other aeolian features and landforms on Titan's surface. These are wind streaks and yardangs, or wind-carved ridges. The wind streaks are visible in ISS images as bright features that extend in the downwind direction from obstacles—for example, Porco et al. [2005]; Lorenz et al. [2006]; Malaska et al. [2016a]. They can be several tens of kilometers wide and long, can have flow-like, teardrop shapes, and appear as though wind has shaped the bright landscapes and deposited dark materials, likely sand, in the low regions downwind of the obstacles. These features help indicate the direction of the winds, which also broadly parallels the linear dunes seen in Cassini SAR images [Malaska et al, 2016a].

Deposits that are SAR-bright, circular in planform and likely elevated into small mounds or domes are found in some regions in the northern mid-latitudes [Lopes et al. 2016]. These domes are easily eroded as revealed by deep, badlands-like river channels that flow outwards from their centers. Cutting across the channels and the domes are a series of parallel, long lineation ~1 km wide, spaced by a few km, and tens of kilometers long [Paillou et al. 2016; Northrup et al. 2018]. They are similar in appearance and SAR brightness, radiometry and scatterometry to yardangs, or wind-carved ridges [Paillou et al. 2015]. These appear to have formed in easily eroded materials, similar to yardangs on Earth and Mars, and further indicate the action of wind at moderate to high latitudes now or in the past [Northrup et al. 2018].

IMPACT CRATERS

Before Cassini arrived at Saturn, the impact cratering history on Titan was unknown from direct observations. Estimates of the cratering rate were made by extrapolating the crater distributions observed on other Saturnian satellites, or by predicting impact rates by comet populations. Such estimates suggested that at least several hundred craters larger than 20 km in diameter should be present on Titan [Zahnle et al. 2003]. Impactors that would create craters smaller than 20 km in diameter are expected to be disrupted by Titan's atmosphere [Artemieva and Lunine 2005; Korycansky and Zahnle 2005]. Cassini RADAR observations show an extreme paucity of craters. Only 23 certain or nearly certain craters and ~10 probable craters >20 km in diameter have been observed on Titan, with a handful of smaller crater candidates [Wood et al. 2010; Neish and Lorenz 2012; Buratti et al. 2012; Neish et al. 2016]. This suggests that Titan has a crater retention age of several hundred million years [Wood et al. 2010; Neish and Lorenz 2012], with the oldest surfaces located near the equator and the youngest surfaces located near the poles [Neish et al. 2016].

The craters that are observed on Titan all show evidence for extensive modification by erosional processes (Figure RADAR-10). Channels are observed to cut through the ejecta blankets and floors of several impact craters [Wood et al. 2010; Soderblom et al. 2010; Neish et al. 2015]. Many of Titan's impact craters are located in its equatorial sand seas, and also show evidence for extensive infilling by sand [Wood et al. 2010; Le Mouelic et al. 2008; Neish et al. 2013]. In addition to the morphologic evidence for erosion and burial, Titan's craters are consistently shallower than similarly sized fresh craters on Ganymede (often by many hundreds of meters), suggestive of infill

[Neish et al. 2013]. Given the distribution of depths, aeolian infilling appears to be the dominant modification process on Titan [Neish et al. 2013], but fluvial erosion seems to play an important secondary role [Neish et al. 2016]. Modification by viscous relaxation is expected to be minimal given the cold lithospheric temperatures on Titan, although insulation by sand could enable some relaxation in Titan's larger craters [Schurmeier and Dombard 2018].

In addition to being highly modified, Titan's impact craters are not uniformly distributed across the moon. There is an almost complete absence of impact craters near Titan's poles, with the majority of the craters found in the topographically high, equatorial sand seas [Neish and Lorenz 2014]. There have been several hypotheses advanced to explain this observation. Neish and Lorenz [2014] proposed the lack of craters near Titan's poles might be indicative of marine impacts into a former ocean in this region. Moore et al. [2014] suggested that extreme climate change occurred in Titan's recent past, causing global methane rainfall that produced sediment that settled in Titan's topographically low polar regions, burying any craters there. Finally, Neish et al. [2016] suggested that an increased rate of fluvial erosion near the poles could degrade Titan's craters to the point where they would be unrecognizable from orbit. In any case, Titan's cratering record demonstrates that it is an extremely dynamic world, and studying its impact structures can reveal much about the processes that have shaped it.

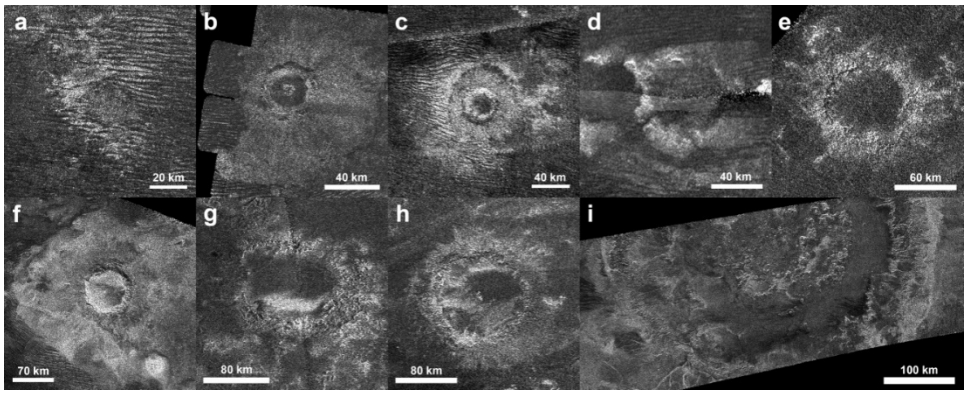

Figure RADAR-10. Nine probable impact craters observed on Titan by Cassini RADAR. From smallest (a) to largest (i) the impact craters on Titan show modification by exogenic processes such as fluvial erosion and infilling by sand [Neish et al. 2013].

MOUNTAINS AND TECTONICS

Features of relatively high topography, termed mountains, have been observed across Titan (Figure RADAR-11). Topography on icy satellites is rare, taking the form of, for example, impact crater rims, grooved terrain on Ganymede, or the towering scarps of Miranda. This is in part because water ice generally loses strength with increasing depth, making high topographies difficult to support. However, the exceptional amount of erosion on Titan may also be responsible for terrain height reduction. Overall, topography on Titan is rather subdued, having a range of just a few kilometers [Lorenz et al. 2013; Corlies et al. 2017]; nevertheless, there are features on the surface aside from impact crater rims that are elevated. These take the form of isolated blocks, chains, ridges, and elevated plateaus [Radebaugh et al. 2007]. Mountains of all types are SAR-bright due

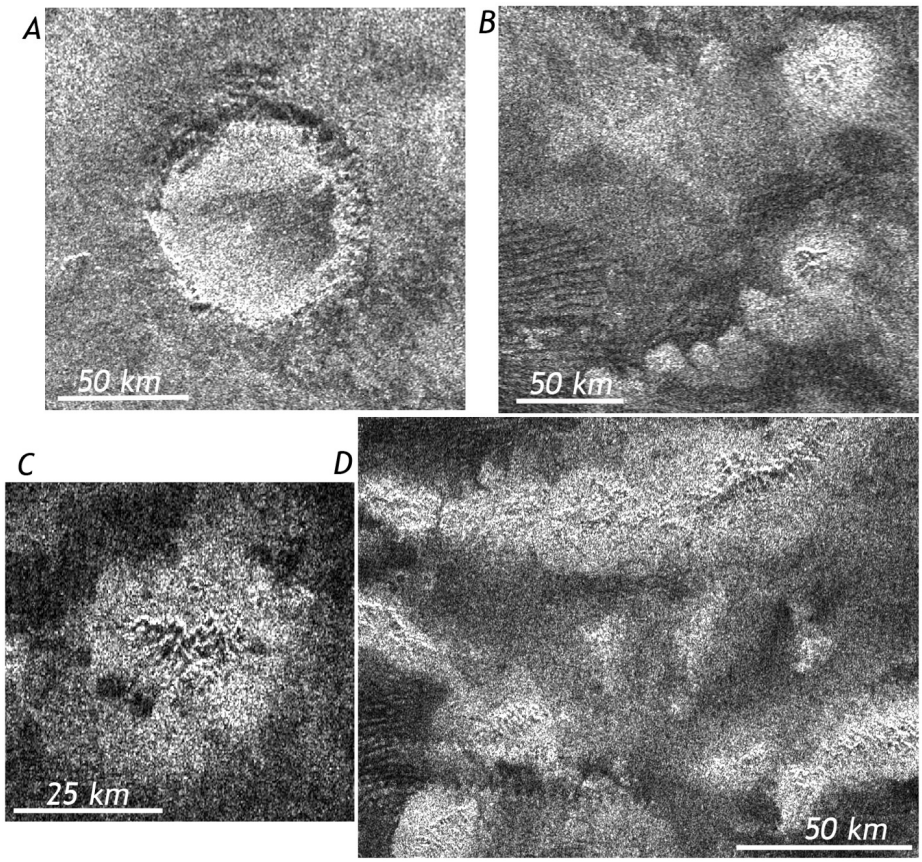

Figure RADAR-11. Some examples of mountains on Titan. Radar illumination is from the top in all cases, and north is up. Bright, possibly erosional, blankets surround the central, high elevation features visible as bright/dark pairs. A) Sinlap crater, shown to demonstrate the effects of radar illumination on a rimmed depression; B) Individual mountain blocks in the T3 swath south of Sinlap crater; C) Rugged mountain from the T3 swath; D) A portion of mountain ranges west of the Huygens landing site from the T8 swath. Figure from Radebaugh et al. [2007].

to the roughness and fractured nature of the materials, as well as the slope geometry with respect to the SAR antenna look direction and incidence angle. Mountains also exhibit high scattering and have a high emissivity as seen by RADAR [Janssen et al. 2009, 2016], and are part of the VIMS bright blue unit [Barnes et al. 2007], indicating a higher water-ice component, which is dominant in Titan's lithosphere.

Isolated mountain blocks are found only in a few select regions and tend to be several km across and a few hundred meters high as calculated from radarclinometry [Radebaugh et al. 2007]. More frequently, mountains are found in small belts near the middle and high latitudes. They are only few to tens of kilometers in length and a few hundred meters high. Mountain chains are the most areally extensive rugged features (aside from Xanadu) and are the most dramatic on the surface, being found dominantly at the equatorial regions and generally aligned E-W. They are up to several hundred kilometers in length, are arcuate in planform, and can be up to several kilometers high [Radebaugh et al. 2007; Radebaugh et al. 2016]. In Xanadu, there are extensive, mountainous and rugged terrains. These appear crenulated to SAR and exhibit multiple

overlapping peaks concentrated in regions over tens to hundreds of square kilometers. They are interspersed with lineations that indicate a regional tectonic fabric, likely extensional, given the straight nature of the lineations [Radebaugh et al. 2011]. All mountains on Titan are highly rugged and exhibit signs of extensive erosion from methane rainfall and possibly mass wasting. All mountain ridges and chains exhibit a preferential orientation [Cook-Hallett et al. 2015; Liu et al. 2016a] indicating internal tectonic forces operating on their formation. The equatorial mountain chains differ in morphology from long, narrow tectonic features on other icy satellites: they sit on elevated topography [Radebaugh et al. 2016], they are arcuate in morphology, and they have low slopes [Liu et al. 2016b]. This indicates they are more likely to have been created by contractional tectonism, by N-S directed forces in the interior and at the equator. Such thrust faulting could have been enabled by liquid methane within the crust, which could act to lubricate fault zones, much as occurs on Earth with water [Liu et al. 2016b]. A similar conclusion is reached for the mountain ridges north of Xanadu, which contain the highest peak on Titan at just over 3,300 m [Radebaugh et al. 2016]: that they were formed by contractional tectonism [Mitri et al. 2010]. Some very large-scale tectonic rises, several hundred kilometers across, may be topographic rises related to laccolithic activity [Schurmeier et al. 2017].

CRYOVOLCANISM

The possibility of finding cryovolcanic features on Titan had been discussed prior to Cassini by Lorenz [1993, 1996]. The case for cryovolcanism was strengthened by results from the Gas Chromatograph Mass Spectrometer (GCMS) instrument on board the Huygens probe, which detected the radiogenic isotope of argon in Titan's atmosphere [Niemann et al. 2005] in concentrations suggesting that the atmosphere was in communication with a reservoir of the parent atom. Prior to the first Titan flyby using RADAR, VIMS imaged a bright feature (later named Tortola Facula) that Sotin et al. [2005] proposed to be cryovolcanic in origin. However, SAR images obtained later in the mission showed Tortola Facula to be a local topographic high similar to others elsewhere on Titan [Lopes et al. 2013] and not a candidate for a cryovolcanic feature. Sotin et al. [2005] further suggested that the upwelling of large cryovolcanic plumes might be releasing sufficient methane into the atmosphere to account for the known atmospheric composition.

Cassini RADAR and VIMS revealed several features interpreted as formed by cryovolcanism [Barnes et al. 2006; Sotin et al. 2005; Lopes et al. 2007; Soderblom et al. 2009; Wall et al. 2009; Lopes et al. 2013; Solomonidou et al. 2016]. However, the interpretation has been the subject of some debate—for example, Moore and Pappalardo [2011]—and has not been entirely resolved by Cassini data [Nixon et al. 2018], primarily due to limitations in spatial resolution and coverage. The cryovolcanic interpretations by RADAR (using several data sets including SAR, stereogrammetry [Kirk et. al. 2010], SARTopo, and radiometry) and VIMS (surface albedo retrievals, surface composition constraints, and temporal variations) are based on morphology, differences in surface albedo between the cryovolcanic areas, their surrounding terrains and several other geomorphological features, and temporal variations detected by VIMS [Barnes et al. 2005; Solomonidou et al. 2014, 2016, 2018]. However, the Cassini mission did not reveal any hot spots, i.e., thermal enhancements, that would have provided conclusive proof. The detection of thermal activity at Titan’s surface using radiometry data (which is sensitive to variations of ~1K) or VIMS,

would require Cassini's instruments to be observing the right locations at the right times and in multiple occasions, an unlikely scenario given the consensus that cryovolcanic candidate features are not ubiquitous on Titan [Lopes et al. 2010].

Landforms considered as possibly cryovolcanic include flow-like terrains seen on the western margin of Xanadu [Wall et al. 2010], spectrally different regions in Tui Regio [Barnes et al. 2005] and tangled flow regions in Hotei Regio [Soderblom et al. 2009; Wall et al. 2010]. These flow-like morphologies even exhibit elevated, lobate margins typical of flows. Other possible cryovolcanic features are the steep-sided, small lakes at the north polar region (see section entitled Lakes). These landforms have slightly elevated rims, steep sides, flat floors, and deposits diffuse to SAR surrounding them. All of these characteristics are typical of maar craters on Earth [Wood et al. 2007] though they are also generally consistent with dissolution and sublimation-related features [Hayes et al. 2017].

The strongest evidence for cryovolcanic features on Titan was put forward by Lopes et al. [2013] who combined SAR imaging (including stereogrammetry, Figure RADAR-12) and VIMS data (Figure RADAR-13) for a region that includes two mountains, Doom Mons (40.4° W, 14.7° S) and Erebor Mons (36.2° W, 5.0° S), as well as a depression, Sotra Patera (40.0° W, 14.5° S), and a region consisting of flow-like features, Mohini Fluctus (centered at 38.5° W, 11.8° S). Doom and Erebor Montes are tall mountains (Doom being ~70 km in diameter and 1.5 ± 0.2 km high,), Sotra Patera is

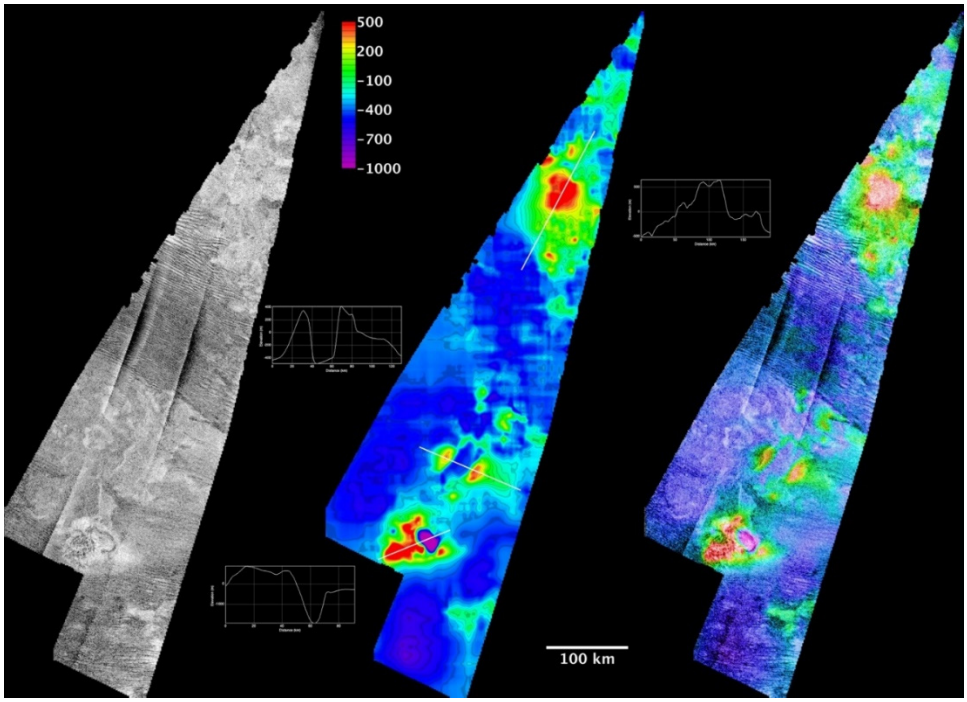

Figure RADAR-12. Topography of Doom Mons, Sotra Patera and (at the top) Erebor Mons region from SAR stereo. The image on the left is SAR over the region. The central image shows a color-coded DTM (scale shown), with the tops of Doom and Erebor Montes being the highest points, the white lines show the locations of the three profiles shown. The SAR and DTM are merged at the right. Figure from Lopes et al. [2013].

the deepest depression found on Titan (1.7 ± 0.2 km deep, relative to surrounding terrain). It is non-circular and interpreted as a collapse feature adjacent to Doom Mons (Figure RADAR-13). Mohini Fluctus appears to emerge from Doom Mons. Other non-circular, collapsed depressions are located between the two Montes, and flow-like features also surround Erebor Mons.

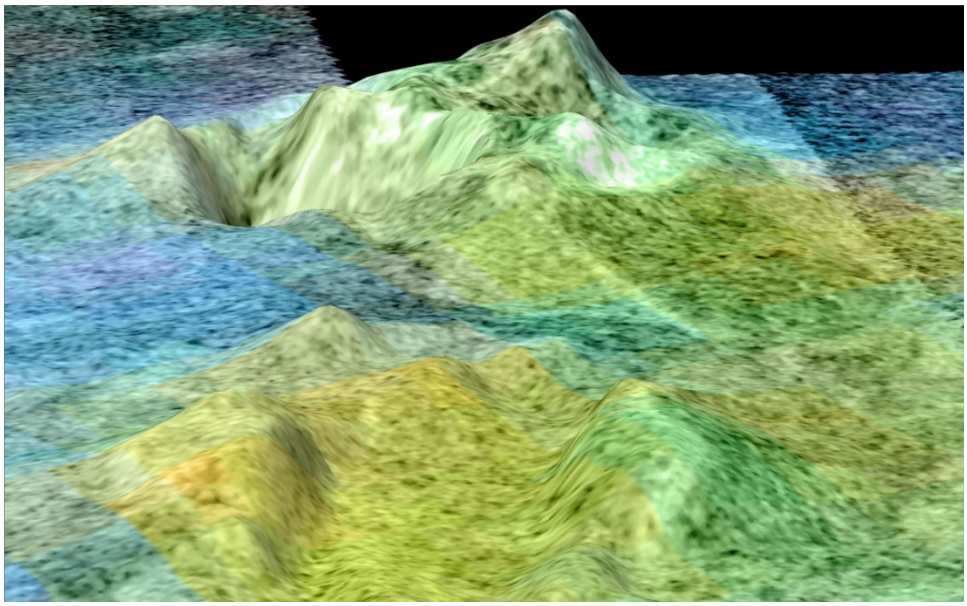

Figure RADAR-13. Perspective view of Doom Mons and Sotra Patera. This 3-D image was obtained by combining a digital topographic model (produced from two SAR swaths) and VIMS data showing compositional differences in representative color, which shows that the dune fields (in blue) are of a different composition from the candidate cryovolcanic materials in shades of green and yellow. The image shows one of the tallest peaks on Titan, Doom Mons, which is ~70 km in diameter and 1.5 ± 0.2 km high. Doom Mons is adjacent to the deepest depression so far found on Titan, Sotra Patera, an elongated pit ~30 km in diameter and 1.7 ± 0.2 km deep. The DTM data have a vertical exaggeration of 10:1. A movie showing the whole region can be seen at http://photojournal.jpl.nasa.gov/catalog/PIA13695.

A criticism by Moore and Pappalardo [2011] of initial interpretations by RADAR of cryovolcanic candidates reported by Lopes et al. [2007] is that flow-like features could have been produced by fluvial activity, since channels are seen in areas such as Hotei Regio and Ganesa Macula (which topography later obtained by RADAR showed it was not a shield or dome as initially interpreted). However, the Doom Mons-Sotra Patera-Erebor Mons region is totally devoid of visible fluvial channels, making a fluvial origin for Mohini Fluctus and other flows unlikely. A vast dune field is located between Doom and Erebor Montes, indicating a dry region. The depressions seen in the region, including Sotra Patera, are not circular, are very deep, and are therefore unlikely to have had an impact origin [Lopes et al. 2013]. VIMS data analysis has contributed to the cryovolcanic interpretation via two different types of investigation. First, analysis of VIMS data using a radiative transfer model [Solomonidou et al. 2014] showed that the surface albedo of the candidate cryovolcanic features is different from that of plains or dunes, indicating differences in composition [Solomonidou et al. 2014]. Following this and again using a radiative transfer model on a large selection of VIMS data, Solomonidou et al. [2016] revealed temporal changes for the Sotra Patera

and Mohini Fluctus areas, which became brighter up to a factor of two in terms of pure surface albedo and brightness during one year (2005–2006), while surrounding areas and the undifferentiated plains and dunes did not present any significant change for the same period of time. The surface albedo variations, together with the presence of volcanic-like morphological features consistent with volcanism, suggest that the regions might be active and possibly connected to the deep interior via cryovolcanic processes. Additional support for cryovolcanic origin of these features comes from interior structure models of Titan and corresponding calculations of the spatial pattern of maximum tidal stresses [Sohl et al. 2014], which indicate that the Doom Mons-Sotra Patera-Erebor Mons area is a likely region for cryovolcanic activity.

LABYRINTH

The enigmatic labyrinthic terrains of Titan are defined as elevated highly-dissected plateaus with intersecting valleys or remnant ridges of low to medium backscatter with a generally >5,000 km^2 extent [Malaska et al. 2010; Moore et al. 2014; Malaska et al. 2016b; Malaska et al. 2017a]. The Katain Labyrinth (Figure RADAR-14) is a typical example. SARTopo suggests that labyrinth terrains are among the locally highest units on Titan [Stiles et al. 2009]. Often the valley floors contain radar-dark floors or fill. The valley and upland widths are variable: in areas where the valleys are narrow and the intervening uplands (or valley spacing) are wide, the terrain appears in the form of a dissected plateau; when the widths of the valleys and the widths of the intervening plateaus are about equal, the terrain appears as a series of valleys and intervening plateaus; and when the valleys are wide and the widths of the intervening plateaus are small, the terrain can appear as a series of remnant ridges. Closed valleys may also be present, although this may be a misinterpretation due to the coarse resolution of the Cassini RADAR.

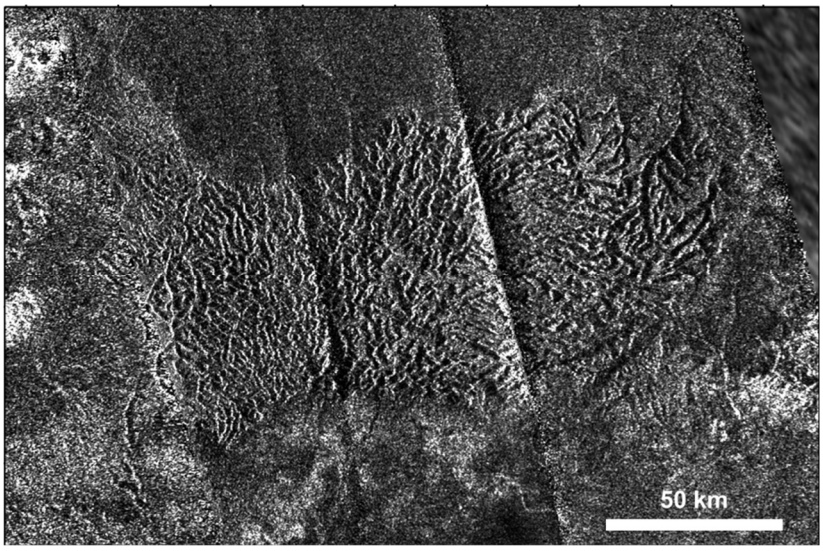

Figure RADAR-14. SAR image of Katain Labyrinth. The highly dissected feature at center is Katain Labyrinth. SAR illumination is from right (large straight lines through center are SAR artifacts due to beam overlap). Sinusoidal projection centered at 349 W. North is at top.

Wide valleys may appear suddenly in the plateaus, suggestive of amphitheater-headed valleys. The overall planforms of the labyrinth terrain units are circular, ovoid, or tabular. The valley density at a scale of 300 m/pixel is above 0.02, significantly higher than the density of valley networks described elsewhere on Titan such as the network in western Xanadu [Burr et al. 2009]. The valley networks inside the labyrinth units are rectangular to dendritic, suggesting varying amounts of structural and topographic control. Some of the more circular planform labyrinths have valley or ridge networks that are radial, extending away from the center of the region, suggesting that doming occurred prior to erosion, possibly as a result of a liquid water laccolith injection at depth [Shurmeier et al. 2017, 2018]. At the terminus of the valley networks and in contact with the labyrinths, undifferentiated plains units are found, suggesting a close connection between the two types of units, at least at the local scale.

The labyrinth terrains are composed almost wholly of a possibly uplifted thick plateau of organic materials, with very little water ice materials present.

The labyrinth terrains are composed almost wholly of a possibly uplifted thick plateau of organic materials, with very little water ice materials present. The emissivity data shows that labyrinth terrains have significantly higher emissivity than mountain and hummocky terrains and have similar emissivities to dunes or undifferentiated plains. The microwave data are consistent with the labyrinths being composed of low dielectric organic materials and are not consistent with materials containing significant amounts of water ice.

The labyrinths were likely formed from the uplifted plateaus through a combination of dissolution coupled with mechanical erosion, or other phase changes that could allow the development of closed valleys with transport of the remaining materials to the outlying plains. Karstic dissolution is a likely scenario, and many of the labyrinth terrains have morphologic analogs with terrestrial karst terrains [Malaska et al. 2010]. Theoretical predictions and laboratory work have shown that organic materials on Titan may dissolve when exposed to Titan hydrocarbon rainfall or liquids [Raulin 1987; Lorenz and Lunine 1996; Cordier et al. 2009; Malaska et al. 2011a; Glein and Shock 2013; Malaska and Hodyss 2014; Cornet et al. 2015; Cornet et al. 2017]. Dissolution geology on Titan may create a landscape that is similar to terrestrial karst terrain present in water-soluble materials such as limestone and gypsum on Earth [Malaska et al. 2011a; Malaska and Hodyss 2014; Cornet et al. 2015]. Preliminary modelling by Cornet et al. [2017] suggests that blocks of Titan soluble materials could dissolve under Titan conditions to form the features observed by SAR that are similar to polygonal karst. The evolution sequence begins with incised valleys in a plateau, then widening to form the end-stage wide-floored remnant ridges. Type examples of each stage are found in close proximity near Sikun Labyrinth in Titan's south polar terrain and are shown in Figure RADAR-15. However, other formation scenarios are possible, including differential hardening and deflation, aeolian deflation, or other phase change and removal processes such as sublimation. From superposition relations, the organic labyrinths represent an ancient terrain [Malaska et al. 2016b]. Thus, the labyrinth terrains unit represents a significant deposit of organic materials on Titan, and suggests that significant organic deposition, lithification, and uplift/exposure occurred early in Titan's history.

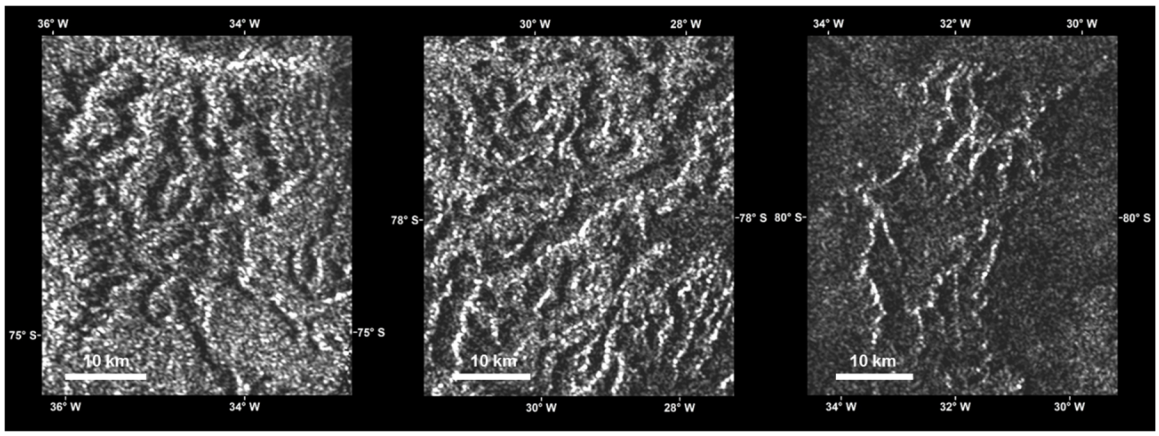

Figure RADAR-15. SAR images of different types of labyrinth terrains found in close proximity in Titan's south polar terrain. Left: Naraj Labyrinth, represents thin valleys incised in a plateau, Center: Sikun Labyrinth, represents valleys and plateaus of near equal width, Right: Tupile Labyrinth, a type example of remnant ridge. Sinusoidal projection. North is at top.

Xanadu

Much of Titan's geology has a regional organization; dunes and mountain belts are found near the equator, lakes and seas are found near the poles, and relatively bland regions are located in the mid-latitudes [Lopes et al. 2010]. Xanadu (Figure RADAR-16), however, is a continent-sized region that breaks with all predictions. It is 4,000 × 2,500 km wide, is located on Titan's leading hemisphere, and interrupts the equator-encircling sand seas. The feature was observed before Cassini arrived [Lemmon et al. 1993; Smith et al. 1996], and efforts were made to observe and understand Xanadu by Cassini SAR and other instruments. Xanadu is generally SAR-bright, which indicates it is composed of rough and fractured terrains [Radebaugh et al. 2011]. It has a high backscatter but low brightness temperature as indicated by scatterometry and radiometry measurements, which is consistent with a water-ice composition in the bedrock [Wye et al. 2007; Zebker et al. 2008; Janssen et al. 2009, 2016]. Furthermore, some portions of Xanadu are correlated with the VIMS dark blue unit, indicating there is a higher than average percentage of water-ice exposed at the surface [Barnes et al. 2007].

Xanadu is unique in several respects to other regions on Titan. While geologically diverse, many regions in Xanadu have extremely rugged terrains, manifest as many adjacent, deeply eroded, and incised mountain ranges [Radebaugh et al. 2011]. There are broad scale linear features characteristic of NE-SW and NW-SE extensional tectonism, and broadly arcuate mountain ranges indicative of N-S directed contractional tectonism [Radebaugh et al. 2011]. These features all indicate a long and complicated tectonic history for Xanadu. Extensive, dendritic networks of varying morphologies [Burr et al. 2009], large channels that distribute fans and cobbles to the south [Le Gall et al. 2010], and the extensive erosion of the mountains also reveal a long erosional history. Over twice as many impact craters or possible impact craters can be found in Xanadu as on the rest of Titan [Wood et al. 2010; Radebaugh et al. 2011], which is further evidence of the generally old nature of Xanadu compared with the rest of the surface of Titan [Radebaugh et al. 2011; Wood

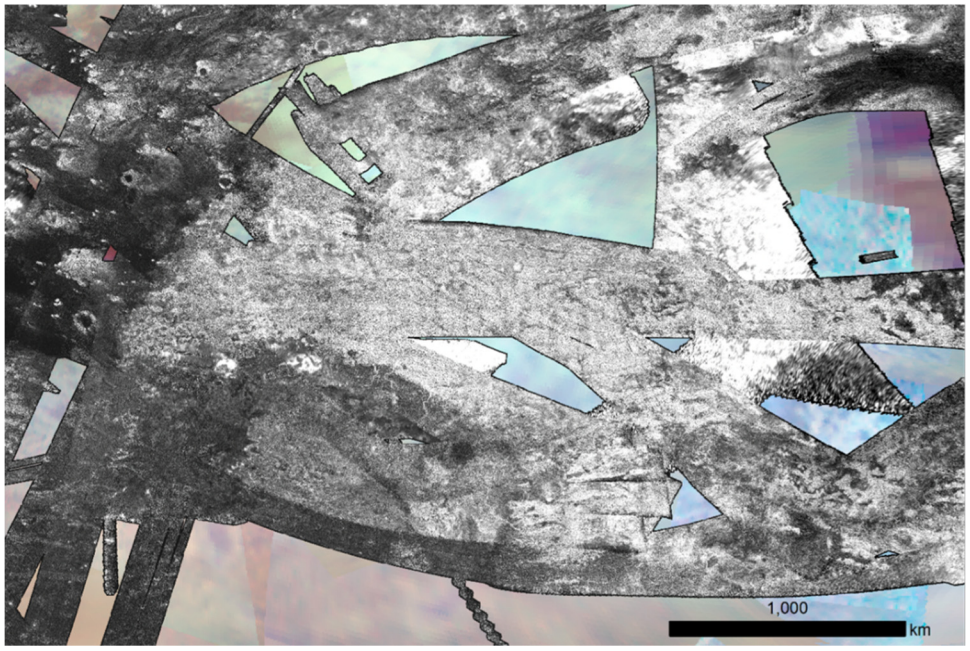

Figure RADAR-16. Xanadu region. All Cassini SAR and HiSAR image swaths covering the Xanadu region, overlain on a VIMS basemap. Xanadu is generally SAR-bright because of rough terrain and fractured ice, which is interspersed with valleys filled with SAR-darker sediment. Some regions of Xanadu are VIMS dark blue, consistent with the presence of exposed water ice. The southwest margin of Xanadu has large river channels emptying to the south.

et al. 2010]. A region of mottled terrain is found on the western margin, with arcuate depositional morphologies and lack of integrated drainage, postulated to be a possible cryovolcanic deposit [Wall et al. 2009]. These morphologies are consistent with other possible cryovolcanic zones in Hotei Regio, bordering Xanadu's southern margin [Soderblom et al. 2009]. These landforms may instead be related to swamp-like deposits entirely fluvial in origin, but they are unique and not widespread.

Xanadu's most puzzling characteristic is that despite the abundance of mountains and high local topographic differences, the region as a whole appears to be regionally lower in elevation than anywhere else near the equator [Zebker et al. 2009a; Stiles et al. 2009]. This is evidenced by radar altimetry measurements as well as SARTopo observations [Stiles et al. 2009]. It is possible that after a time period of mountain-building and contraction, there was gravitational collapse of the water ice crust [Mitri et al. 2010], resulting in broad extensional tectonism and down-dropping of Xanadu [Radebaugh et al. 2011]. This scenario might have led to Xanadu-bounding fault zones, along which the possible cryolavas of western Xanadu and Hotei in the south could have ascended [Radebaugh et al. 2011].

What could have driven this N-S directed contractional tectonism is unknown but might have resulted from global contraction related to interior cooling, tidal spin-up or spin-down, or internal convection [Radebaugh et al. 2011]. Another scenario hypothesized for the formation of Xanadu

involves a large impact event early in Titan's history, leaving behind a disrupted terrain [Brown et al. 2011].

Several outstanding questions about Xanadu remain, in addition to its origin: Why is it regionally depressed? Why do the dunes of the equatorial sand seas not cover and fill Xanadu? Why is water ice more exposed here than in most other places on Titan? Much remains to be learned about this unusual region.

Lakes

While ISS revealed ~50 dark features poleward of 70° S during one of Cassini's first observations of Titan, these features were not initially referred to as lakes as they could not be distinguished from dark equatorial dune fields at optical wavelengths [Porco et al. 2004]. The first high-resolution and definitive observations of Titan's hydrocarbon lakes were acquired by the RADAR in July 2016 (T16), when ~75 features with exceptionally low backscatter, high emissivity, and distinctly lacustrine morphology were identified in SAR images [Stofan et al. 2007]. Subsequent observations have revealed more than 650 such features, both dry and filled, scattered throughout Titan's polar terrain [Hayes et al. 2008; Birch et al. 2017]. These features have diameters that follow a log-normal distribution with a median of 77 ± 20 km [Hayes et al. 2016]. The morphology of both dry and filled lakes and seas on Titan provide a record of past and current climatic conditions and surface evolution processes. For example, while Titan's large seas have complex shorelines that are consistent with drowning of pre-existing topography, most of the smaller lakes are steep-sided depressions that are more consistent with dissolution-based erosion driven by karstic processes [Hayes et al. 2017; Cartwright et al. 2011; Langhans et al. 2012]. For a recent and more detailed review of Cassini's exploration of Titan's lakes and seas, see Hayes et al. [2016].

Lakes and seas encompass 1% of Titan's total surface area [Hayes et al. 2016]. The majority of surface liquids (97% by area) reside in the north polar region, with 80% of all liquid-filled surface area contained in three large seas; Kraken Mare, Ligeia Mare, and Punga Mare (Figure RADAR-17; note that the coloration in this figure is artificial). The largest modern liquid body in the south polar region is Ontario Lacus, although several large empty basins that encompass an area similar to the northern maria (7.6×10^5 km^2) have been identified and interpreted as paleoseas [Hayes et al. 2010, 2011; Birch et al. 2018b]. The observed dichotomy in lake distribution has been attributed to a net transport of ~5×10^{14} kg of methane per Titan year from the South Pole to the north, driven by a seasonal asymmetry in solar insolation that is the result of Saturn's eccentric orbit around the sun [Aharonson et al. 2009; Lora and Mitchell 2015]. Summer solstice in Titan's southern hemisphere occurs near perihelion while northern summer solstice occurs at aphelion, resulting in 25% higher peak insolation during southern summer as compared to northern summer. Long timescale (~100,000 year) orbital cycles can switch the direction and magnitude of the seasonal asymmetry driving this transport, moving liquid deposits between the poles similar to the way Croll-Milankovitch cycles drive ice ages and other long-term climate effects on Earth [Aharonson et al. 2009]. The presence of drowned river valleys at the terminus of channels flowing into the northern seas [Stofan et al. 2006], as well as the presence of exposed and abandoned river deltas adjacent

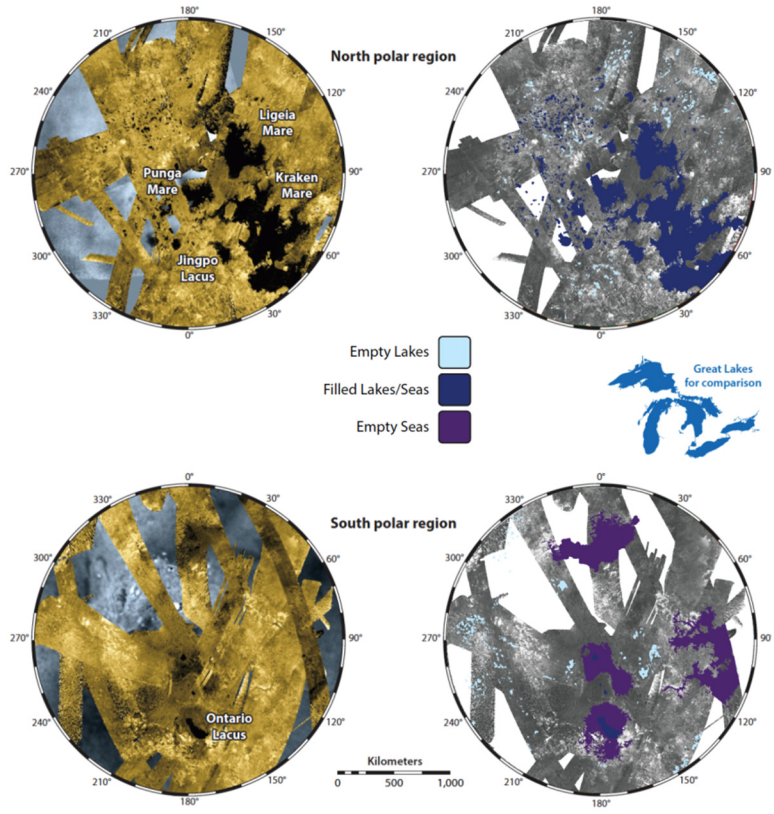

Figure RADAR-17. Map of lakes and seas on the northern (top) and southern (bottom) polar regions of Titan.

to the shores of southern Ontario Lacus [Wall et al. 2009], support the theory of rising and falling liquid levels as the magnitude and direction of net pole-to-pole methane transport varies with Titan's orbital cycles [Lora et al. 2014].

While a few small lakes have been observed to disappear or brighten in both the north and south over the 13 years of Cassini observations, no large-scale changes in the sea shorelines have been observed over the course of the mission. Given the resolution of the RADAR, however, this is not surprising. Although confirmed and stable liquid deposits are currently restricted to polar terrain, the equatorial features Hotei and Tui Regiones have been interpreted as possible low-latitude paleoseas [Moore and Howard 2010]. Both regions are surrounded by fluvial networks that appear to converge on a field of radar-bright, lobate, depressions that are morphologically similar to high-latitude lakes [Moore and Howard 2010]. Dark flow-like features identified adjacent to the radar-bright depressions have been interpreted as cryovolcanic deposits [Barnes et al. 2006; Wall et al. 2009], suggesting that both paleo-lakes and cryovolcanic flows may be present at Tui Regio and Hotei Regio [Lopes et al. 2013]. The existence of modern equatorial lakes has been proposed based on the longevity of low albedo localities observed by Cassini VIMS [Griffith et al. 2012; Vixie et al. 2015], although none of these features have been observed in higher-resolution SAR or altimetry datasets of the regions. Ample evidence exists (e.g., at the Huygens landing site) for at least transient liquids at low latitudes, and very flat areas exist that may be lake beds. Indeed, strong specular reflections

were observed at low latitude by the Arecibo radar on Earth (the longest-range radar astronomy experiment conducted to date) before Cassini's arrival, and the favored interpretation at the time was as extant bodies of smooth liquid hydrocarbons [Campbell et al. 2003]. A recent reinterpretation of the Arecibo returns is in progress at the time of this writing [Hofgartner et al. 2014b].

In May 2014, the RADAR acquired nadir-pointed altimetry over Ligeia Mare. The resulting altimetry echoes revealed waveforms that displayed two distinct returns, one from the surface of Ligeia Mare and one from its seabed [Mastrogiuseppe et al. 2014]. The difference in the received timing between these returns was a direct measure of Ligeia's depth (Figure RADAR-18), while the relative intensity difference between the surface and subsurface return was a measurement of the liquid's loss tangent (i.e., absorbance). While several studies—for example, Brown et al. [2008]; Lorenz et al. [2008a]; Lunine and Lorenz [2009]; Cordier et al. [2012]; Cornet et al. [2012]; Ventura et al. [2012]—have used indirect measurements to constrain the depth of Titan's lakes and seas, the altimetry observations over Ligeia represent the first direct measurement of extraterrestrial bathymetry profiles. Following the identification of Ligeia Mare's seabed, several passes of Titan were modified to repeat the experiment over Punga Mare and Kraken Mare [Mastrogiuseppe et al. 2016]. A reprocessing of altimetry data acquired over Ontario Lacus in December 2008 allowed the technique to be applied to Ontario Lacus as well [Mastrogiuseppe et al. 2018]. Ligeia Mare was determined to have a depth of 170 m at the deepest point along the observed track [Mastrogiuseppe et al. 2014] and, in combination with SAR images, the total volume of the basins was found to be around 14,000 km^3 of liquid [Hayes et al. 2016]. The estimated Ku-band loss tangent was $4.4 \pm 1 \times 10^{-5}$ [Mastrogiuseppe et al. 2016]. Assuming a methane-ethane-nitrogen composition and using the laboratory measurements of Mitchell et al. [2015] with the Lorentz-Lorenz formulation, the best-fit loss tangent is consistent with a methane-dominated composition of 71% CH_4: 12% C_2H_6: 17% N_2. As large quantities of liquid ethane should have been produced by photolysis of methane in the upper atmosphere, and as at least trace amounts of ethane have been detected in Ontario Lacus [Brown et al. 2008], the lack of significant ethane—and other higher order hydrocarbons such as propane—in Titan's lakes and seas requires that the ethane be sequestered in reservoirs (e.g., subsurface liquid deposits or sequestration in crustal clathrate hydrate).

To within error, the loss tangents of Punga Mare and the shallower parts of Kraken Mare (Figure RADAR-18) suggested a similar composition to Ligeia [Mastrogiuseppe et al. 2018]. Along most of Kraken Mare the seafloor was not detected, indication that the seas are either too deep or too absorptive in these areas. Within Punga Mare, a clear detection of the subsurface was observed up to 120 m along-track [Mastrogiuseppe et al. 2018]. At Ontario Lacus, however, the loss tangent was observed to be greater ($7 \pm 3 \times 10^{-5}$), consistent with a composition of ~47% CH_4, ~40% C_2H_6, and ~13% N_2,and suggesting an increased abundance of high-order hydrocarbons as compared to the northern seas. This higher loss tangent could be related to an increased abundance of more involatile hydrocarbons and/or nitriles or suspended particulates that represent a lag deposit generated as methane is transported from the south to the north over multiple seasonal cycles. The final RADAR observation of the bathymetry campaign was the T126 (April 22, 2017) final flyby of Titan, which observed several small-to-medium size (10–50 km) hydrocarbons lakes present at the northern polar terrain, revealing that such lakes can exceed one hundred meters of depth and have similar loss tangents, and therefore composition, to the northern seas. When the bathymetry

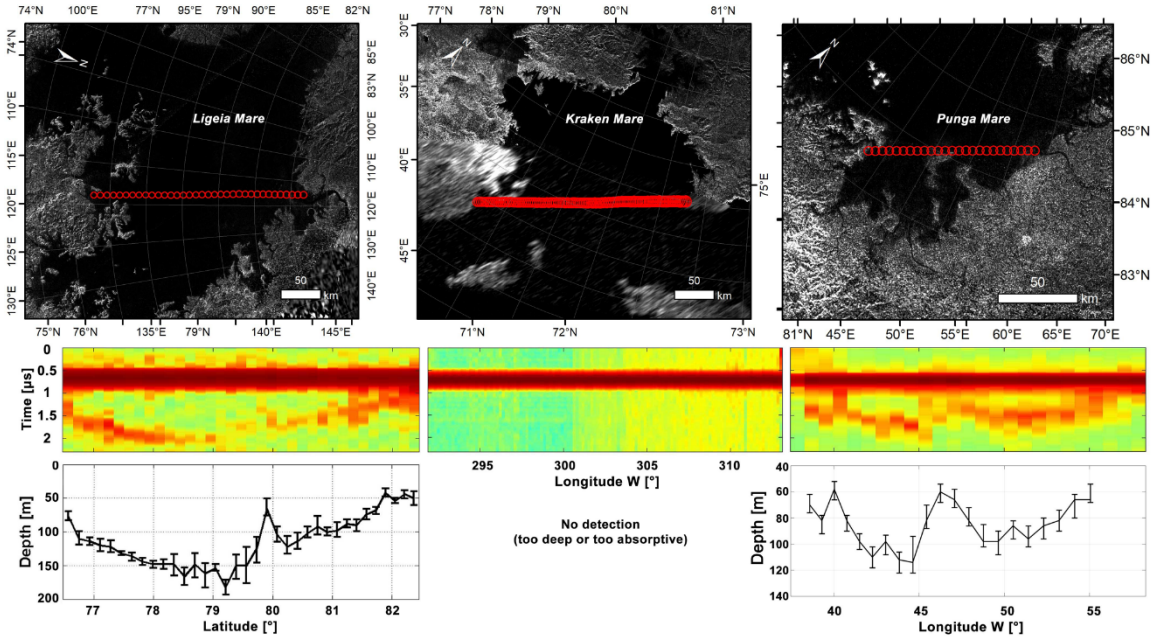

Figure RADAR-18. SAR mosaics, radargrams, and relative bathymetries (respectively in the upper, middle, and bottom panels) relative to the flyby T91 over Ligeia Mare (left), the flyby T104 over Kraken Mare (center), and the flyby T108 over Punga Mare (right) altimetry observations. Note that seafloor echoes have been detected for Ligeia and Punga Maria, while only surface returns are present over the open sea of Kraken Mare.

measurements are used to anchor models of sea and lake depth from SAR images, the estimated volume of all Titan's observed lakes and seas is ~70,000 km^3 [Hayes et al. 2016]. It is interesting to note that this represents only 1/7 the amount of methane that currently resides in Titan's atmosphere, suggesting that the lakes and seas do not drive global-scale heat transport or meteorology. It is also worthwhile mentioning that measuring the bathymetry and microwave absorptivity of Titan's seas was not planned initially and represents an exciting discovery made during the Cassini spacecraft lifetime.

T126 data (together with previous passes) revealed that some of the northern lakes have raised rims. Recent analysis of these features have produced different hypotheses for their origins [Birch et al. 2018a; Mitri et al. 2019].

RIVERS/CHANNELS

When water falls to the surface of the Earth, the most visible conduits on its journey downslope are networks of fluvial channels that slowly transport it toward the oceans. These networks take on many different forms that are the result of the mechanical and chemical properties of the surface [Burr et al. 2006], the climate and weather that generate fluid flow, and the mechanisms that produce topographic relief [Black et al. 2017]. The observation of channels on Titan by Cassini and Huygens [Collins 2005; Lorenz et al. 2008c; Lunine et al. 2008; Burr et al. 2009; Black et al. 2012; Burr et al. 2013] has thus provided similar constraints on the nature of Titan's surface and the

climatic conditions that proved favorable for the formation of these features, albeit in a far more limited fashion.

Cassini's RADAR imaged large portions of the moon and showed that valley networks are distributed at all latitudes [Lorenz et al. 2008c; Burr et al. 2009; Lopes et al. 2010] and have a wide variety of surface morphologies (Figure RADAR-19). Cassini has observed canyon networks at the poles with a diversity of valley networks analogous to Earth [Poggiali et al. 2016], including both dendritic and rectilinear networks globally [Burr et al. 2013], and even a meandering like feature in

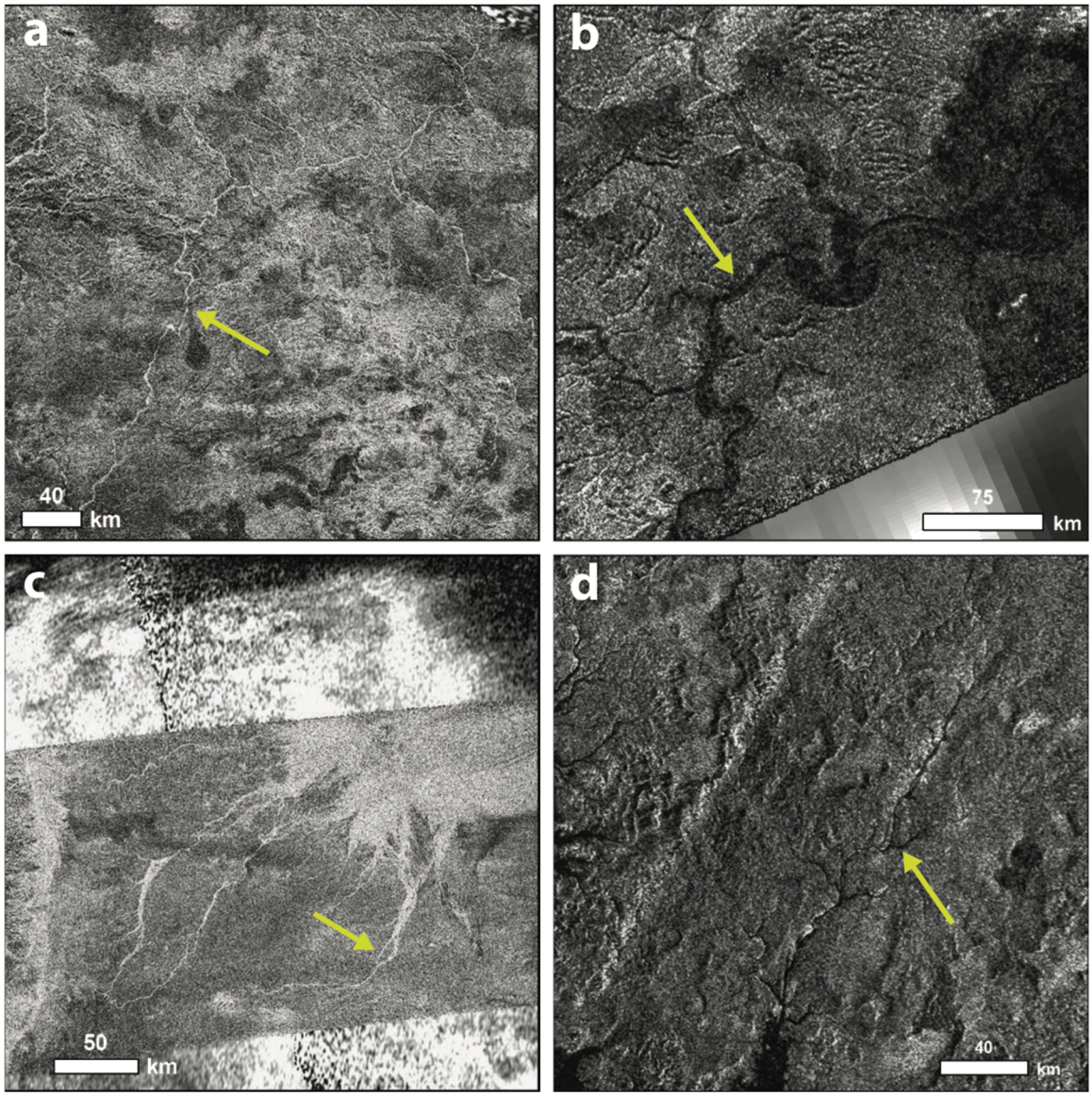

Figure RADAR-19. Erosions on Titan. (a) Rectilinear networks in eastern Xanadu; (b) Celadon Flumina, a meandering network near the South Pole; (c) Elvigar Flumina, a braided network that deposits into an alluvial fan; (d) Vid Flumina, a dendritic canyon network up to 500 m deep that drains into Ligeia Mare.

the south polar region [Malaska et al. 2011b; Birch et al. 2018b]. The presence of canyons implies a vertically weak bedrock, which may be influenced by fractures in the crust and/or a relatively highly erodible material. Similarly, rectilinear channels imply a fractured bedrock, where channels are forced to follow tectonically controlled paths of weakness. Meandering networks, meanwhile, imply the presence of a cohesive substrate [Howard et al. 2009]. A critical unknown following the Cassini mission, however, is whether there are any systematic variations in morphologic type that may be indicative of crustal heterogeneities [Burr et al. 2013] and/or variations in transport efficiencies/climate change [Moore et al. 2014].

Due to the coarse resolution of the Cassini RADAR, we have been limited to studying only the largest valley networks on Titan. We therefore have a limited idea about the extent to which Titan's landscapes are dissected by fluvial networks. The one exception to this was the region where the Huygens lander descended, where descent images, with an order-of-magnitude higher resolution [Tomasko et al. 2005], showed a highly dissected network of dendritic valleys [Perron et al. 2006]. It is likely that Titan is dissected everywhere at the scale observed by Huygens, however, a definitive answer to this question requires image data and topography with a resolution finer than the scale of fluvial dissection (10s of meters).

While it is not surprising that Titan has a global network of fluvial valleys, the mere presence of channelized flow conduits implies that the surface material can be eroded either physically or chemically, and that flows of sufficient magnitude, either from precipitation or groundwater, are able to erode Titan's surface. However, using estimates for the initial topography and erodibility of the substrate, channels may be very inefficient agents of erosion on Titan [Black et al. 2012] or there may be a gravel lag deposit that inhibits erosion under Titan's current climate [Howard et al. 2016]. Better estimates for the physical and chemical properties of both the bedrock and the fluid(s) [Burr et al. 2006; Cordier et al. 2017; Malaska et al. 2017a; Richardson et al. 2018] are needed to provide better understanding about the role that fluvial channels have played in sculpting Titan's surface.

In some locations, fluvial channels terminate in alluvial or fluvial fans—distributary landforms that indicate a transition from a high to a low elevation [Radebaugh et al. 2017; Birch et al. 2017]. These are fairly low in slope, and in some cases can run out to large distances, indicating the carrying power by methane fluid of organic sedimentary rock [Radebaugh et al. 2017]. These landforms are widely distributed across the surface, but they are not abundant [Birch et al. 2017]. This may indicate there is not frequent rainfall that can generate surface erosion, or that topographic gradients are gentle on a global scale such that these landforms are not readily generated.

Temporal change

Temporal changes were detected on Titan during the course of the Cassini mission, due to seasonal or other effects. Data from more than one instrument are key for determining the possible causes of change. For example, as mentioned in the section entitled Cryovolcanism, the radiative transfer code analysis of VIMS data from Tui Regio (2005–2009) and Sotra Patera (2005–2006) showed temporal surface albedo changes in two areas identified by SAR as cryovolcanic

candidates: Tui Regio darkened by 50% and Sotra Patera brightened by a factor of 2 [Solomonidou et al. 2016]. These changes could be due to endogenic and/or exogenic processes, possibly cryovolcanism or atmospheric deposition.

Magic Islands

For the majority of the Cassini mission, Titan's lakes and seas were observed to be quiescent, with no temporal changes and maximum vertical surface roughness on the order of millimeters [Barnes et al. 2011b; Stephan et al. 2010; Wye et al. 2009; Zebker et al. 2014; Grima et al. 2017]. This lack of observable surface roughness has been attributed to a seasonal effect in which polar winds were too weak to create waves or other dynamic features [Hayes et al. 2013]. As the northern hemisphere transitioned from spring equinox to summer solstice, temporal changes were observed in all three of Titan's seas. Specular reflections offset from the geometric specular point were observed by VIMS in Punga Mare [Barnes et al. 2014], transient bright features were observed by RADAR in Ligeia Mare [Hofgartner et al. 2014a, 2016], and both offset specular reflections and transient radar-bright features were observed in Kraken Mare [Hayes et al. 2016].

The transient bright features were nicknamed "Magic Islands" due to their appearing/disappearing act and similarity in appearance to islands in SAR images.

The transient radar-bright features were nicknamed "Magic Islands" due to their appearing/disappearing act and similarity in appearance to islands in SAR images. The features are not islands, however, and are most consistent with waves, or floating and/or suspended solids and bubbles. Based on the frequency of these phenomena in analogous terrestrial settings, wind-driven waves (intended to mean roughness of the liquid surface regardless of the process causing the roughness) are the most probable hypothesis. Tides, changes of sea level, and changes of the seafloor are unlikely to be the primary cause of the temporal changes. Magic Islands were observed in three regions; two in Ligeia Mare [Hofgartner et al. 2014a, 2016] and one in Kraken Mare [Hayes et al. 2016].

Figure RADAR-20 shows the time evolution of the first and most observed Magic Island region. This region was observed to have Magic Islands on two occasions; the transient bright features were in the same location on both occasions but differed in areal extent and morphology. HiSAR and VIMS observations acquired between the two SAR detections did not detect Magic Islands, however, the possibility that the Magic Islands were present but not detected in these observations could not be ruled out. Magic Islands were definitely not present in SAR observations before the first appearance and after the second appearance (Figure RADAR-20 includes a subset of the images of the region).

The Kraken Magic Island was also observed as a 5-micron sunglint by VIMS within two hours after the radar detection. The co-detection of the Kraken Magic Island by both RADAR and VIMS

suggests that it is likely caused by surface waves, as the reflecting facets must be smooth at both microwave and micron length scales [Hayes et al. 2016].

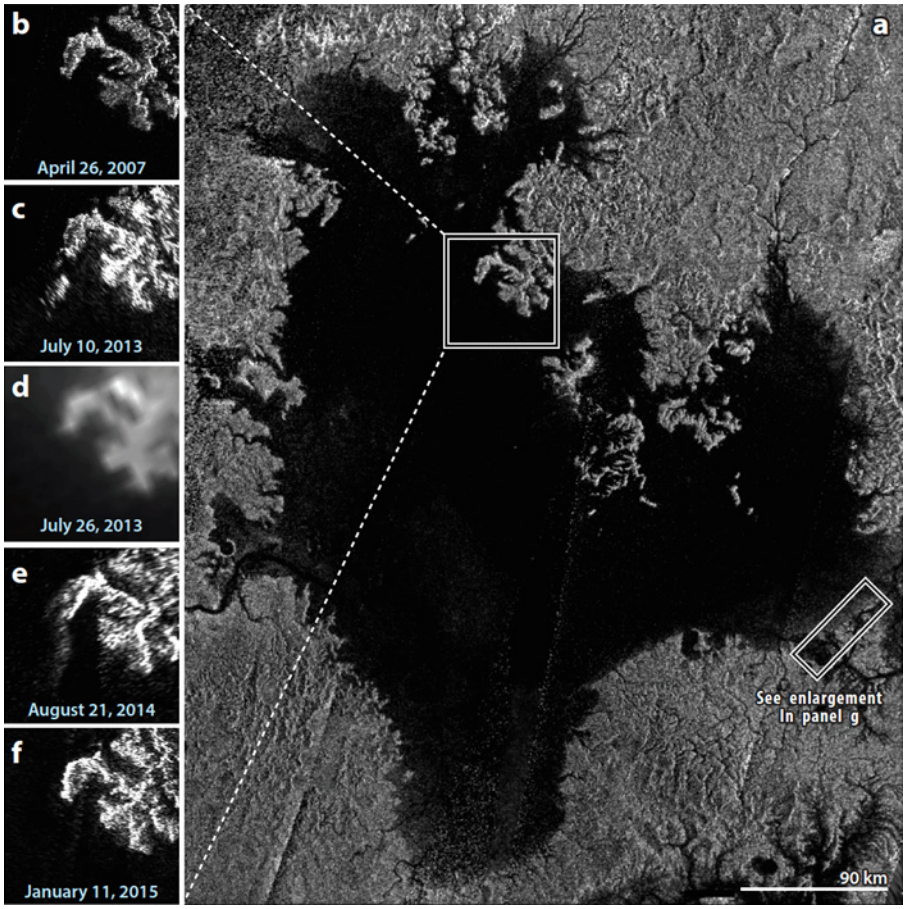

Figure RADAR-20. Time evolution of the first and most observed Magic Island region. The large panel on the right is a SAR mosaic of Titan's hydrocarbon sea, Ligeia Mare. The panels on the left show the temporal variation of a region observed to have Magic Islands. Transient bright features (Magic Islands) are observed in the images from July 10, 2013 and August 21, 2014 that are not present in any other images of this region [Hayes 2016]. The VIMS observation on July 26, 2013 (panel d) did not detect Magic Islands, however, the possibility that they were present but not detected in these observations could not be ruled out. Magic Islands were definitely not present in SAR observations before the first appearance and after the second appearance. The figure shows only a subset of Cassini observations of the region, see Hofgartner et al. [2016] for all observations with a resolution sufficient to observe the Magic Islands.

ARRAKIS PLANITIA PRECIPITATION AND OTHER TRANSIENT EVENTS

The first Cassini observations of surface change on Titan were obtained over Arrakis Planitia, near the South Pole, where ISS observed the appearance of dark splotches (interpreted as ponded hydrocarbon liquid) in June 2005 that were not present in the previous observation acquired in July 2004 [Turtle et al. 2009]. In October 2004, between those two observations, a large cloud outburst was observed near Titan's South Pole from Earth-based telescopes [Schaller et al. 2006].

SAR images and SARTopo later found that the ISS dark splotches occurred in topographic depressions that are morphologically similar to steep-sided depressions interpreted as empty lakes in the north [Soderblom et al. 2016]. VIMS observations of this area acquired between 2007 and 2009 show that the dark splotches had become brighter than the surrounding terrain [Soderblom et al. 2016]. SAR images of the area obtained in October 2007 and December 2008 showed the absence of dark splotches in the same topographic depressions, this time in the microwave, that were interpreted as either the evaporation or infiltration of ponded liquid [Hayes et al. 2011].

In addition to Arrakis Planitia, temporal changes have also been observed at other locations in the South Pole as well as within the northern lakes and seas and at equatorial latitudes. The largest observed surface change occurred in 2010 when an equatorial area of over 500,000 km in size was observed to darken, presumably by methane precipitation, after a chevron-shaped cloud passed over the region [Turtle et al. 2011]. SAR images of the area suggest that the darkened region represented local topographic lows. The area was later observed to return to its original albedo [Barnes et al. 2013]. Whereas there have been no definitive changes observed in the shorelines of the northern lakes and seas through April 2017 (flyby T126), there have been several surface changes reported for lacustrine features in the south polar region. Turtle et al. [2011] argued for shoreline recession at Ontario Lacus between ISS images acquired June 2005 and March 2009, although the poor resolution of T51 makes quantitative measures difficult. Hayes et al. [2011] found that, while inter-instrument comparisons can be dangerous, SAR images acquired in 2009 (T57/T58) and 2010 (T65) were consistent with a receded shoreline when compared to the June 2005 images obtained by ISS. However, Cornet et al. [2012b] argued that, to within measurement error, the data are consistent with no changes at all. Hayes et al. [2011] also discussed repeat RADAR passes of the south acquired in 2007 and 2008/2009 that contain lacustrine features that seem to disappear between subsequent SAR observations. The observed ten-fold increase in SAR backscatter cannot easily be explained by geometric effects and suggests that, between the observations, liquid either infiltrated into the ground, evaporated, or did both [Hayes et al. 2011]. Other temporal changes, including roughening events interpreted as wave or fluvial activity as well as Titan's mysterious magic islands have been observed within the northern seas. These changes are discussed in the section entitled Magic Islands.

Although the Cassini mission's exploration of Titan's methane cycles has ended, ground-based observations can continue to monitor Titan's weather until future missions can map fluvial features at a higher resolution and characterize the composition of surface material (including the lakes and seas) through in situ exploration.

Observation of a Summer Lag in the North Pole (by Radiometry)

One of the main scientific objectives of the Cassini Extended Mission (2008–2017) was to monitor the changing seasons on Titan. If any change were to occur, it should be primarily in Titan's arctic regions where the most important temperature variations are expected (though limited to 2-4 K over the course of a year).

Onboard Cassini, both the Composite Infrared Spectrometer (CIRS) and the microwave radiometer had the ability to measure the variations of surface/near-surface temperature with time [Jennings et al. 2009; Cottini et al. 2012; Janssen et al. 2016] and both instruments observed a lag in the summer warming of the northern polar terrains [Jennings et al. 2016; Le Gall et al. 2016]. They reported a much slower rise of temperature in late spring (2014–2015) than predicted by a global circulation model (GCM), even assuming a very high thermal inertia for lakes and seas [Tokano 2005]. Further, there seems to be no significant temperature difference between the land and the seas, which suggests that the solid surface surrounding the lakes and seas of Titan are saturated with liquid and behave thermally like the liquids. They may as well experience evaporative cooling which would explain the low measured temperatures in the north polar region and have important implication for the hydrocarbon cycle on Titan.

Surface and atmosphere interaction

Winds and temperature

In contrast to the contemporary instantaneous winds revealed by sea surface roughness (see section entitled Major Geologic Units and Mapping), the widespread observations of dunes on Titan attest to winds that have acted over significant periods in the past, and indeed the possibility that aeolian landforms might shed light on Titan's climate history was recognized before Cassini's launch—for example, Lorenz et al. [1995]. Since so few trackable cloud features have been observed on Titan, the aeolian features in Titan's landscape have emerged as one of the principal constraints on Titan's meteorology. Specifically, it has been estimated that the saltation threshold for the movement of dry sediment on Titan requires surface winds of the order of 1 m/s—for example, Greeley and Iversen [1987], Lorenz et al. [1995], and Lorenz [2014]. This estimate is based on an assumption of interparticle cohesion not too different from terrestrial sands: some laboratory measurements suggest they could be slightly larger [Burr et al. 2015] and it is possible or even likely that (methane/ethane) moisture [Yu et al. 2017] and/or electrostatic charging [Lorenz 2014; Mendez-Harper et al. 2017] could be responsible for stronger cohesion. In any case, the presence of dunes requires winds sometimes exceeding this threshold in the past.

The construction or reorientation time for dunes of the size (~100 m tall) observed by Cassini is substantial, of the order of 50,000 years [Ewing et al. 2015; Lorenz et al. 1995; Lorenz 2014]. Thus, not only does the presence of dunes require that the winds have been above the saltation threshold for a substantial integrated period, but also that the dune pattern observed today retains some memory of winds extending into the past by a substantial part or multiple of an astronomical (Croll-Milankovich) climate cycle—see, for example, Aharonson et al. [2009]; Lora et al. [2014]. In particular, Ewing et al. [2015] noted that some of Titan's dunes are somewhat crescentic, implying a recent dominance of a northward meridional component to the winds—see McDonald et al. [2016].

The generally-eastwards direction of sand transport implied by the dune morphology was noted early [Lorenz et al. 2006; Radebaugh et al. 2008; Lorenz and Radebaugh 2009] and was a

challenge to meteorological expectations, since low-latitude near-surface winds should have on average an easterly (westwards) flow, much like the trade winds on Earth. Tokano [2008] made some of the first systematic experiments with a GCM to attempt to reproduce the observed pattern by positing the influence of Xanadu as a highland or bright region. The vexing paradox—see for example Lorenz and Zimbelman [2014]—was resolved by invoking occasional westward gusts [Tokano 2010; Charnay et al. 2015] such that even though the average wind direction is eastwards, these typical winds are below the threshold speed and so are not reflected in the sand transport. Thus, the landscape is shaped only by the stronger (westward) gusts—with the saltation threshold acting like a diode in an electrical analogy of alternating winds. Tokano [2010] found that a threshold of order 1 m/s was consistent with obtaining a dune pattern similar to that observed, and suggested that stronger vertical mixing in the low-latitude troposphere during the equinox period might cause the required westward flows. This idea has been developed somewhat further by Charnay et al. [2015], who suggested that methane rainstorms in particular may be responsible. Significant developments in the mapping of dune morphology and orientation to wind diversity and sand supply/mobility have taken place in the last decade and a half, stimulated in no small part by the Cassini discovery of large linear dunes as well as other wind-borne features [Lorenz and Radebaugh 2009; Malaska et al. 2016a]. Detailed observations suggest that there is a divergence of material transport in the equatorial regions, and a convergence in the mid-latitude regions around latitude 35°. This suggests that a relationship exists between two major land units on Titan: the longitudinal dunes and the undifferentiated plains, as discussed in the section entitled Plains. It has been suggested [Rubin and Hesp 2009] that sticky sand may yield longitudinal features, and laboratory results with organic material have shown that electrostatic charging may be significant for Titan organics under cryogenic, dry conditions [Mendez-Harper et al. 2017]. Nonetheless, the interaction of multiple modes of dune growth may be important in decoding Titan's winds from dunes—for example, Lucas et al. [2014].

In contrast to the complex wind story, the overall distribution of dunes on Titan is somewhat straightforward from the standpoint of wetness. Early Titan GCM studies—for example, Rannou et al. [2006]; Mitchell [2008]—indicated that Titan's low latitudes should be dried out by the general circulation, as a result of the meridional (Hadley) cells on this slowly rotating world. Thus, the dunes form a broad equatorial belt on Titan, whereas they form belts at about 20 degrees north or south on the faster-rotating Earth. The size and spacing of dunes, assuming that they have been allowed to grow to their full extent without being limited by growth time or sand supply, has been determined—for example, Andreotti et al. [2009]—to correlate to the thickness of the atmospheric boundary layer. Essentially, the layer caps the dune growth once the spacing is roughly equal to the layer thickness. Lorenz et al. [2010] showed that the Huygens descent data were consistent with a boundary layer thickness of the order of 3 km, matching the typical dune spacing on Titan. Extensive dune spacing measurements—for example, Le Gall et al. [2011], and Savage et al. [2014]—show only small minimal variations with latitude. Charnay et al. [2012] found that a GCM with an improved boundary layer scheme reproduced the 3 km thickness, interpreting this as a seasonal boundary layer.

The full meteorological interpretation of the dune pattern revealed by Cassini's RADAR will require a finer scale of modeling than has been performed so far, including regional topography

and albedo effects. It may be that the dune fields, by virtue of having a low thermal inertia and albedo, cause their own sea breeze effect, modifying the local winds. The role of evolving ground moisture remains to be elucidated, although some hints of moisture effects on ground thermal inertia have been suggested in the RADAR radiometry data [Janssen et al. 2016].

Although the radiometer in principle is an indicator of surface temperature and could be used to independently constrain gradients with latitude etc. [Lorenz et al. [2003], in practice, the surface temperature estimates from the Cassini CIRS and the Huygens probe have been adopted as ground truth and the interpretation of the microwave radiometry has been principally in terms of the surface dielectric properties. However, future studies might profitably examine small-scale radiometer variations and their correlation with surface elevation—in principle, the ~1 K/km lapse rate may have a signature in surface brightness temperature.

METHANALOGIC CYCLE

Titan is the only place in the solar system, other than Earth, that is known to have an active hydrologic cycle.

Titan is the only place in the solar system, other than Earth, that is known to have an active hydrologic cycle. Titan's methane-based hydrologic cycle is an extreme analog to Earth's water cycle. Exchange processes between atmospheric, surface, and subsurface reservoirs produce methane and ethane cloud systems, as well as erosional and depositional landscapes that have strikingly similar forms to their terrestrial counterparts. Over its 13-year exploration of the Saturn system, Cassini has revealed that Titan's hydrocarbon-based hydrology is driven by nested methane cycles that operate over a range of timescales including geologic, orbital, seasonal, and that of a single convective storm. A fast physical (phase change) cycle drives active weather and fluvial processes over seasonal to orbital timescales. A medium-paced chemical cycle siphons off methane for photochemical synthesis in the upper atmosphere, depositing the products on the surface over timescales of millions of years. A long-term geologic cycle may sporadically inject methane into the system from Titan's interior over the age of the solar system. For a recent review of Titan's hydrologic cycle, see Hayes et al. [2018].

Titan as a system

Titan is the only moon in the solar system with an atmosphere so massive that it dominates the total volatile inventory in the surface-atmosphere system and provides strong radiative forcing and an active meteorology [Lorenz et al. 2005]. It also obscures the surface from view in both the optical and infrared, which is why the Cassini RADAR has been such a crucial tool. However, by the irreversible deposition of heavy hydrocarbons, nitriles, and other photochemical products from methane and nitrogen, the atmosphere also obscures the underlying surface geology to some extent. Were the current inventory of methane to condense onto the surface, it would form a layer 5 m thick [Mitchell and Lora 2016], but a variety of evidence suggests that many times that number is present in various solid and liquid deposits of organics on and within the crust [Hayes et al. 2018].

Therefore, Titan's geologic history is poorly constrained and in particular there is a significant uncertainty as to what fraction of the body's 4.5 billion years of existence is recorded on the surface. Observations relevant to its history include:

1. The low observed numbers of impact craters [Porco et al. 2005] yield an age of hundreds of millions of years, not billions [Lorenz et al. 2007; Wood et al. 2010; Neish and Lorenz 2012].

2. The rate of photodissociation of methane in Titan's atmosphere implies that the current gaseous inventory will be depleted in some tens of millions of years [Yung et al. 1984].

3. Titan's interior has at least partially differentiated, resulting in a rock-metal core, a high-pressure ice mantle of uncertain thickness, a liquid water ocean [Iess et al. 2010] perhaps with salts and ammonia [Mitri et al. 2014], and an ice crust 50 to 150 km thick. The core is either significantly hydrated [Castillo-Rogez and Lunine 2010], or there is a mixed rock-ice layer somewhere in the interior [Tobie et al. 2014].

4. A range of chemical and physical data from the atmosphere to the interior suggest that a significant event, or change in the way Titan evolves, occurred sometime between a few hundred million and a billion years ago [Horst 2017].

The relatively youthful age of the surface, which may be the result of geologic activity, older impacts occurring on surfaces covered by liquids [Neish and Lorenz 2014], extensive erosion, or substantial burial in organic matter, means that there is little if any geologic evidence of the first 3/4 of Titan's history. Two unanswered questions are: 1) what was the process/processes that eroded or covered older impact craters and other landforms; and 2) did the obscuration of features older than a few hundred million years occur continuously over time, or in some singular event?

There is no evidence of the answer to the second question, but a theoretical model of the evolution of Titan's interior by Tobie et al. [2006] provides an intriguing scenario that implies Titan had a significant change in the working of its interior, crust, and atmosphere about 500 million years ago [Wood 2018]. In the Tobie et al. [2006] model, Titan had a thin and rigid clathrate crust—with methane as the dominant guest species—up until 500 million to one billion years ago. During that earlier epoch, several major heating events resulted in the release of large (compared to the present atmospheric inventory) amounts of methane from the clathrate hydrate into the surface-atmosphere system. Within the last 500–1000 million years the interior has cooled sufficiently to allow an ice I crust to form underneath the buoyant clathrate hydrate crust, with diapirism in the thickening ice I crust providing one or several episodes of further release of methane into the surface-atmosphere system.

Wood [2018] called the onset of the ice I subcrust the Great Crustal Thickening Event and noted that the mode of geologic processes would change dramatically as Titan transitioned from a

body with a thin rigid conductive crust over the ocean to one with a thicker and rheologically heterogeneous crust.

Models of Titan's interior look broadly similar but with substantial disagreements on the thickness of the high pressure ice layer and the extent of silicate core hydration [Tobie et al. 2014]. How much this affects the surface evolution is unclear. While the idea is commonly held that the source of the methane to resupply the atmosphere is in crustal clathrate hydrate—such as that predicted in pre-Voyager days [Lewis 1971]—how the resupply works is unclear. Simple forcing out of the methane from the clathrate by the photochemically produced ethane eventually fails because of the stoichiometry (two methane molecules making one ethane), although this replacement could eventually weigh down the crust and cause an overturn because clathrate with predominantly ethane is heavier than ice I [Choukroun and Sotin 2012]. This could cause interesting geologic consequences in the present era when the clathrate is nominally underlain by warm ice I. Whether the methane hydrological cycle that we see today shaping so many aspects of Titan's surface is ancient or recent, episodic [Lunine et al. 1998] or continuous, remains a mystery that may be directly coupled to the poorly understood interior evolution. Or it may reflect a series of external events whose record in the Saturn system has yet to be properly read.

Birch et al. [2017] have pointed to geologic evidence (notably the presence of large sedimentary deposits) suggesting that the present epoch of lakes and seas of methane, ethane, and nitrogen might have been preceded by one with a widespread ocean of methane and other hydrocarbons. The longevity of such an ocean, in particular its decline, may be constrained by the limits on tidal dissipation of the orbital eccentricity during ocean shrinkage [Sagan and Dermott 1982; Sears 1992], since we now have measured global Titan topography. Finally, it is possible that Titan has run out of atmospheric and surface methane multiple times in its history, leading to dramatic atmospheric changes [Lorenz et al. 1997] and possibly epochs in the which the surface is worked by liquid nitrogen seas and rivers [Charnay et al. 2014].

If Titan's geologic and atmospheric nature have changed in a secular way over its history, it would join the other terrestrial planets—Venus, Earth, and Mars, in this regard. In each case, interior and surface-atmosphere changes over time have led to present-day characteristics that are likely to have been dramatically different from those in the past.

Open questions

Now that we have a global view of Titan contributed by several Cassini instruments, the questions that remain become more detailed and in general require more than one data type to address. Some also require a different type of sensing platform as well. NASA plans to send a rotorcraft to Titan called Dragonfly, scheduled to launch in 2026 and land in 2034 [Lorenz et al, 2018; http://dragonfly.jhuapl.edu/]. Dragonfly's primary objective is to look for prebiotic chemical processes, and it will also address open questions atmospheric, surface and subsurface properties. Other open questions are addressed in Lunine's Interdisciplinary Scientist (IDS) report on Titan elsewhere in this report.

Below we list a subset of those questions that might be addressed by future spaceborne radar instruments, keeping in mind that they have proven to be a challenge from several standpoints. In fact, because of Cassini's success, the minimum orbiter science payload considered worthwhile for such purposes is now fairly large [Reh 2007].

Direct benefit from higher resolution (<100m) SAR

- To what extent is the surface fluvial dissected?
- How do the organic compounds produced in the atmosphere evolve on the surface?
- Does cryovolcanism occur on Titan?
- What is the composition of the dune particles and how are they produced?
- What is the nature of the asymmetry in seasonal effects?

Indirect benefit from higher resolution SAR/HiSAR/scatterometry/ altimeter

- How did the lakes and sea basins form?
- What is the organic and inorganic composition of the surface?
- What is the circulation in the lakes and seas and how is it affected by the atmosphere?
- What is the salinity and composition of the deep ocean and is it in contact with rock beneath?

Direct benefit from a radar sounder

- What is the nature and extent of the exchange between the surface/atmosphere and deep subsurface and ocean?
- What is the depth and thickness of the subsurface ocean?

Saturn Science

Introduction

The thermal emission from the gas-giant planets was first observed by single-antenna telescopes in the 1950s [Mayer 1958], and quantitatively related to fundamental atmospheric properties in the following decade [Thornton and Welch 1963; Gulkis et al. 1969; Wrixon and Welch 1970]. Subsequent observations through the 1980s filled in the disk-temperature spectra of Jupiter and Saturn through the millimeter- and centimeter-wavelength range. This combined with advances in understanding the high-pressure microwave absorption of ammonia, which possesses a strong inversion band just longward of 1 cm wavelength, led to a consistent story of deeply convective

atmospheres with ammonia as the dominant absorber [Gulkis and Poynter 1972; Berge and Gulkis 1976; Klein and Gulkis 1978]. The advent around the same time of radio interferometers capable of using aperture synthesis to image the planets led to the first microwave image of Saturn, reported by Schloerb et al. [1979] using the interferometric Owens Valley Radio Observatory at 3.7 cm wavelength. The completion of the National Radio Astronomical Observatory's Very Large Array (VLA) in New Mexico was followed by a series of images of Saturn and its rings made with this instrument reported by a number of authors at wavelengths ranging from 2–21 cm wavelength (de Pater and Dickel [1982, 1991]; Grossman et al. [1989]; Grossman [1990]). These studies have resulted in a better understanding of Saturn's rings and atmospheric microwave spectrum, and have provided evidence of large-scale structure in Saturn's ammonia distribution including variable broad bands in the mid-latitudes. However, they have been limited by the capabilities of the VLA in spatial resolution and dynamic range for imaging extended objects; in addition, the process of Earth-rotational aperture synthesis used for imaging averages out longitudinal structure.

The microwave radiometer contained in the Cassini RADAR provides a unique opportunity to image Saturn with the advantage of close range and without the limitations of a ground-based approach other than the restriction to a single wavelength. This has resulted in nearly an order-of-magnitude improvement in both spatial resolution and sensitivity over Saturn microwave observations published up to the Cassini era, although improvements made to the VLA since then promise to close this gap. In this report we summarize the mapping campaign of Saturn carried out by the RADAR radiometer during the Cassini mission and its main results, leaving the details to papers already in the literature.

Observations

The thermal emission from Saturn's atmosphere was mapped globally on six occasions by the RADAR radiometer at its single wavelength (2.2 cm) and half-power beamwidth of 0.36°. Imaging was achieved by controlling the spacecraft orientation to scan the source using the spacecraft momentum wheels to scan back and forth from pole to pole. We obtained six global maps of the 2 cm thermal emission from Saturn distributed over a period from 2005–2015, each obtained using a period of approximately 14 hours centered on an equatorial periapsis pass. The motion of the spacecraft and Saturn's rotation combined to provide nearly complete global maps of Saturn in each pass. Janssen et al. [2013] presented the first five of these maps and described in detail the techniques used, calibrations, and general interpretations. A companion paper by Laraia et al. [2013] focused on the interpretation in terms of the ammonia vapor distribution in the ammonia cloud and sub-cloud region. A sixth map was obtained in May 2015 and a paper presenting its results is in preparation at the time of this report.

The five published maps are shown in Figure RADAR-21 as cylindrical maps of brightness temperature relative to a model Saturn atmosphere with nominal composition and fully saturated ammonia—for example, 0 K in the map indicates an absolute brightness as given by the fully

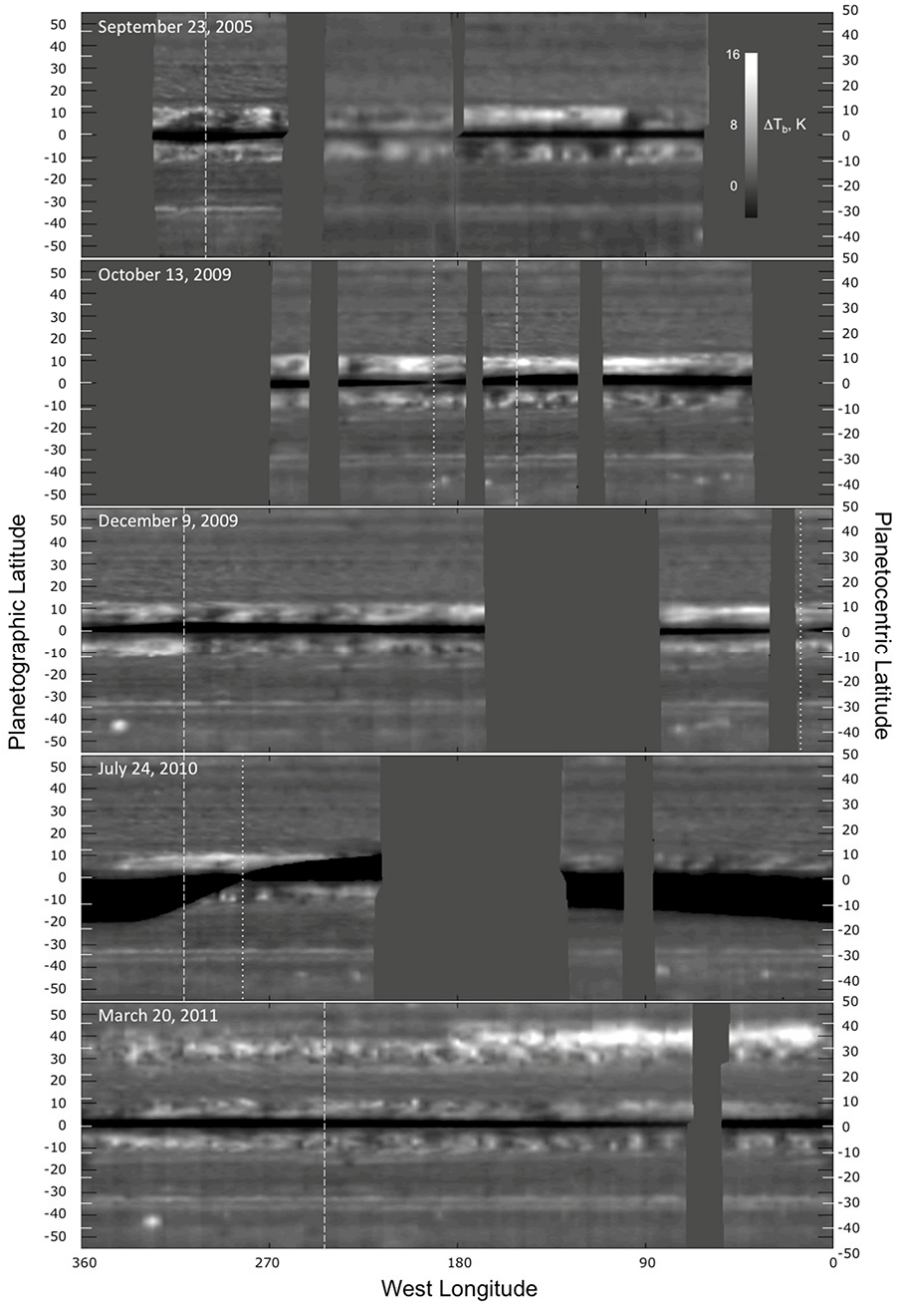

Figure RADAR-21. Global cylindrical maps of Saturn's thermal emission obtained at 2.2 cm wavelength during the Cassini prime and equinox missions. This was obtained by accumulating north-south scans from pole to pole during an approximately 14-hour period surrounding Saturn periapsis.

saturated model (see section entitled Key Objectives for RADAR Instrument). The Saturn brightness measurements themselves were calibrated to an absolute accuracy approaching 1% by transferring absolute calibrations obtained from Titan observations [Janssen et al. 2009, 2016] to Saturn. All observations were made during periods in the mission when the spacecraft was in Saturn's equatorial

plane. The inclination of the rings as seen by the spacecraft was less than 1° for all observations except for that of July 24, 2010 where it approached 4°. The dark band with variable width seen in the equatorial region is due to blockage by the rings. Gaps indicated by the uniform grey shading (corresponding to 0 K relative brightness) are lapses in data-taking where time had to be taken to unload the spacecraft momentum wheels. The dashed and dotted lines indicate periapsis and ring plane crossings respectively (there were no observations made exactly at ring plane crossing for the 2005 and 2011 maps). Planetographic latitudes are indicated by black ticks on the vertical scales, planetocentric by white. Mapping of the regions outside approximately ±50° latitude is of lower quality because of high emission angle and the results obtained there are not shown. The resolution in latitude is as good as 0.86° at the equator, and the sensitivity of each observation is ~0.1 K. The longitude resolution is limited by the scan rate of the spacecraft but averages about 2° at the equator.

Interpretation

The maps are interpreted in terms of a reference model for Saturn's atmospheric structure and composition based on Atreya [2010] and shown in Figure RADAR-22, using current values for the known constituents of the atmosphere [Hanley et al. 2009; Deveraj 2011]. The weighting function in

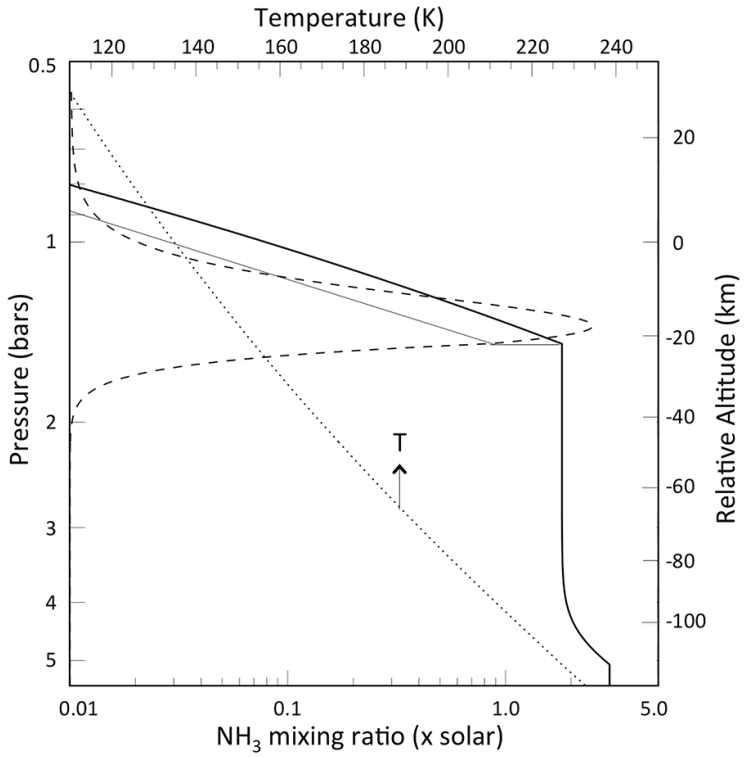

Figure RADAR-22. Atmospheric model used to compute reference brightness temperatures. The temperature (dotted line) and NH_3 mixing ratio in units of solar abundance (thick solid line) are shown as a function of pressure and altitude in the vicinity of the ammonia cloud region in the atmosphere. The reference model assumes 100% relative humidity for ammonia above its saturation level, while the light solid line shows a case for 50% relative humidity. The decrease in NH_3 mixing ratio above the 5-bar level is due to reaction with H_2S to form NH_4SH ice. The dashed line shows the 2.2 cm wavelength weighting function in arbitrary linear units at normal incidence for the reference model.

Figure RADAR-22 shows the region responsible for the thermal emission assuming that the ammonia is fully saturated in the cloud region. In this model, the microwave absorption, and hence thermal emission, is seen to be due almost entirely to gaseous ammonia and is located primarily within the ammonia cloud region. Any depletion of ammonia relative to the fully saturated model leads to excess brightness. The maps indicate that the ammonia cloud region is everywhere unsaturated (at least away from the equator where the atmosphere is blocked by the rings), and variations in the ammonia can be expected to trace atmospheric circulations in and below the clouds.

The maps in Figure RADAR-21 reveal features either never before seen or known features viewed from a perspective never before available. The region of the atmosphere responsible for the microwave brightness variations, roughly 0.5 to 2 bars, has been extensively observed with high-resolution instruments at infrared wavelengths. Nevertheless, the unique value of observations at 2.2 cm wavelength is the simple origin of the observed structure—it is just ammonia vapor and variations in its distribution. Low residual brightness indicate the presence of gas phase ammonia in the cloud region at concentrations approaching but not exceeding its saturation level, whereas higher brightness indicates a relative depletion. The variability of the brightness distribution across Saturn suggests the existence of circulations that cause the depletion or enhancement of the ammonia by means of gas flow into and out of the ammonia condensation region, while the morphologies of these variations give clues as to the nature of the dynamical forcing causing these flows. Obvious features include the bright bands that are symmetric about the equator from approximately 3° to 10° latitude north and south respectively, where regions of high brightness alternate with low brightness regions resulting in longitudinal variability not seen at higher latitudes (until the Great Northern Storm in the 2011 map). These regions are similar to Jupiter's equatorial belts as seen recently by the Juno microwave instrument on the Juno spacecraft [Bolton et al. 2017]. The regions of high brightness in these bands are dry in the sense of low ammonia abundance, and therefore resemble the dry sub-tropics of Earth.

In between the north and south equatorial bands, at the equator, is a central band of relative calm with the lowest brightness seen on Saturn, similar to that seen by Juno in Jupiter's equatorial zone. The low brightness seen here indicates ammonia concentration to be near saturation, consistent with the greatly enhanced NH_3 abundances found by VIMS in this region [Fletcher et al. 2011]. Although difficult to discern because of the ring blockage, this band is apparent at or near the ring crossings, most notably in the central segment of the 2005 map. Although at relatively low resolution, the ring inclination in this segment is near 0.01° as seen from the spacecraft, with the blockage causing less than a 1 K influence on the brightness. Laraia et al. [2013] present a more thorough examination of the ring blockage, using a ring model to retrieve the equatorial brightness at the ring plane crossings for all maps to confirm the presence of generally uniform near-saturated ammonia in the equatorial belt.

We investigated the significance of these maps more quantitatively by assuming a simple model for the ammonia distribution. In particular, we allowed the ammonia concentration to vary only in the cloud region only, assuming that it could be described there by a constant relative humidity (RH) in the range 0% < RH < 100%. Figure RADAR-23 shows an analysis using this model carried out by Laraia et al. [2013] of the March 2011 map, which fortuitously captured the Great

Northern Storm of 2010–2011 in progress. The map in panel (a) shows the relative humidity derived from the relative brightness and illustrates that, in general, most of the variation in brightness can be interpreted as variation of ammonia within the cloud region. Significantly, some regions cannot be described this way since the brightness temperature exceeds the model brightness with all cloud ammonia removed. Hence, in these regions, some of the sub-cloud ammonia must be removed as well. The Great Northern Storm (seen in panel (b) around the same time by the Imaging Subsystem) had progressed about halfway around the globe at the time of this map, and shows a dramatic decrease in ammonia extending well beneath the clouds. This supports a model describing the cause and consequences of this storm that predicts such an ammonia depletion [Li and Ingersoll 2015]. The north and south equatorial belts, and isolated storms in a region near 40°S latitude, show evidence of such strong depletion in this map, and all others as well.

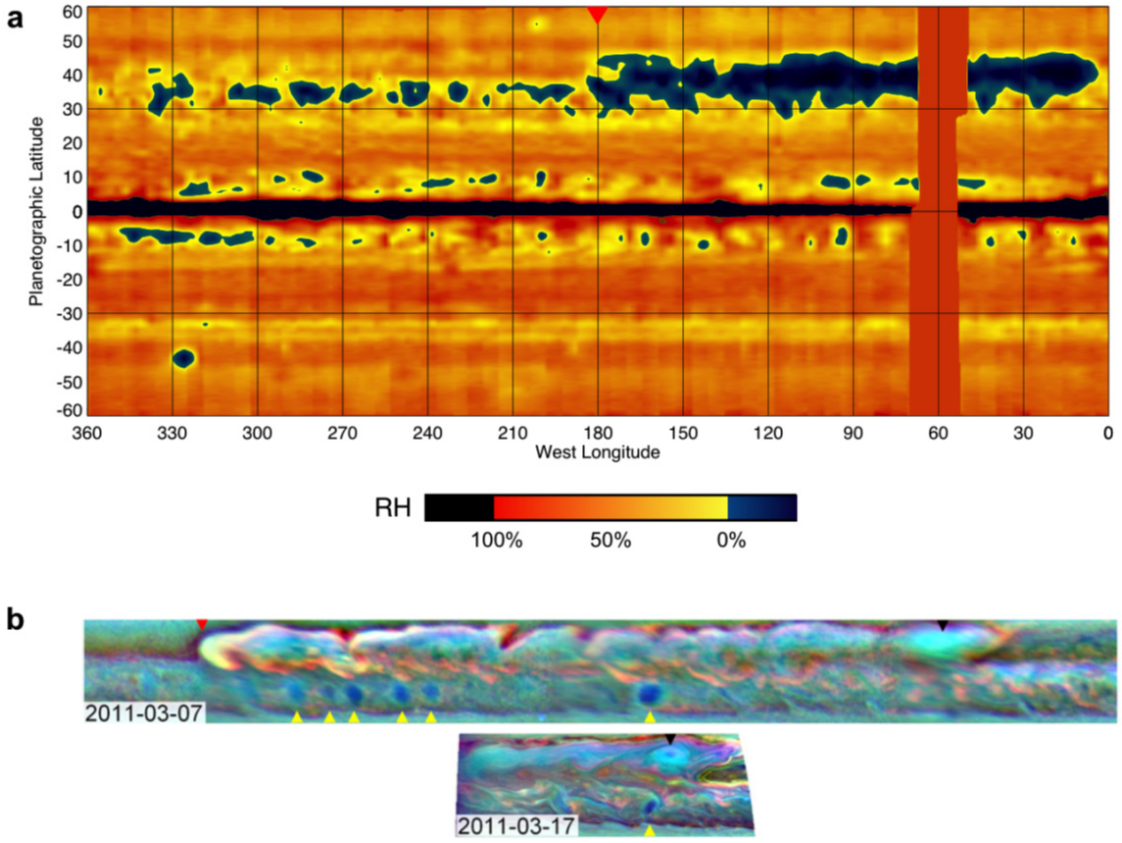

Figure RADAR-23. A simple model used for the ammonia distribution. (a) Map of ammonia cloud humidity from March 20, 2011. Black regions would indicate super saturation of ammonia in the cloud layer (we do not see any). Here, the black regions are due to the cold rings blocking the emission from the atmosphere. Blue regions are regions that require ammonia depletion below the ammonia cloud layer (i.e., RH < 0 in the cloud layer). The northern storm is blue, indicating low ammonia concentrations in the storm that extend to layers beneath the clouds. There are many local regions in the subtropical bands, as well as a storm in the southern hemisphere near 325°W, −43°, that require ammonia depletion below the clouds. (b) Two Cassini ISS images of the northern storm from Sayanagi et al. [2013] Figure 4. These are the closest dates we have to the 2.2 cm map date. Cloud heights are distinguished by the three color filters—red (CB2−750 nm), green (MT2–727 nm), and blue (MT3–889 nm).

A final global map was obtained in 2015, more than four years after the onset of the storm. This map is shown in Figure RADAR-24 in context with maps from 2010 and 2011, all together showing Saturn's atmosphere prior to, in the midst of, and after the storm onset. Figure RADAR-25 shows the relative humidity as described in Figure RADAR-23. This map shows the long-lived ammonia depletion in the latitudes affected by the storm as it has evolved, and contains valuable information on the nature of convection, meridional and zonal circulations in Saturn's sub-cloud atmosphere. A paper discussing the implications for the dynamics of Saturn's atmosphere is in preparation as of this writing.

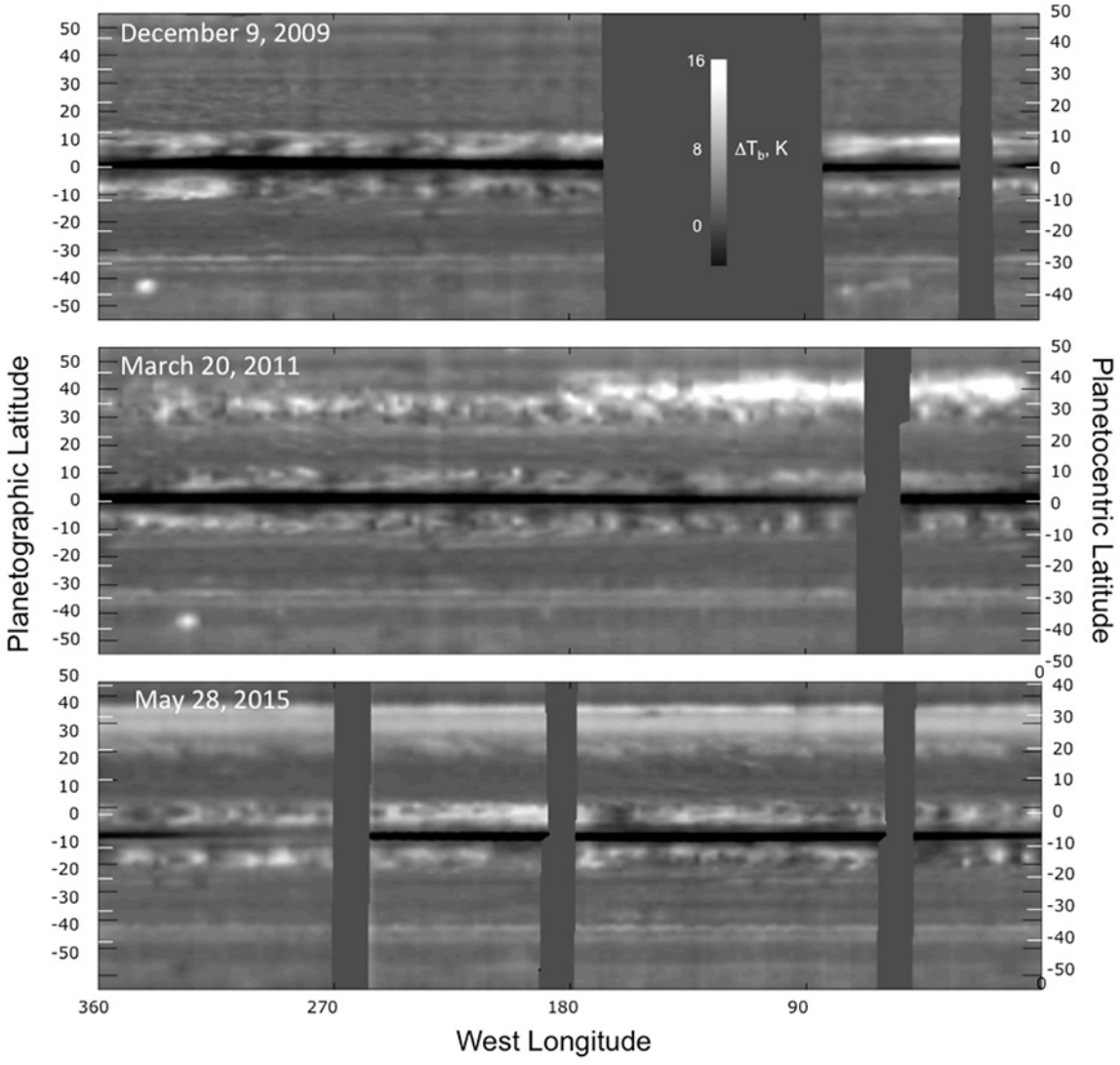

Figure RADAR-24. The global map of 2015 shown in context with earlier maps to show the development of the Great Northern Storm of 2010–2011. The relative brightness for each is shown as in Figure RADAR-21.

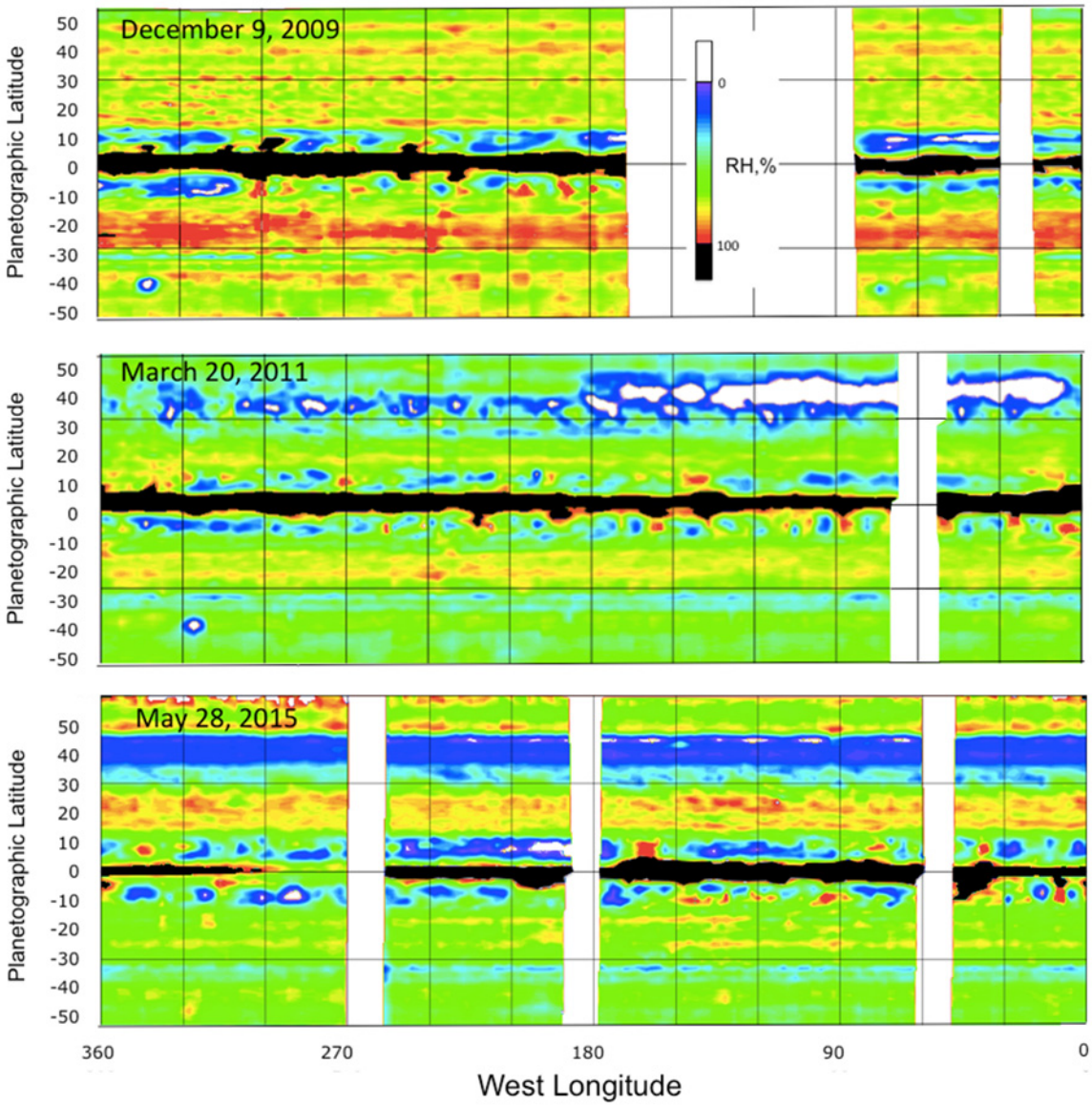

Figure RADAR-25. Ammonia cloud relative humidity for the brightness maps in Figure RADAR-24. Here regions of black are due to ring blockage, while white indicates regions where ammonia additional depletion below the cloud base is required to fit the observations.

Open Questions

The Cassini RADAR radiometer has provided unprecedented images of Saturn's equatorial and mid-latitude atmosphere at 2 cm wavelength. It has uniquely measured the cloud and sub-cloud humidity through the period of the Great Northern Storm of 2010–2011. This provides a basis for ground-based observations of Saturn over multiple frequencies using the VLA and Atacama Large Millimeter/Submillimeter Array (ALMA) radio interferometers to extend the atmospheric depths sounded and follow the slow decay of the 2010–2011 storm, which remains a puzzle. A follow-on

radiometric experiment based on the Juno orbiter's Microwave Radiometer [Janssen et al. 2017; Bolton 2017] would be an excellent complement to an atmospheric sounder assuming that difficulties in obtaining a close orbit and achieving deep sounding in Saturn's more absorbing atmosphere can be overcome. This would enable a comparative examination of the deep atmospheres of both gas giants, which appear to have strikingly different dynamical properties based on present results from Cassini and Juno.

Saturn Ring Science

Introduction

Saturn's rings are the most massive, extensive and diverse ring system in the solar system, …, their origin and age continue to be a subject of debate.

Saturn's rings are the most massive, extensive and diverse ring system in the solar system, yet despite decades of ground and spacecraft-based observations [Dougherty et al. 2009; Grossman 1990; de Pater and Dickel 1991; van der Tak et al. 1999; Dunn et al. 2002, 2005; Poulet et al. 2003; Nicholson et al. 2008], their origin and age continue to be a subject of debate. Although water ice has long been accepted as the most prominent component of ring composition [Cuzzi et al. 1984; Esposito et al. 1984], it is the small fraction of non-icy material that is crucial in understanding their origin and age through source composition and exposure time to extrinsic micrometeoroid bombardment [Cuzzi and Estrada 1998]. However, the abundance and character of this non-icy material remained poorly understood until the extensive observations of Saturn's rings by RADAR, in both its active and passive modes.

Microwave observations at mm- to cm- wavelengths provide an ideal window through which to study the non-icy material fraction in Saturn's main rings, as these are wavelengths where the absorptivity of water ice is negligible compared to that of most non-icy material, and thus the intrinsic thermal radiation from the ring layer is dominated by the non-icy components. Moreover, whereas visible and near-IR spectra are only sensitive to the top millimeter or less of ring particle surfaces, microwave observations are able to sample the bulk of the ring mass. Furthermore, microwave measurements at mm- to cm- wavelengths are most sensitive to mm- and cm- scale particles, which are known to be the most dominant sizes of the ring particles.

Passive radiometry observations at 2.2 cm

During the Cassini Prime Mission, the radiometer scanned Saturn and its rings at 2.2 cm wavelength on 12 occasions between December 2004 and October 2008. There are two categories of radiometric observations of Saturn's rings: low-resolution map scans from a distance of ~20 RS (where RS = 60,330 km is Saturn's radius) and high-resolution spoke scans (not related to the

fuzzy features seen in the B-ring) from a distance of ~5–8 RS. The map scan footprints cover all of the main rings at all azimuthal angles. The projection of the line connecting Saturn's center and the spacecraft onto the ring plane lies at zero degree azimuth, and the azimuthal angle increases anti-clockwise in the ring plane. At small azimuthal angles, the observed ring regions occult Saturn. These observations are comparable to stellar and radio occultations except that the light source is due to the planet's radiation. On the other hand, high-resolution spoke scan footprints only cover the main rings at five distinct intermediate azimuthal angles where the rings are not occulting Saturn. While map scans reveal the complete angular scattering profile, spoke scans show finer radial structures. RADAR has a main beam size of 0.36° in angular diameter (full width at half maximum (FWHM) power), which results in radial resolution of ~2,000 km in high resolution scans and ~6,000 km in low resolution maps.

While this dataset presents several advantages, it is also very challenging to process. Each measurement of antenna temperature is the convolution of the radiometer's broad gain pattern and the brightness temperature of all targets in the field of view [Janssen et al. 2009]. In order to remove the contribution to the signal from the sidelobes and obtain values of the brightness temperature, we developed an iterative adaptation of the successful calibration and sidelobe removal algorithms [Zhang et al. 2017a] developed for Titan and Saturn [Janssen et al. 2009, 2013, 2016]. Figure RADAR-26 shows the output of our calibration and processing applied to a low-resolution map scan of Saturn's rings. Figure RADAR-27 shows the brightness temperature T_b profile versus distance from Saturn center after one high-resolution spoke-scan; all such scans were collected when the rings were not occulting Saturn, at azimuthal angles larger than 20 degrees. Going from the C-ring to B-ring and then to A-ring, the distance from Saturn increases, and hence the planet's angular size decreases as seen from Cassini's vantage point. The dashed curves in Figure RADAR-27 illustrate the decreasing trend of incoming radiation from Saturn as the observation point moves further away from Saturn center. While T_b follows the trend of incoming Saturn radiation in most parts of the rings, the distinct bump (with a peak at ~83,000 km) in the C-ring's brightness is too large to be attributed simply to optical depth variation, which suggests some unusual properties. We will show that this effect may result from a radially variable increase in non-icy material fraction that produces an extra amount of intrinsic thermal emission.

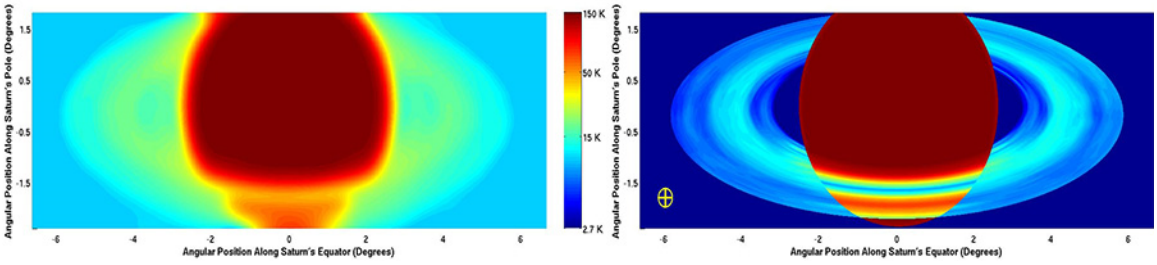

Figure RADAR-26. Calibration of low-resolution Cassini RADAR map scans as projected onto the sky in degrees. Left panel: The collected antenna temperature map. Due to the wide antenna pattern and extensive sidelobe contribution from Saturn, the antenna temperature shows very little clear structure of the main rings. Right panel: The output brightness temperature map obtained through our calibration. The yellow circle in the lower left corner shows the main beam size.

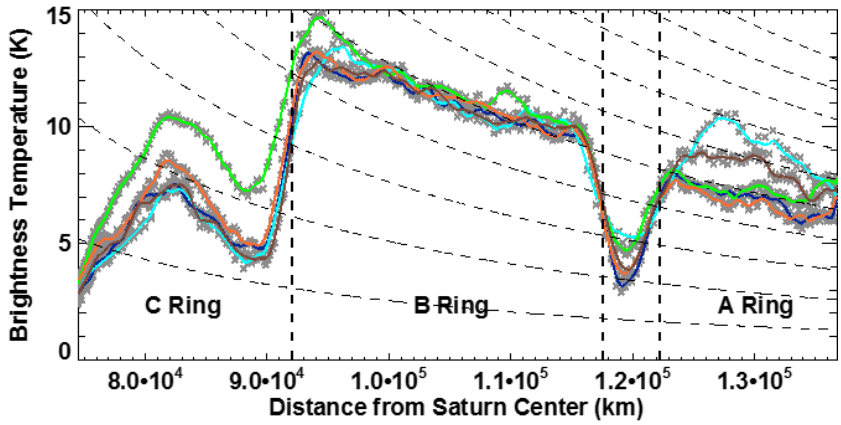

Figure RADAR-27. Brightness temperature T_b versus ring radius obtained from one high-resolution spoke scan. Solid lines of different color indicate spoke scans at different azimuthal angles. The black dashed lines show the trend of incident Saturn radiation, which decreases as one moves further away from Saturn's center.

Brightness temperature model

The observed brightness temperature has four components: 1) directly transmitted Saturn radiation (which exists in occultation data only); 2) scattered Saturn radiation; 3) intrinsic thermal emission; and 4) cosmic microwave background (CMB) contributions. To simulate the observed brightness we use the Monte-Carlo-based photon counting code SimRings [Dunn et al. 2002]. SimRings is able to deal with multiple scattering within the ring layer (where the light source is from extended Saturn emission) and derive the amount of directly transmitted Saturn radiation, scattered Saturn radiation and the intrinsic thermal emission from the ring particles that arrives at the observer. The rings' intrinsic thermal emission mainly depends on the non-icy material fraction since the emissivity of water ice at 2.2 cm is negligible. SimRings requires knowledge of the ring particles' composition and size distribution, which determines the scattering phase function, absorption rate, and the local optical depth.

The ring particle composition is used to determine the material's effective dielectric constant based on the Maxwell-Garnett mixing rule of Effective Medium Theory (EMT)—see Bohren and Huffman [1983]. We assume that the ring particles are made of porous water ice with non-icy material embedded in the form of small inclusions. We primarily use silicates as the candidate for the intermixed non-icy material which has dielectric constant $\varepsilon_{silicate} = 5.38 - i \cdot 0.134$ [Cuzzi et al. 1980].

The ring particles sizes are assumed to have a power law distribution, $n(a) = n_0 a^{-q}$, with minimum size a_{min}, maximum size a_{max}, power law index q and a constant n_0, which depends on the particle areal number density in the rings. Table RADAR-3 summarizes the nominal size distribution parameters we employed for each ring region. The size distribution parameters are determined from previous stellar and solar occultation observations [Zebker et al. 1985; Harbison et al. 2013; Cuzzi et al. 2009; Marouf et al. 2008; French and Nicholson 2000; Dones et al. 1993].

An important result derived from density wave measurements that relate the particle sizes and their mean densities is the opacity, which can be approximated as:

$$\kappa \sim \frac{3(4-q)}{4(3-q)} \cdot \frac{a_{max}^{3-q} - a_{min}^{3-q}}{a_{max}^{4-q} - a_{min}^{4-q}} \cdot \frac{1}{\bar{\rho}}.$$

Table RADAR-3. Particle size distribution parameters in the main rings.

Ring Radius (km)	a_{min}(cm)	a_{max}(m)	q
C-ring: 74,510–92,000	0.4	4.5	3.15
B-ring: 92,000–117,580	30.0	6.3	2.75
Cassini Division: 117,580–122,170	0.1	7.5	2.79
A-ring			
– A0: 122,170–127,900	30.0	5.4	2.75
– A1: 127,900–130,860	30.0	6.3	2.75
– A2: 130,860–133,423	30.0	11.2	2.75

In Saturn's C-ring and Cassini Division, millimeter-centimeter scale particles are dominant in the scattering process and a Mie phase function is a good approximation in these regions. However, in Saturn's B-ring and A-ring, particles are much larger than the wavelength and the particle non-sphericity effect becomes important. The phase function deviates from being simply Mie scattering and become more isotropic. In addition, due to the larger number density found in the middle B-ring and A-ring wakes, close packing of ring particles can also cause the phase function to be more isotropic. To that end, where Mie scattering alone is inadequate, we introduce a phase function that is a linear combination of Mie and isotropic scattering phase functions [Dunn et al. 2002].

$$p(\theta) = (1 - f_{iso}) \cdot p_{mie}(\theta) + f_{iso} \cdot \frac{1}{4\pi}$$

Here f_{iso} is the fraction of isotropic scattering, which is determined by matching the observed data.

The C-ring

Non-Icy Material Fraction Determined by Cassini Radiometry

In the low-resolution maps, the C-ring regions at near-zero azimuthal angles that occult Saturn reveal the forward scattering profile for the C-ring particles. We found that the modeled brightness temperature is much smaller than observed when assuming non-porous ring particles (see Figure RADAR-28). However, we are able to match the observation by either making the whole particle uniformly 75% porous or by assuming a core-mantle ring particle structure with a solid core and porous mantle, both of which result in a more forward-directed scattering phase [Zhang et al. 2017a]. Due to the complication of the core-mantle ring particle structure in our simulation, we defer treatment of the core-mantle particles to the section entitled Ring opacity favors large rocky chunks.

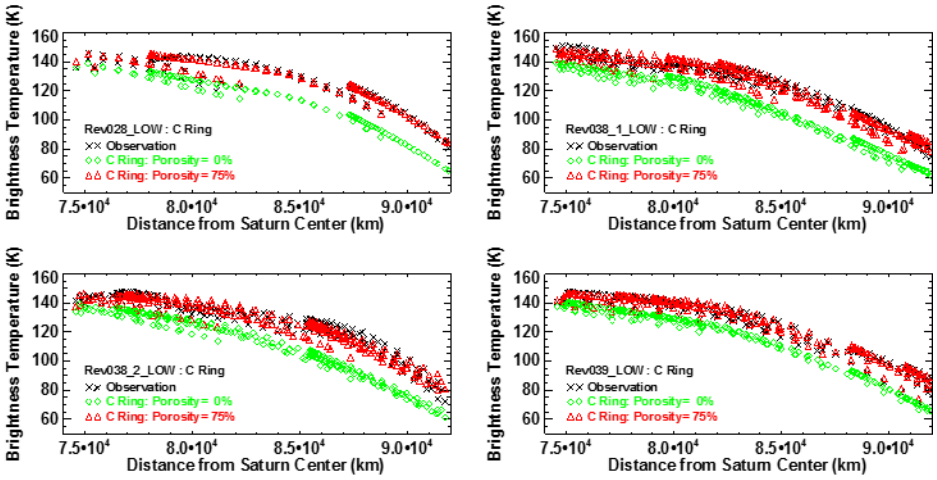

Figure RADAR-28. Brightness temperature model as compared to actual observations for C-ring particles with 75% porosity. Plotted is the brightness temperature versus ring radius for occultation observations of the C-ring low resolution maps during Rev028_LOW (upper left), Rev038_1_LOW (upper right), Rev038_2_LOW (lower left), and Rev039_LOW (lower right). Black crosses: Observed brightness temperature. Green diamonds: Simulated brightness temperature assuming zero porosity. Red triangles: Simulated brightness when assuming C-ring particles are 75% porous.

By adding 75% porosity, the bending angle of intrinsic refraction tends to be smaller and more light gets scattered into the forward direction.

Given that some of the smaller satellites in the Saturn system have bulk porosities in excess of 60% [Thomas et al. 2007; Johnson et al. 2005], and the recent works by the Rosetta team that reported a bulk porosity of 70–80% for comet 67P/Churyumov-Gerasimenko [Sierks et al. 2015; Kofman et al. 2015], it may not be surprising that individual ring particles can be so porous. One possible explanation might be that impact gardening due to micrometeoroid bombardment, which creates a regolith of increasing depth over time—Elliott and Esposito [2011]—may play a role in increasing particle porosity. Collisions among ring particles occur frequently within the C-ring, but at relatively low (mm/s) velocities, when compared to impacts by extrinsic micron-sized meteoroids (~10 times more frequent for the nominal choice of flux, see the section entitled Exposure time due to micrometeoroid bombardment). However, secondary impacts that arise as a result of the ejected material from the primary micrometeoroid impact should occur much more frequently than inter-particle collisions and at velocities of up to tens of meters per second—ballistic transport process as discussed in Cuzzi and Estrada [1998]. These secondary impacts might kick up loosely bound regolith particles such that a considerable exchange of material may happen locally between neighboring ring particles, keeping their regoliths fluffy. Thus, even though inter-particle collisions may have a tendency to compact a ring particle surface, it might be possible that the ring particles can achieve a quasi-equilibrium porous regolith that results from a balance of these combined impact and collisional processes.

While occultation observations mainly reveal the strength of the forward directed part of the scattering phase function, non-occultation observations in high-resolution spoke scans depend more on the scattering phase function at intermediate scattering angles. Figure RADAR-29 shows

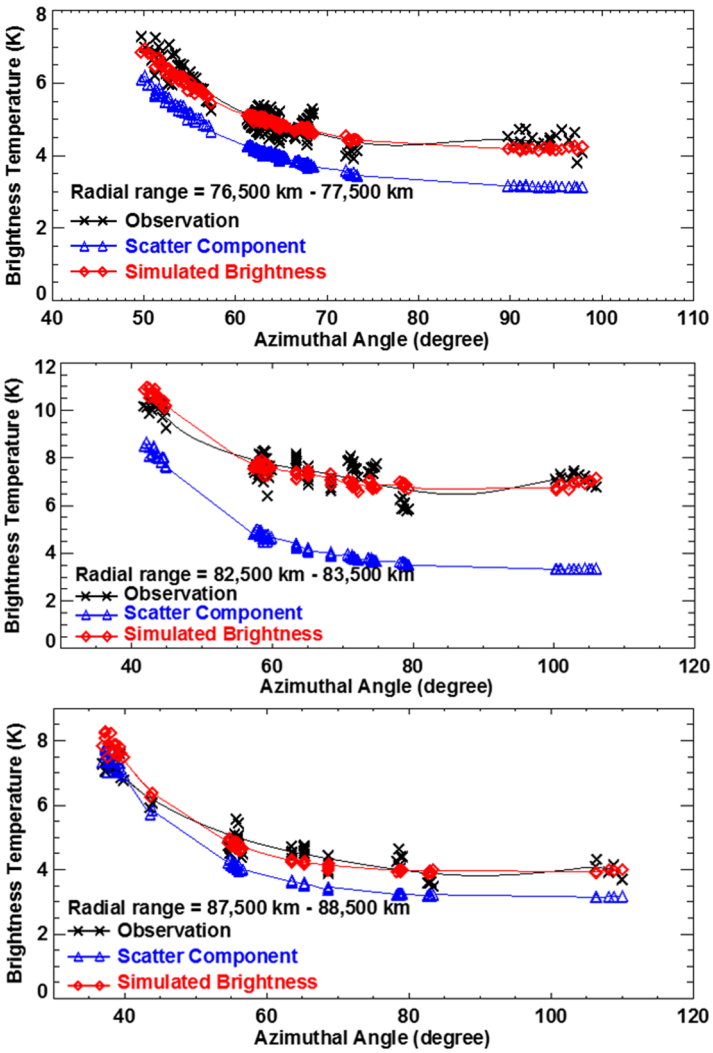

Figure RADAR-29. High-resolution spokes observations and simulations for three ring annuli. Brightness temperature versus azimuthal angle curves at three different ring radii for the: inner (76,500 km–77,500 km); middle (82,500 km–83,500 km); and outer C-ring (87,500 km–88,500 km). All observation data come from high-resolution scan Rev028_HIGH. We plot the observed brightness temperature (black crosses), scattering component with CMB contribution (blue triangles), and simulated brightness temperature (red diamonds—addition of scatter component, CMB contribution and intrinsic thermal emission). We have added ~2%, ~6% and ~1.5% non-icy material in the ring annulus for panels 1, 2 and 3, respectively. The simulated brightness temperature matches the observations well.

high resolution spokes observations and simulations for three ring annuli in the inner, middle and outer C-ring at intermediate azimuthal angles. The simulated scattering profile (brightness temperature versus azimuthal angle) matches the data fairly well with a radially varying non-icy material fraction as shown in Figure RADAR-30. The results of this analysis justify the necessity for including intrinsic thermal emission in order to match the observed brightness temperature, especially around ~83,000 km in the middle C-ring, where the brightness is observed to increase significantly beyond what can be attributed to scattered radiation from Saturn [Zhang et al. 2017a].

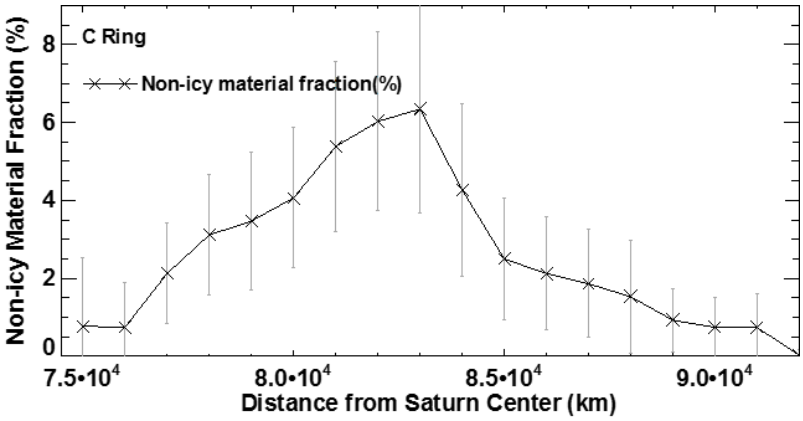

Figure RADAR-30. Simulated scattering profile. The derived radial variation of non-icy fraction reaches its maximum of ~6.3% silicate by volume in the middle of the C-ring and gradually decreases inward, and more sharply outward. The grey vertical lines show the range of one standard deviation.

In the previous paragraphs, we have treated C-ring particles as water ice with a fraction of voids and non-icy material as inclusions. The Maxwell-Garnett mixing rule of the EMT calculates the ring particle's averaged (effective) dielectric constant taking water ice as the host medium. This mixing rule treats one material as the matrix (host material) in which other materials (guest materials) are embedded in the form of small inclusions. However, this model is not symmetric as the host and guest materials do not contribute on an equal basis to the effective dielectric constant. Therefore, it makes a difference what one chooses as the host material. An alternative is to use vacuum as the host medium, which will result in 70% porous C-ring particles and 50% more non-icy material fraction in the C-ring (see Figure RADAR-31). These two cases, using either water ice or vacuum as the host medium, set the upper and lower limit of the non-icy material fraction in the ring particles. The non-icy material fraction will lie in between these two limits depending on which mixing rule is used.

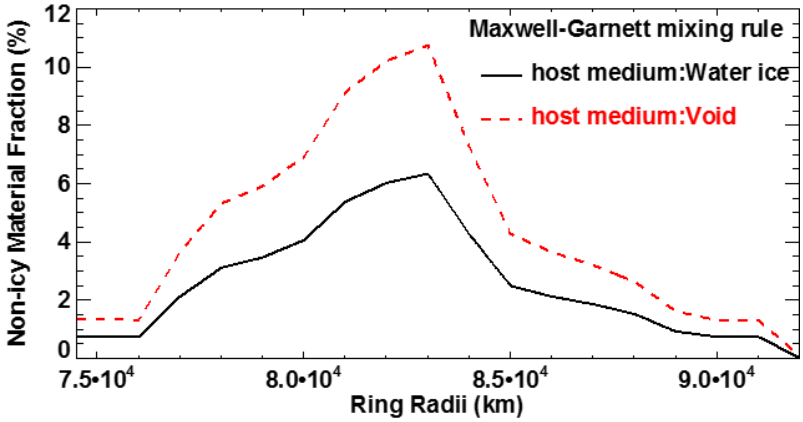

Figure RADAR-31. Using vacuum as an alternative model host medium. Black curve: Maxwell-Garnett mixing rule with water ice as the host material, and 75% porous C-ring particles. Red curve: Maxwell-Garnett mixing rule with vacuum as the host medium, and 70% porous C-ring particles.

EXPOSURE TIME DUE TO MICROMETEOROID BOMBARDMENT

After their formation, the rings have been continuously bombarded by extrinsic meteoroid impacts that have the effect of polluting them with non-icy material over time. The required exposure time to accumulate the observed fraction of non-icy material implies a lower limit on the rings' age. The exposure time scale due to micrometeoroid bombardment is inversely proportional to the local impact flux onto the ring plane.

The radial variability of the derived non-icy material fraction is surprising and warrants discussion. Considering that the local impacting flux depends approximately linearly on the local geometric optical depth in most regions of the C-ring, the final non-icy material fraction should be proportional to opacity, which equals geometric optical depth divided by surface density ($\kappa = \tau_{geometry}/\sigma$). The larger the opacity, the higher the non-icy material fraction should become, if meteoroid bombardment is the only pollution source. Though a complete opacity radial profile for the C-ring is still unknown, the current values at a few radial locations from density wave measurements suggest a higher opacity in the inner (and outer) C-ring of ~0.15 $cm^2\ g^{-1}$, and a significantly lower opacity in the middle C-ring of ~0.022 $cm^2\ g^{-1}$ [Baillie et al. 2011; Hedman and Nicholson 2013], which is the opposite trend to the shape of the non-icy material fraction we have found. In Figure RADAR-32, we demonstrate how the non-icy material fraction would evolve over 15 and 45 million years (upper panel) and 30 and 90 million years (lower panel) after the C-ring first formed assuming that the rings were initially pure water ice, that meteoroid bombardment is the only pollution source and that the C-ring optical depth and surface density have not changed significantly during that time. The opposite trend between the observed (black curve) and simulated (red dashed curve) non-icy material fraction profiles in Figure RADAR-32 implies that if the rings started as mainly pure ice ~15–90 million years ago, there must be some non-icy material source other than the nearly radially constant micrometeoroid flux in order to explain the enhanced non-icy fraction in the middle C-ring [Zhang et al. 2017a].

On the other hand, in order to accumulate the observed peak non-icy material fraction merely from meteoroid bombardment in the middle C-ring, it would require ~900 million years, which sets an upper bound on the age. However, if this is the case, it would imply that the non-icy material fraction in the inner and outer C-ring would be much higher than the observed values and a process that preferentially removes non-icy material from the inner and outer C-ring regions would be required in order to account for the observed distribution. Another alternative is that the C-ring did not start out as nearly pure ice. In such a case, if the non-icy material was intramixed within the initial ring composition, any radial variability that may have existed most likely would have already been smoothed out as a result of ballistic transport [Cuzzi and Estrada 1998; Estrada et al. 2015]. That is, ballistic transport, which behaves much like both a diffusive and advective process [Cuzzi and Estrada 1998] (see next section), generally works to smooth out any compositional differences that may have existed or that might arise in the rings. Indeed, how material is diffused/advected through ballistic transport in the rings is an effective means by which the age of ring features or the rings themselves can be determined. Therefore, the exceptionally high non-icy material fraction in the middle C-ring requires either the recent introduction of a high concentration of non-icy material, or a process that preferentially removes non-icy material from the inner and outer C-ring regions

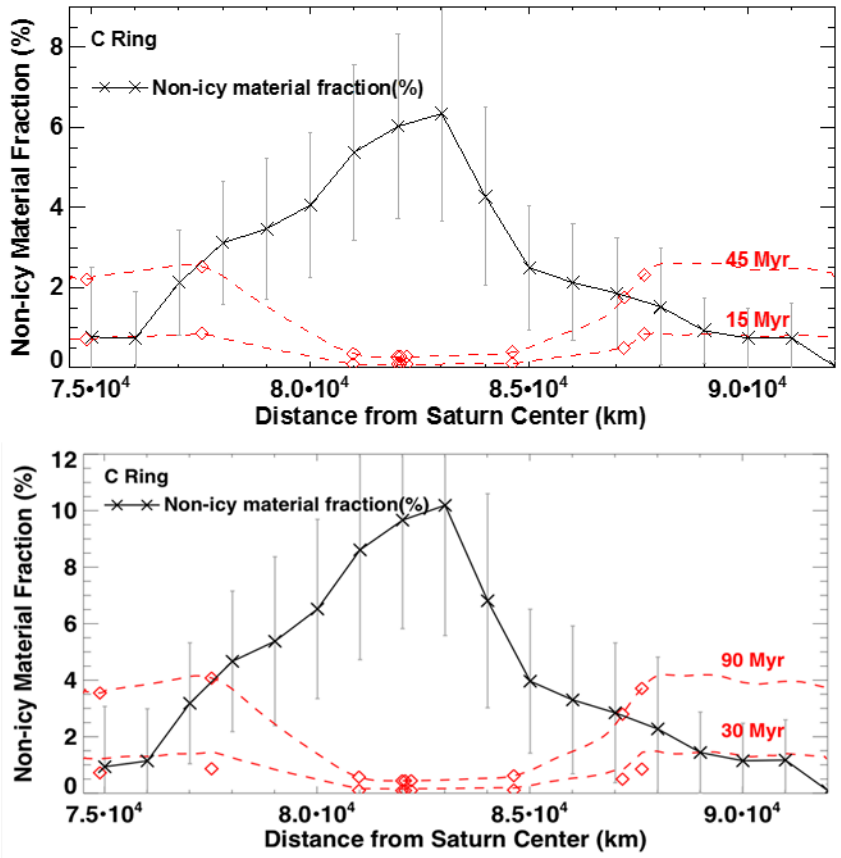

Figure RADAR-32. How the non-icy material fraction would evolve over millions of years. Black curve: Derived non-icy material fraction from the observations. Both cases using Maxwell-Garnett mixing rule with water ice (upper panel) and vacuum (lower panel) as the host material are shown. Red dashed curve: The non-icy material fraction evolution over 15 and 45 million years (upper panel) and 30 and 90 million years (lower panel), if meteoroid bombardment is the only source of contamination. Red diamonds demonstrate the positions where opacity measurements [Baillie et al. 2011; Hedman and Nicholson 2013] have been made through density waves.

[Zhang et al. 2017a]. We argue that the persistence of a non-uniform distribution of silicates within the middle C-ring strongly favors the former scenario. In the next sections, we describe the former scenario in more detail that attempt to address this observation.

A BAND OF NON-ICY MATERIAL FROM AN IMPACTING CENTAUR AT C-RING CENTER

In the first scenario, we assume that meteoroid bombardment has continuously contaminated the whole of the C-ring since it first formed, and that a higher concentration of non-icy material was injected into the middle C-ring at a more recent time. Barring any process that might dilute the non-icy fraction—for example, a by-product of ballistic transport is that icier material spills over from the B-ring to C-ring [Durisen et al. 1992; Estrada et al. 2015]—the implied age of the C-ring from this evolution is between 15 and 90 million years based only on the pollution of the inner and outer

C-ring for the nominal micrometeoroid flux (see Figure RADAR-32). Note that this estimate is inversely proportional to the time-averaged micrometeoroid flux.

Any additional contribution to the effective dielectric constant of material must be attributed to an alternative, more localized source. In order to further examine this source, we investigated a scenario in which the middle C-ring was contaminated by a debris cloud derived from a Centaur disrupted by previous encounters with Saturn [Hedman et al. 2011]. Centaurs captured into orbit around Saturn might break apart into debris through tidal disruption as they pass close to the planet, or even through direct collision with the rings. This debris will follow the same bound trajectory and crash into the rings potentially across a range of radii at later periapses [Hedman et al. 2011]. Assuming the non-icy material is all silicates, and that this material is now finely ground and intramixed within the ring particles, we find that the observed non-icy material distribution may be produced during the break-up of a Centaur with radius R ~7–20 km. The capture of the Centaur would likely involve it passing through the ring plane several times leaving little material behind initially, becoming weaker and rubblized until tides break up the object into smaller fragments which could then be captured and integrated into the rings [Hyodo and Ohtsuki 2014]. In such a scenario, it is not clear that the material would initially be concentrated into a narrow annulus of material. However, in the case that a narrow annulus is the initial condition, the spreading timescale of the high concentration of non-icy material through ballistic transport [Cuzzi and Estrada 1998] could help constrain the earliest possible time the initial contamination occurred. A conservative estimate of the time it would take for the intramixed pollutant that initially occupies an annulus at ~83,000 km to spread into the observed distribution is about 9.3 million years. Therefore the non-uniform radial peak in our intramixed, non-icy material fraction profile would be a relatively new structure, with an age on the order of ~10 million years, though the absolute time scale depends on the meteoroid flux rate at infinity and how gravitationally focused the micrometeoroids are by Saturn. Such Centaur crossing events are fairly likely to occur over this time period. On average, about 5 to 52 Centaurs larger than 7 km in radius may have hit the Saturn system within the last ~10 million years. Once the Centaur is disrupted into debris by Saturn's gravity, the debris is likely to be absorbed by the rings after several orbits. The observational evidence would suggest, however, that successful disruption and capture events of such large Centaurs have not happened so frequently otherwise we might expect to see relatively large peaks in non-icy material concentration in other C-ring regions rather than the single, well-defined peak we observe in the middle C-ring.

RING OPACITY FAVORS LARGE ROCKY CHUNKS

In the previous section, we have discussed the case where non-icy material brought in by the incoming Centaur is intramixed within the ring particles as envisioned in the EMT model. However, it seems unlikely that an incoming Centaur, basically a rocky object that may have substantial internal strength, torn apart gently by tides and ultimately broken into pieces that reside in the C-ring, could be ground to powder this way, especially if it were done fairly recently. It seems more likely that there would still be many chunks of solid silicates in the centimeter-decimeter-meter size range left, which have now been coated by the icy ring material. This would require more total non-icy material in the middle C-ring since non-icy material affects emission most efficiently when

finely divided as in the EMT intramixed assumption versus a salt and pepper, or intramixing type model—Cuzzi and Estrada [1998]; Poulet and Cuzzi [2002]; Cuzzi et al. [2014].

Moreover, 75% porous ring particles containing less than 11% intramixed non-icy material implies a ring layer opacity of ~0.07–0.08 $cm^2\ g^{-1}$ using our nominal particle size distribution, which is inconsistent with the opacity measured through density wave. Recall that the derived radial opacity profile from density wave measurements is notably non-uniform. In order to have a radially varying opacity profile, the C-ring particles must have a radially-varying particle size distribution or a radially varying mean particle density $\bar{\rho}$. At the inner and outer C-ring, the measured opacity is higher than our calculated value, possibly suggesting fewer large particles in those regions. We are able to match the measured opacity by decreasing the maximum particle size from 4.5 m to 1.5 m −2.2 m in the inner C-ring and 1.3 m in the outer C-ring. However, by merely increasing the maximum particle size it is not possible to lower the opacity in the middle C-ring to the measured value ~0.022 $cm^2\ g^{-1}$. Therefore, the exceptionally low opacity in the middle C-ring suggests a potentially considerable amount of extra mass hidden in the ring particles, just where the finely distributed non-icy material also is. A particle in the middle C-ring is likely to contain large chunks of silicates, which originated from the disrupted Centaur.

We proposed a silicate-core and porous-dirty-icy-mantle model in which the mass of the Centaur is initially contained in a narrow annulus located at the peak of the current non-icy material fraction bump in the C-ring center (83,000 km) [Zhang et al. 2017a]. This annulus can viscously spread to the feature's current width (78,000 km–87,000 km) and surface density in as little as ~20–30 million years. It is possible that a combination of viscous spreading and ballistic transport acting together could shorten this time further. We find this variant more compelling because it successfully fulfills the requirements for a strong forward-directed scattering phase function, while explaining both our derived radially-variable thermal emission and the low opacity in the middle C-ring, without requiring the Centaur to be ground to powder.

Other main rings

Though the ring particles in the Cassini Division are very similar to the C-ring particles, and thus a pure Mie scattering phase function matches the observation well, B-ring and A-ring are much optically thicker and comprise particles much larger as compared to the wavelength. We found that a hybrid phase function that varies between Mie half-isotropic to purely isotropic fits the observations best in A-ring and B-ring. By fitting the shape of the scattering profile in the Cassini Division, we found that Cassini Division particles are likely to have 90% porosity, which is consistent with the high opacity ~0.064–0.111 $cm^2\ g^{-1}$ derived from density waves [Colwell et al. 2009]. Though we are not able to determine the porosity values for B-ring and A-ring particles only based on our data, the high opacities measured through density waves [Hedman and Nicholson 2016] suggest that B-ring particles have porosities in excess of 85% while A-ring particles are likely to have porosity value in between 55% and 90%. The radial profile of the derived non-icy material fraction and the corresponding required exposure time to meteoroid flux is rather flat in the B-ring, Cassini Division and A-ring as compared to that in the C-ring, which indicates that the non-icy material observed in these regions has been

accumulated from meteoroid bombardment. In Table RADAR-4, we summarize the derived results (i.e., particle porosity, scattering phase function, silicate fraction, and exposure time) for all the main rings [Zhang et al. 2017b].

Table RADAR-4. Summary of the main finds in C-ring, B-ring, Cassini Division, and A-ring from Cassini passive radiometry observations.

Rings	Radial Range (km)	Porosity	Phase Function	Silicate Fraction	Exposure Time (million years)
C-ring	74,510–92,000	70%–75%	Mie	Baseline: 1–2% Maximum: 6–11%	15–90
B-ring	92,000–117,580	85%–90%	From 50% Mie / 50% Isotropic to Isotropic	Inner/Outer:0.3–0.5% Middle: 0.1–0.2%	30–100
Cassini Division	117,580–122,170	≳90%	Mie	1–2%	60–100
A-ring	122,170–133,423	55%	Isotropic	0.2–0.3%	80–150
Inside Encke Gap		90%	30% Mie / 70% Isotropic		

Conclusion

We conclude that ring particles in the C-ring, B-ring, Cassini Division, and A-ring are likely to be highly porous [Zhang et al. 2017b]. The result that ring particles are very porous across all the main rings may come as some surprise, especially in dense, high particle packing fraction regions like the A-ring and B-ring wakes, since it might be expected that collisions between particles would lead to compaction. Yet relative velocities, and thus impact velocities between ring particles even in these dense regions are small, and is especially true if they are very dissipative—for example, Porco et al. [2008]—making collisions more gentle, and perhaps causing particles to spend more time being stuck in larger clumps—see, for example, Robbins et al. [2010]. Collisions at such low velocities might lead to sticking of ring particles, or only bouncing with some compaction of the particle's surface layers—for example, Güttler et al. [2010]. Meanwhile, micrometeoroid bombardment is continuously acting to garden those same ring particle surfaces, perhaps producing fluffy regoliths, not just from direct bombardment, but even more so from the secondary impacts due to the ballistic transport of the large amounts of impact ejecta. It may be that these competing effects might account for and/or maintain particle porosity.

The C-ring non-icy material fraction shows the most significant and interesting radial variation, reaching a maximum of 6%–11% by volume in the center of the C-ring near 83,000 km, and decreasing gradually to 1%–2% inward and rapidly outward from this radial location [Zhang et al. 2017a]. A possible scenario that nicely explains this trend has a passing Centaur providing the necessary material for post-formation enhancement of the C-ring non-icy material in addition to the micrometeoroid in-fall component. That is to say, the non-icy material fraction in the inner and outer C-ring, which is about 1%–2%, is due to meteoroid bombardment and indicates an exposure time of 15–90 million years. On the contrary, the non-icy material fraction radial profile in the B-ring, A-ring and Cassini Division are relatively flat and can be explained by merely meteoroid bombardment pollution.

Our derived results for the radial distribution of the mass fraction of non-icy material due to direct micrometeoroid bombardment in general support the idea that Saturn's rings are geologically young, formed ≲150 million years ago. The high contamination rate in the middle C-ring, which we have explained as being due to the breakup and deposition of a Centaur, occurs within this time frame [Zhang et al. 2017a]. It further suggests a formation scenario in which the rings are derived from the relatively recent breakup of an icy moon, perhaps of Mimas' mass consistent with the post Voyager ring mass estimate [Esposito 1984], though recently Hedman and Nicholson [2016] suggest that the total mass of the rings may be as little as 0.4 times Mimas' mass. However, no model for the origin of the rings in which they form within the indicated timescale has thus far been proposed. It might be argued that such a ring progenitor may have had a rocky core that could still in one form or another remain hidden within the rings [Charnoz et al. 2009b] which might then account for the anomalous fraction in the C-ring. However, how that rocky material ends up solely in the C-ring but apparently not elsewhere, combined with the fact that the radial distribution of non-icy material and observed opacity in the middle C-ring can be simulated through viscous diffusion of an initially high density annulus of rocky chunks embedded within icy mantles (core-mantle model) suggests that the Centaur capture scenario can readily account for the observations.

Active radar observation during Cassini's Grand Finale

During the Grand Finale, RADAR scanned along the line connecting the ring plane crossing point with Saturn's center in the active mode. These observations looked at the rings' backscattering as a function of radial distance. Although similar observations have been done at optical wavelengths, RADAR saw a different population of ring particles because our measurements will be dominated by cm-scale and larger particles, while the optical observations are seeing a wider spectrum of particle sizes. Figure RADAR-33 shows calibrated normalized backscattering cross-section in F-ring orbit Rev 260 and Proximal orbit Rev 282. These data have not gone through the range compression process and the resolution is therefore equal to the aperture resolution with angular diameter of 0.36°, which is about hundreds of kilometer as projected onto the ring plane. After the

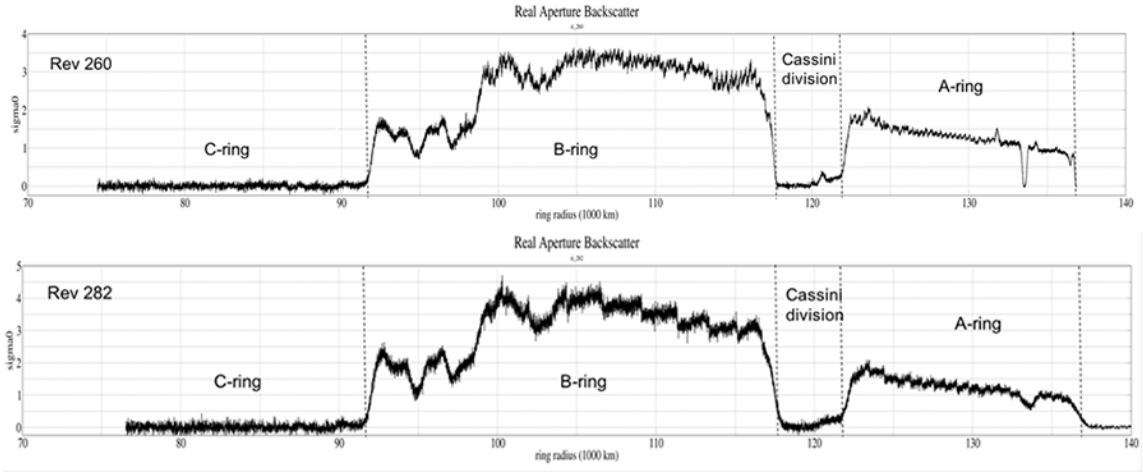

Figure RADAR-33. Normalized back scattering cross-section obtained in Rev 260 and Rev 282.

range compression we would expect the radial resolution to be as high as several kilometers. The Rev 260 observation was shortly after the ring plane crossing and thus has a shorter observation range and thus higher resolution.

In order to compare the observation with the known ring structure, we plot the rings optical depth with the red curve over the Rev 260 data (see Figure RADAR-34). We notice that the backscattering signal in the C-ring and inner Cassini Division is below the noise level, which is consistent with the previous Arecibo observation, which is due to the low optical depth, smaller particle size, and relatively larger absorption loss there. However, we do see backscattering from the outer Cassini Division, suggesting that the ring particles at the outer Cassini Division are more similar to those in the inner A-ring. These particles might have been spilled from the inner A-ring through ballistic transportation. We also notice that the backscattering in the A-ring interior Encke Gap (located at 133,590 km) is much higher than that exterior Encke Gap, suggesting that particles in the exterior Encke Gap tend to be smaller than those in the interior Encke Gap. The observed backscattering in B-ring and A-ring

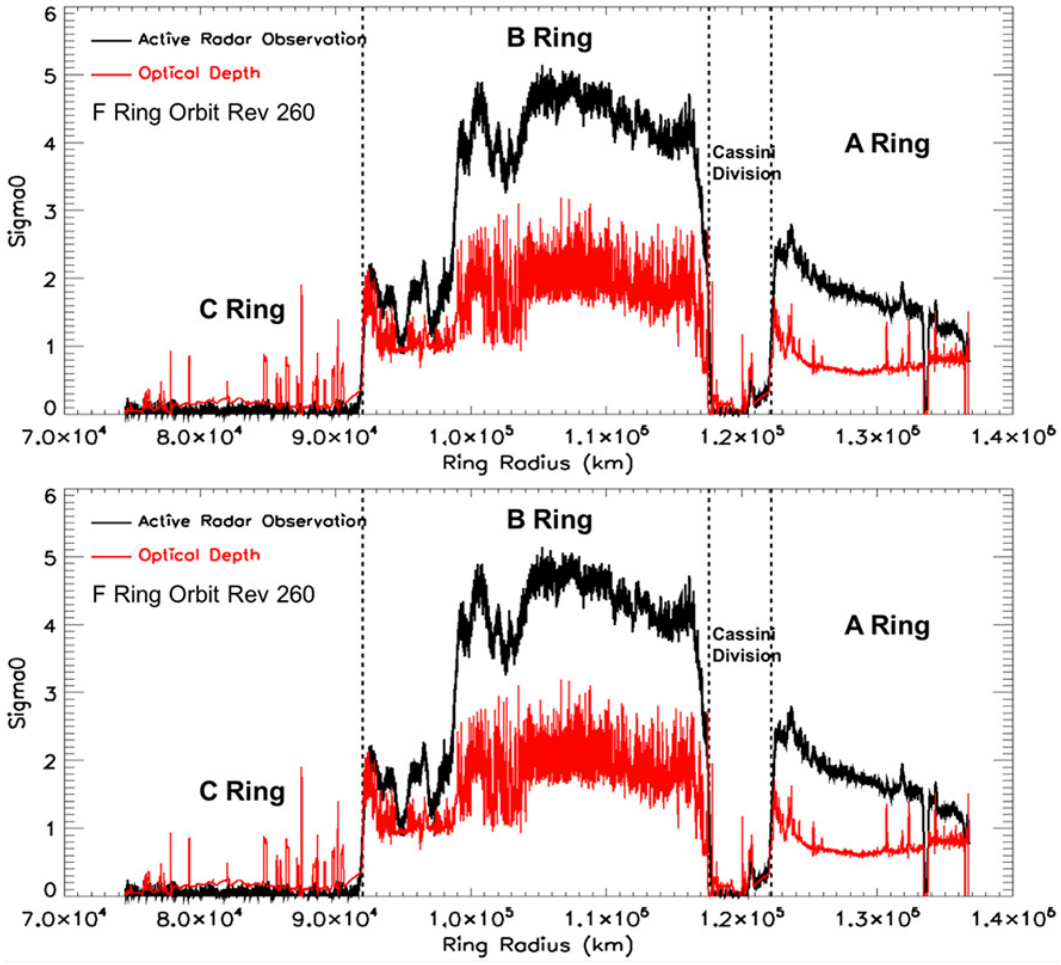

Figure RADAR-34. Comparison between the Rev 260 normalized backscattering cross-section (black curve) and rings optical depth (red curve). In the lower panel, we further zoom in and focus on the A-ring. For better comparison, we have rescaled the optical depth in the lower panel.

is lower than as predicted by a pure Mie scattering phase function. An accurate backscattering phase function is required in order to match the simulation with the observation, which will then help determining the non-spherical shape of the A-ring and B-ring particles. In the lower panel, we further zoom in and focus on the A-ring and Cassini Division. Despite the difficulty in calibrating these observations, we have successfully had the observation line up with the known fine structures. We are able to resolve the Encke Gap, which is about 300 km wide. Furthermore, we have captured all the density and bending waves structures, which are the dynamical structures we are interested in. There is still a great deal to be done, but we must acknowledge that these results of the Cassini era will stand firmly as the benchmark until that point in a possibly uncertain future that we may return to observe Saturn and its majestic rings up close once again.

Icy Satellite Science

Introduction

While it was initially designed to examine the surface of Titan through the veil of its optically opaque atmosphere, RADAR was occasionally used to observe Saturn's airless icy moons from long ranges (>50,000 km) and, less frequently, during targeted flybys. In this section, we give an overview of the Cassini radar/radiometry observations of Mimas, Enceladus, Tethys, Dione, Rhea, Hyperion, Iapetus, and Phoebe, many of which have not been published as of this writing. These observations have taught us much about the about the near-surface of the middle-sized satellites of Saturn, but many questions remain about their composition, structure and what it tells us about their geological history and interaction with Saturn and its rings.

Science objectives

Investigating the microwave properties … provides insights into the various physical and geological processes … and thus into what is common and what is specific to the history of each satellite.

After Titan, the six largest Saturnian satellites are, in order of distance from Saturn: Mimas, Enceladus, Tethys, Dione, Rhea, and Iapetus (Figure RADAR-35). Phoebe and Hyperion are smaller and exhibit irregular shapes. The collective formation of these moons and subsequent evolution remains an outstanding problem. All of them are composed largely of water ice [Clark et al. 1986]. However, their respective evolution history and near environment have led to different regolith composition and structure. In particular, they show evidence of varying degrees of geologic activity in the past and, in the case of Enceladus, the present [Porco et al. 2006]. Investigating the microwave properties of Saturn's airless satellites' near-surface provides insights into the various physical and geological processes that have affected them and thus into what is common and what is specific to the history of each satellite.

Figure RADAR-35. Saturnian icy airless satellites observed by the Cassini RADAR (with the exception of Hyperion). They are here presented at scale (in size, not in distance) and by order of distance from Saturn.

Microwave observations of Saturnian satellites are rare and recent. Until the 2004 through 2007 oppositions of the Saturn system, Earth-based radar measurements in the outer system were limited to Galilean satellites and Titan [Muhleman et al. 1990; Campbell et al. 2003; Roe et al. 2004]. Black et al. [2004, 2007] observed both hemispheres of Iapetus and the middle-sized Saturnian satellites Rhea, Dione, Tethys, and Enceladus with the Arecibo Observatory's 13 cm wavelength (2.38 GHz) radar system. The other Earth-based planetary radar system, Goldstone—equipped with a 3.5 cm transmitter (X-band)—has not been used to observe these objects or other Saturnian airless satellites yet. In addition, passive microwave observations of Saturnian moons from Earth are difficult to make due to confusion with emissions from the planet, the faintness of some targets and their small apparent size. That is the reason why, with the exception of Titan and Iapetus, they have never been conducted. In that regard, the Cassini RADAR and radiometry observations of Saturn's icy moons are pioneer.

RADAR operates at a wavelength (2.2 cm, f = 13.78 GHz), which is a factor of 6 times smaller than the 12.6 cm wavelength used by Arecibo, and 22 times longer than the millimeter wavelengths at the limit of Cassini's CIRS instrument. It has thus expanded the observation of the icy satellites of Saturn to a new and revealing length scale. The Cassini RADAR likely probes icy subsurfaces down to depths of several meters against few millimeters for CIRS. Its main scientific objective was to provide constraints on the thermal, physical and compositional properties of the first few meters below the surface of the investigated objects and, doing so, insights into the degree of purity and maturity of their water-ice regolith. The goal was also to further explore existing hemispheric dichotomies or regional anomalies such as the dramatic two-tone coloration of Iapetus. In addition, operations at closer ranges (i.e., spatially resolved) offered a unique opportunity to examine or detect features of interest at the surface and identify potential hot spots in the near-surface, in particular of Enceladus. Overall, RADAR observations of Saturn's icy moons were to enhance our understanding of the diversity of icy regoliths in the solar system by comparison with radio observations of other objects such as the Galilean satellites (e.g., de Pater et al. [1984], Muhleman and Berge [1991], and Black et al. [2001]), trans-Neptunian objects (e.g., Lellouch et al. 2017], or comets (e.g., Gulkis et al. [2015]).

Data acquisition, calibration, and reduction

Most of the Cassini icy satellite observations are distinguished by the relatively long range to the target. Notable exceptions are one close flyby of Iapetus that is partially analyzed in Le Gall et al.

[2014], two close flybys of Enceladus where one is partially analyzed in Ries and Janssen [2015] and Le Gall et al. [2017], one close flyby of Dione (not yet analyzed), and one close flyby of Rhea that is partially analyzed in Wye [2011] during which spatially resolved data were acquired in both the active (scatterometry) and passive (radiometry) modes of the instrument.

Background

RADAR data come in two flavors: active and passive. In its active mode, the instrument measures the radar albedo which describes the reflectivity of a target. The radar cross-section (RCS) of a target is the projected area of a perfectly reflective, isotropic target that would return an identical echo power to what is measured, if it was observed at the same distance from the radar and with the same transmitted and received polarizations. The radar albedo is derived by normalizing the radar cross-section by the projected geometric area of the target or equivalently by the RCS of a perfectly reflective target such as a smooth metallic sphere. It is thus a dimensionless quantity which is a measure of how reflective the target is in the backscatter direction. RADAR receives echoes in the same linear polarization as it transmits, so it provides same-linear radar albedos at 2.2 cm. For more details, see Ostro et al. [2006] and Wye [2011].

In its passive mode, RADAR records the microwave thermal emission from the near-surface through the measurements of its brightness temperature essentially at the same wavelength (2.2 cm) and with the same aperture as in active mode. By virtue of the Rayleigh-Jeans approximation, the 2.2 cm emissivity of the surface can be estimated from the measured brightness temperature dividing it by the effective physical temperature of the near-surface.

In best cases, active and passive distant observations follow each other so that the same (or almost the same) disk is observed in both modes and thus the derived disk-integrated radar albedo and brightness temperature can be compared, which is key for understanding the near-surface properties. When active and passive measurements are too separated in time, the sub-spacecraft point has changed between observations (both due to the motion of the spacecraft and the rotation of the satellite) and it is not relevant to compare active and passive measurements, especially for satellites that exhibit a hemispheric dichotomy.

Lastly, we note that there were two Hyperion observations, HY15 and HY39. However, these data are not included in this report because their reduction, which requires a shape model is still a work in progress.

Distant observations

Typical distant RADAR observations of Saturn's moons occur at ranges between 50,000 km and 500,000 km where the antenna beamwidth is comparable to or greater than the apparent angular extent of the target's disk. These experiments were designed largely for disk-integrated albedo and average temperature calculation. The derivation of these quantities is described in the next paragraph. Ostro et al. [2006, 2010] report on the distant observations of Saturn's major airless

satellites measured at the beginning of the mission. Since then, the observational database has significantly increased.

DISTANT ACTIVE STARES

During distant active observations, often referred to as stares, RADAR transmits 46 W through the 4 meter dish antenna with a half-power beamwidth of 0.37°. The receiver operates with a relatively high noise temperature around 900 K, and the received echo power is well below the noise floor. To overcome the low signal strength, the radar stares at the target body while accumulating echo measurements (see Figure RADAR-36 left). Spacecraft power constraints limit RADAR to a 7% transmit duty cycle, so the actual integration time is less than the total staring time, which usually runs 5 to 10 minutes for a single observation. In order to maximize the signal to noise ratio (SNR), the echo data is Fourier-transformed and then summed in the frequency domain. The transmit events consist of bursts of single frequency pulses at 13.78 GHz. The received echo power is spread out in the frequency domain by Doppler variation, which arises from the relative motion of the spacecraft and the rotation of the target body (see Figure RADAR-36 right). For the icy satellites, the Doppler variation ranges from a few hundred Hz up to about 4 kHz. The pulsed nature of the transmit events introduces grating lobes spaced at the pulse repetition frequency (PRF). The PRF is set to a frequency higher than the Doppler spread of the target, so the central spectral peak is separated from the grating lobes and shows the natural variation of the echo power over the target body.

The sum of the echo power in the power spectrum is then scaled by the radar equation to give a radar albedo for the target body. More especially, the radar equation is applied assuming azimuthal homogeneity and a diffuse surface scattering function given by $\sigma^0 = Acos^n\theta$ where θ is the incidence angle. The values of A and n are obtained from a least-squares fit to the observed power spectrum with a model consisting of the surface scattering function and the antenna gain pattern integrated over the illuminated area (see Figure RADAR-36). The resulting disk-integrated radar albedo is the uniform normalized backscattering value, which reproduces the observed integrated power assuming that the fit model is correct. Therefore, it is derived from the best-fit values of A and n as follows:

$$A_{\mathrm{SL}-2}^{\mathrm{disk}} = \frac{2\pi R_t^2 \int_0^{\frac{\pi}{2}} \sigma^0(\theta) \sin\theta d\theta}{\pi R_t^2} = 2\int_0^{\frac{\pi}{2}} Acos^n\theta \sin\theta \, d\theta. \qquad \text{Eq. 1}$$

It results:

$$A_{\mathrm{SL}-2}^{\mathrm{disk}} = \frac{2A}{n+1}. \qquad \text{Eq. 2}$$

For more details, see Ostro et al. [2006] and Wye [2011].

Table RADAR-5 presents the results of 79 active stares. These results are discussed in the next section (see also Figure RADAR-41). Note that it corrects a factor of 2 error in the originally published values in Ostro et al. [2006, 2010]. The original calculation was normalized by the total surface area of the visible hemisphere (i.e., $2\pi R_t^2$); but to be consistent with Earth-based

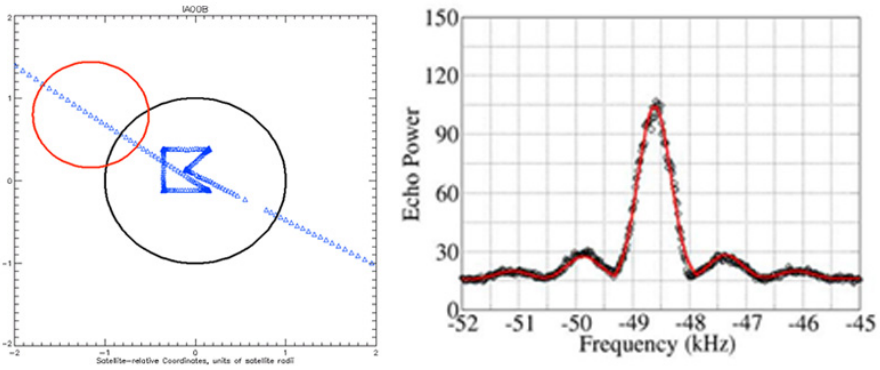

Figure RADAR-36. Distant active RADAR observations. Left: Boresight pointing directions (blue triangles) during the IA-B active stare observation. Iapetus' disk is in black. The beam size at the beginning of the observation is indicated in red. Right: Cassini 2.2-cm radar echo power spectrum (black circle symbols) acquired during the IA-B stare observation and model fit (red line). Figures extracted from Ostro et al. [2006].

observations and the usual convention for the definition of radar albedo, the correct normalization is the disk cross-sectional area (i.e., πR_t^2). This gives an albedo of 1 for a conducting sphere.

The last column of Table RADAR-5 shows the relative errors on the derived disk-integrated albedos. These describe the statistical uncertainties and were derived from the goodness of the fit. The absolute error is about 1.5 dB (1.4 in linear scale). It was estimated adding all known uncertainties on the transmitter power, receiver path losses, receiver gain, and beam solid angle.

We highlight that the choice of a surface scattering function as just a diffuse cosine law is supported by the shape of the measured spectra. As stated in Ostro et al. [2006], none of them, and none of the ground-based echo spectra from any of our targets or the icy Galilean satellites, show any hint of the specular (narrowband) scattering expected if the echoes were dominated by single backreflections from surface elements that are large and smooth at scales near the wavelength. Rather, the spectral shapes are broad, indicating diffuse scattering from structural complexity at some scale(s) comparable to the wavelength or larger.

We further note that radiometry data were also acquired during active stares. However, because the transmitter has just been turned ON at the beginning of the observation and/or because it is turned OFF and ON at least once during these observations, the receiver temperature is not stabilized and the calibration of the radiometry data is not straightforward.

Table RADAR-5. Cassini active-stare observations of Mimas (MI), Tethys (TE), Enceladus (EN), Dione (DI), Rhea (RH), Iapetus (IA), and Phoebe (PH).

Obs ID[a]	Latitude (°)	W Longitude (°)	Beam size (diameter)	Range (km)	n	A_{SL-2}^{disk}	Error
MI47	−2.2	59.3	3.56	219,539	1.9	**2.45**	0.022
MI53	16.2	136.4	2.89	177,750	1.9	**2.69**	0.005
MI64	−48.3	150.7	1.78	109,554	1.9	**2.37**	0.005
MI126	−5.0	271.8	0.68	42,047	1.3	**2.69**	0.005

Table RADAR-5. Cassini active-stare observations of Mimas (MI), Tethys (TE), Enceladus (EN), Dione (DI), Rhea (RH), Iapetus (IA), and Phoebe (PH).

Obs ID[a]	Latitude (°)	W Longitude (°)	Beam size (diameter)	Range (km)	n	A_{SL-2}^{disk}	Error
EN3	0.0	232.0	2.14	165,480	2.0	**2.16**	0.004
EN4	−12.8	70.1	1.08	83,059	1.8	**2.82**	0.002
EN28	60.7	186.5	2.11	162,678	1.2	**3.01**	0.005
EN32	−29.2	243.0	1.18	90,772	1.7	**3.15**	0.002
EN50	16.7	120.0	1.54	119,321	1.9	**3.21**	0.004
EN61In	68.9	108.6	1.88	145,225	1.7	**3.49**	0.004
EN120	−0.5	313.5	0.97	75,735	1.8	**2.63**	0.005
EN61Out	−70.3	331.9	1.09	83,845	1.7	**3.04**	0.005
TE15	−0.2	207.3	0.74	120,908	1.8	**2.76**	0.002
TE21	3.2	254.6	1.47	240,696	1.7	**2.66**	0.004
TE48	1.9	107.7	0.58	95,421	2.1	**3.10**	0.003
DI16	−1.3	14.9	0.64	111,107	1.5	**1.64**	0.005
DI16C1	19.2	18.0	0.66	115,330	1.9	**1.70**	0.005
DI16C2	−3.5	36.2	0.69	119,692	2.9	**1.40**	0.005
DI16C3	0.9	358.4	0.72	124,780	1.3	**2.18**	0.005
DI16C4	−19.1	14.9	0.75	129,270	1.4	**1.56**	0.004
DI27	−33.6	266.8	0.98	169,413	1.9	**1.94**	0.003
DI33**	17.1	355.7	0.44	76,199	2.4	**1.31**	0.004
DI33C1	43.1	27.4	0.45	77,546	1.8	**1.93**	0.005
DI33C2	8.3	26.2	0.45	78,600	2.1	**1.35**	0.005
DI33C3	−10.5	353.3	0.46	79,847	4.8	**1.25**	0.005
DI33C4	15.0	321.3	0.47	81,148	1.1	**1.36**	0.005
DI50	−12.6	227.0	0.46	79,275	2.3	**1.58**	0.003
DI50C1	−11.3	242.9	0.57	98,379	2.8	**1.46**	0.005
DI50C2	−42.7	215.9	0.54	93,688	1.4	**1.88**	0.004
DI50C3	−10.8	187.4	0.51	89,125	1.8	**1.85**	0.004
DI50C4	19.7	222.7	0.49	84,676	1.9	**1.66**	0.004
RH11	−74.4	61.7	0.82	193,603	1.7	**1.84**	0.003
RH18*	0.4	17.5	0.51	120,829	1.9	**1.83**	0.005
RH18C1	27.6	17.6	0.53	125,575	1.9	**1.81**	0.003
RH18C2	0.3	44.0	0.57	135,169	2.7	**1.32**	0.004
RH18C3	−23.5	20.1	0.61	144,896	1.4	**1.89**	0.004
RH18C4	−0.0	0.2	0.65	154,761	1.3	**2.36**	0.004
RH22	0.9	109.1	0.40	93,867	5.2	**1.09**	0.002
RH22C1	−35.2	102.7	0.40	95,353	1.0	**2.39**	0.003
RH22C2*	−2.9	76.0	0.41	96,415	1.1	**2.18**	0.003

Table RADAR-5. Cassini active-stare observations of Mimas (MI), Tethys (TE), Enceladus (EN), Dione (DI), Rhea (RH), Iapetus (IA), and Phoebe (PH).

Obs ID[a]	Latitude (°)	W Longitude (°)	Beam size (diameter)	Range (km)	n	A_{SL-2}^{disk}	Error
RH22C3	35.8	100.0	0.41	97,476	1.5	**1.60**	0.003
RH22C4	23.2	145.4	0.42	98,647	3.0	**1.22**	0.004
RH22C5	−16.1	149.9	0.42	99,771	3.1	**1.36**	0.004
RH27	26.7	320.2	0.77	181,621	1.6	**2.18**	0.003
RH45	−45.0	63.2	0.83	195,637	1.5	**2.12**	0.003
RH47	−2.7	234.2	0.64	152,183	1.2	**2.62**	0.002
RH49	−0.4	346.8	0.45	105,925	2.1	**1.86**	0.005
RH49C1	−35.1	347.4	0.44	103,287	1.0	**2.34**	0.006
RH49C2	−1.8	315.8	0.43	100,710	1.8	**1.97**	0.007
RH49C3	27.9	322.4	0.41	98,206	1.6	**1.89**	0.006
RH49C4	28.6	9.2	0.40	95,652	1.3	**2.04**	0.006
RH127	0.8	163.5	0.27	63,927	2.7	**1.43**	0.007
RH49C5	−9.0	24.8	0.39	93,559	1.0	**2.38**	0.006
IAIn	38.8	66.5	0.68	150,823	1.1	**0.54**	0.009
IAInC1	52.0	41.6	0.68	150,229	2.3	**0.54**	0.008
IAInC2	52.0	91.6	0.67	149,611	1.9	**0.42**	0.009
IAInC3	23.1	82.2	0.67	148,993	1.2	**0.41**	0.011
IAInC4	23.8	49.2	0.67	148,375	0.7	**0.56**	0.011
IAOut	45.6	296.0	0.91	202,360	1.3	**1.02**	0.006
IA17	37.1	358.3	1.88	419,001	3.1	**0.71**	0.020
IA49Obs1	10.9	61.2	1.10	244,226	1.5	**0.34**	0.019
IA49Obs2	10.4	65.5	0.45	100,193	1.9	**0.28**	0.011
IA49Obs2C1	−15.4	72.6	0.49	109,270	1.4	**0.34**	0.017
IA49Obs2C2	3.0	39.8	0.48	107,855	0.4	**0.43**	0.016
IA49Obs2C3	35.6	57.2	0.48	106,450	1.1	**0.39**	0.016
IA49Obs2C4	16.7	91.3	0.47	105,049	1.3	**0.36**	0.016
IA49Obs4	−10.3	247.3	0.50	110,290	2.2	**0.66**	0.018
IA49Obs4C1	−16.6	274.9	0.50	111,345	1.5	**0.92**	0.018
IA49Obs4C2	−36.6	238.3	0.50	112,121	1.8	**0.66**	0.019
IA49Obs4C3	−1.6	220.5	0.51	112,763	2.1	**0.48**	0.019
IA49Obs4C4*	16.3	255.0	0.51	113,460	1.8	**0.82**	0.019
PHIn	−21.9	245.5	2.72	92,525	1.1	**0.29**	0.044
PHOut	26.7	327.8	1.71	58,238	1.3	**0.31**	0.007

[a] Observations for which there is a discrepancy in the best-fit n and derived radar albedo compared to what was published in Ostro et al. [2010] are marked by a * when the discrepancy is small and by ** when the discrepancy is significant.

DISTANT PASSIVE RASTER SCANS

Distant radiometry observations use the spacecraft reaction wheels to raster-scan a rectangular area centered on the target and extending off the disk for baseline calibration (see Figure RADAR-37). The rasters are approximately 2° in length with spacing less than half of the 0.37° beamwidth. First, the measured antenna temperatures are calibrated using the best current calibration of the instrument. This calibration is based on Titan and Saturn observations and described in Janssen et al. [2016], where it is argued that the resulting absolute uncertainty on non-Titan objects is better than 2%. The cold sky reference level (i.e., the Cosmic Microwave Background brightness temperature at 2.7 K) is determined by averaging the off-disk observations. Second, a limb-darkening brightness temperature model (see Figure RADAR-37 bottom) is used to derive the total emission from the moon, expressed as its disk-averaged brightness temperature $T_{\mathrm{b}}^{\mathrm{disk}}$. This model is convolved with the well-determined beam pattern of the radiometer along the raster-scan path in order to produce synthetic data with the same viewing geometry as the time-ordered measured data (see Figure RADAR-37). The model parameters, namely the pointing error,

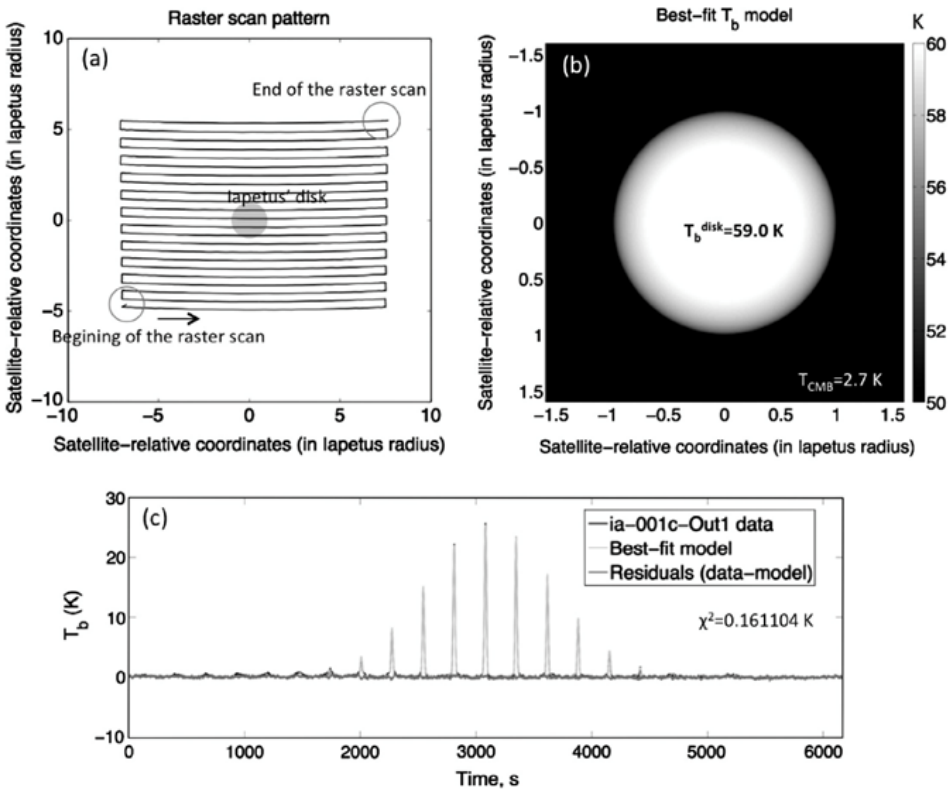

Figure RADAR-37. IA01c-1-Out1 distant radiometry observation of Iapetus. Top Left: Raster-scan pattern performed to collect radiometry data. The beam sizes at the beginning and the end of the raster scan are indicated; they are about the size of Iapetus' diameter (see also Table RADAR-6). Top Right: Measured calibrated antenna temperature compared to the best-fit model as a function of time. Radiometry distant raster-scan typically last one or two hours. Bottom: Best-fit model and corresponding disk-averaged temperature. The model assumes a circularly symmetric bright disk (730 km in diameter) with a $\cos^n\theta$ brightness taper to account for limb darkening (where θ is the emission angle and n = 0.04). Figure is extracted from Le Gall et al. [2014].

the timing offset and the brightness scale factor, are adjusted until the chi-squared sum of the residuals is minimized. T_b^{disk} is derived from the best-fit brightness temperature model as follows:

$$T_{\mathrm{b}}^{\mathrm{disk}} = \frac{1}{\Omega^{\mathrm{disk}}} \int T_{\mathrm{b}}^{m} d\Omega, \qquad \text{Eq. 3}$$

where Ω^{disk} is the disk solid angle and T_b^m the best-fit modeled brightness temperature of each element of solid angle dΩ. The errors on T_b^{disk} are estimated from the least-squares fit. The results are almost insensitive to the choice of a priori model parameters. More details can be found in Janssen et al. [2009].

Table RADAR-6 summarizes all 40 distant radiometry observations of Mimas, Tethys, Enceladus, Dione, Rhea, Iapetus, and Phoebe during the Cassini mission. Note that some radiometer footprints are as small as about 0.4–0.5 satellite diameter. These observations are able to resolve large-scale features at the surface. However, in this report we have chosen to classify them as distant because no scatterometry data were acquired concurrently with the radiometry.

Table RADAR-6. Cassini radiometry distant observations of Mimas, Tethys, Enceladus, Dione, Rhea, Iapetus, and Phoebe.

Target Distant Observation ID[g]	Date Start time End time M, D, Y h:m:s	Sub-spacecraft Point[a] (°E, °N)	Sub-solar Point[b] (°E, °N)	Beam size[c] (Diameter)	$T_b^{disk[d]}$ (K)	Emissivity[e]	Radar albedo[f]
MIMAS MI47	2007 Jun 28 03:38:47 04:01:17	(−50.5, −2.0)	(−40.3, −10.4)	3.89	43.1±1.5	0.56	2.45
MIMAS MI53	2007 Dec 03 00:25:31 03 00:59	(−92.9, 14.8)	(141.0, −10.3)	4.59	41.0±1.8	0.53	N/A
MIMAS MI64	2008 Apr 11 10:21:18 10:54:08	(−166.6, −67.9)	(6.1, −7.5)	2.06	42.7±1.3	0.55	N/A
MIMAS MI126	2010 Feb 13 14:51:31 15:15:11	(97.3, −3.3)	(−76.9, 2.0)	0.77	43.0±0.9	0.56	2.69
ENCELADUS EN03	2005 Feb 17 10:33:29 11:26:59	(128.2, 0.7)	(−65.4, −22.8)	3.29	39.3±1.4	0.66	2.16
ENCELADUS EN04	2005 Mar 09 13:04:24 13:52:58	(−74.1, 0.3)	(51.6, −22.5)	1.29	32.9±0.8	0.54	N/A
ENCELADUS EN32	2006 Nov 09 02:20:41 02:31:06	(114.0, −14.3)	(130.8, −15.2)	1.23	38.8±0.9	0.64	N/A
ENCELADUS EN50	2007 Sep 30 15:21:43 16:00:46	(−131.5, 16.0)	(−71.1, −10.6)	1.59	31.0±0.8	0.51	3.21

Table RADAR-6. Cassini radiometry distant observations of Mimas, Tethys, Enceladus, Dione, Rhea, Iapetus, and Phoebe.

Target Distant Observation ID[g]	Date Start time End time M, D, Y h:m:s	Sub-spacecraft Point[a] (°E, °N)	Sub-solar Point[b] (°E, °N)	Beam size[c] (Diameter)	T_b^{disk}[d] (K)	Emissivity[e]	Radar albedo[f]
ENCELADUS EN61-1	2008 Mar 12 15:01:01 15:49:46	(−108.0, 68.6)	(46.6, −8.0)	2.33	35.0±1.0	0.58	3.49
ENCELADUS EN88-1	2008 Oct 09 12:06:44 12:57:04	(−40.6, 64.4)	(89.7, −4.8)	4.42	36.8±1.6	0.61	N/A
ENCELADUS EN120-1	2009 Nov 02 01:46:02 02:27:42	(60.5, -0.6)	(-107.7, 1.3)	2.02	39.7±1.1	0.66	2.63
ENCELADUS EN120-2	2009 Nov 02 02:44:22 03:21:02	(54.5, −0.7)	(−118.2, 1.3)	1.73	40.6±1.0	0.67	2.63
ENCELADUS EN16-1#	2011 Nov 06 03:02:26 03:14:09	(172.0, 0.0)	(18.0, 11.7)	0.65	Data contamined with Saturn	N/A	N/A
ENCELADUS EN16-2#	2011 Nov 06 03:22:53 03:37:36	(167.8, −0.1)	(14.1, 11.7)	0.51	Data contamined with Saturn	N/A	N/A
ENCELADUS EN16-9#	2011 Nov 06 06:32:49 06:46:30	(−43.3, −0.8)	(−19.1, 11.7)	0.58	37.9±0.9	0.63	N/A
ENCELADUS EN16-10#	2011 Nov 06 06:58:09 07:12:51	(−47.3, −0.7)	(−23.8, 11.7)	0.74	37.5±0.9	0.62	N/A
TETHYS TE15	2005 Sep 24 06:49:46 07:21:41	(152.6, −0.3)	(−42.2, −19.3)	0.94	32.9±0.7	0.47	2.76
DIONE DI16	2005 Oct 11 22:52:51 23:30:41	(−23.6, 0.2)	(140.4, −20.1)	1.12	54.2±1.2	0.76	1.64
DIONE DI50	2007 Sep 30 00:19:29 01:12:39	(152.7, −13.1)	(34.3, −10.4)	0.64	52.8±1.1	0.74	1.58
DIONE DI177-1	2012 Dec 23 05:08:11 05:22:41	(−95.1, 45.7)	(−14.4, 16.9)	1.35	47.6±1.0	0.67	N/A
DIONE DI177-2	2012 Dec 23 05:34:21 05:47:41	(−93.9, 49.0)	(−16.7, 16.9)	1.37	47.3±1.0	0.66	N/A
RHEA RH11	005 Jul 14 09:05:44 09:41:44	(−48.3, −74.7)	(174.8, −20.6)	0.79	46.6±1.0	0.64	1.84

Table RADAR-6. Cassini radiometry distant observations of Mimas, Tethys, Enceladus, Dione, Rhea, Iapetus, and Phoebe.

Target Distant Observation ID[g]	Date Start time End time M, D, Y h:m:s	Sub-spacecraft Point[a] (°E, °N)	Sub-solar Point[b] (°E, °N)	Beam size[c] (Diameter)	T_b^{disk}[d] (K)	Emissivity[e]	Radar albedo[f]
RHEA RH18	2005 Nov 27 04:35:35 05:21:55	(−21.8, 0.2)	(156.8, −19.1)	0.74	50.1±1.1	0.69	1.83
RHEA RH22-1	006 Mar 21 11:03:26 12:57:06	(−135.5, 0.9)	(52.4, −17.8)	0.51	46.5±1.0	0.64	N/A
RHEA RH22-2	2006 Mar 21 13:03:16 14:57:06	(−153.0, 0.7)	(45.8, −17.8)	0.64	47.4±1.0	0.65	1.43
RHEA RH45	2007 May 27 11:21:28 11:49:44	(−57.7, −44.0)	(−157.2, −11.9)	0.84	47.3±1.0	0.65	2.12
RHEA RH49	2007 Aug 29 20:05:06 20:47:36	(15.2, −0.3)	(−114.3, −10.6)	0.51	49.2±1.1	0.68	1.86
RHEA RH127-1	2010 Mar 02 13:42:57 14:30:12	(−159.5, 0.3)	(19.3, 3.1)	0.47	47.2±1.0	0.65	1.43
RHEA RH127-2	2010 Mar 02 14:31:57 15:23:02	(−162.1, 0.4)	(16.6, 3.1)	0.35	47.5±1.1	0.65	1.43
RHEA RH177-1#	2012 Dec 22 20:06:52 20:28:42	(−102.2, −76.0)	(−11.7, 16.6)	0.40	43.7±1.0	0.60	N/A
RHEA RH177-2#	2012 Dec 22 20:38:32 20:57:16	(−91.6, −77.0)	(13.4, 16.6)	0.33	43.5±1.1	0.60	N/A
IAPETUS IA01b-1-In	2004 Dec 31 05:13:48 06:27:51	(−72.1, 37.1) L	(−111.5, −7.5) ☼	0.68	69.6±1.5	0.81	0.54
IAPETUS IA01c-1-Out1	2005 Jan 01 19:04:23 20:45:33	(60.9, 41.0) T	(−118.7, −7.5) ☾	0.97	56.0±1.2	0.65	N/A
IAPETUS IA01c-1-Out2	2005 Jan 01 20:44:23 22:27:13	(61.7, 39.6) T	(119.0, −7.5) ☾	1.02	55.8±1.2	0.65	N/A
IAPETUS IA17-1	2005 Nov 12-13 23:18:50 00:04:40	(1.3, 36.9) T/L	(−97.5, −4.7) ☾/☼	1.84	62.2±1.4	0.72	0.71

Table RADAR-6. Cassini radiometry distant observations of Mimas, Tethys, Enceladus, Dione, Rhea, Iapetus, and Phoebe.

Target Distant Observation ID[g]	Date Start time End time M, D, Y h:m:s	Sub-spacecraft Point[a] (°E, °N)	Sub-solar Point[b] (°E, °N)	Beam size[c] (Diameter)	T_b^{disk}[d] (K)	Emissivity[e]	Radar albedo[f]
IAPETUS IA49-1	2007 Sep 09 07:41:52 08:23:32	(−65.4, 10.8) L	(146.4, 1.5) ☾	1.12	73.4±1.5	0.85	0.34 0.28
IAPETUS IA49-2	2007 Sep 10 00:13:00 01:07:10	(−69.2, 10.7) L	(143.3, 1.5) ☾	0.50	74.1±1.7	0.86	0.34 0.28
IAPETUS IA49-4	2007 Sep 11 03:51:15 04:51:45	(106.8, −10.8) T	(138.1, 1.5) ☼	0.52	59.3±1.3	0.69	0.66
PHEOBE PH3-1	2004 Jun 11 14:31:11 15:22:52	(136.5, −21.7)	(−137.7, −12.8)	3.10	78.7±3.6	0.88	0.29
PHEOBE PH3-2	2004 Jun 12 00:01:19 00:23:48	(−45.5, 22.2)	(−137.2, −12.8)	3.13	69.0±1.9	0.77	N/A
PHEOBE PH3-3	2004 Jun 12 00:25:17 00:47:56	(−61.4, 22.7)	(−152.3, −12.5)	3.42	71.5±2.1	0.80	N/A

a The planetographic coordinate of the apparent sub-spacecraft point is given at the center of the scan. It may change a few degrees along the scan. L and T flag observations of the leading or trailing sides.

b The sub-solar point is given at the center of the raster scan. ☾ and ☼ flag observations of the day or night sides.

c The beam size at the center of the raster scan is expressed in satellite diameter. It is related to the encounter distance by the following relationship: beam size = distance*tan(0.37/2)/radius, where 0.37° is the antenna beamwidth and radius is the mean of the two equatorial radii of the satellite.

d 2.2-cm absolute brightness temperature over the satellite disk. The derived values include statistical and calibration uncertainties.

e Estimate of the disk-integrated emissivity. As in Ostro et al. [2006], we use the isothermal equilibrium temperature T_{eq} as a proxy for the effective physical temperature at 2.2 cm with $T_{eq} = 91.4\ (1-A_{Bond})^{1/4}$, where 91.4 K is the equilibrium temperature for a grey body at Saturn's distance from the Sun and A_{Bond} is the bolometric Bond albedo of the satellite. For this parameter, we use the up-to-date values published in Howett et al. [2010] based on CIRS observations. Note that these Bond albedo values are different from those used in Ostro et al. [2006] and should be more accurate. Indeed, prior to Cassini measurements, only much less accurate and complete Voyager and ground-based data were available, and the leading and trailing values had been measured solely for a few icy satellites. The emissivity is estimated by $T_{\mathrm{b}}^{\mathrm{disk}}/T_{eq}$.

f Radar albedo value for comparison. Only the values acquired during the same flyby and over (almost) the same disk are shown.

g Observations marked with a # are observations that are preceded or followed in an observation of the same disk in the orthogonal polarization.

SCATTEROMETRY-RADIOMETRY RESOLVED OBSERVATIONS

Over the course of the Cassini mission, RADAR had few opportunities to collect spatially resolved scatterometry and radiometry data during close-targeted encounters of icy satellites. For instance, during Cassini's 49th orbit around Saturn (Sept. 9–10, 2007), RADAR was assigned a time slot while the spacecraft was at a range of ~20,000 km from Iapetus. The SAR image obtained during this close encounter is described in Ostro et al. [2010] while the scatterometry data were processed

and analyzed by Wye [2011] and the radiometry data by Le Gall et al. [2014] (see Figure RADAR-38).

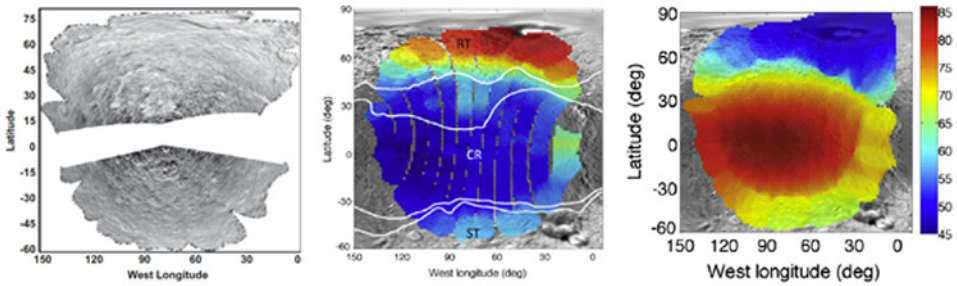

Figure RADAR-38. SAR-scatterometry-radiometry IA49-3 observation. (See Table RADAR-6). Left: SAR image of the leading side of Iapetus acquired during flyby IA49 (September 2007). For this SAR image, a cosine scattering law with exponent 1.5 was subtracted from the original image. Extracted from Ostro et al. [2010]. Middle: Scatterometry data collected during the IA49-3 experiment overlaid on an ISS base map (PIA08406). The normalized backscattering cross-sections are in linear scale and corrected to an incidence angle of 32° using the backscatter analysis conducted by Wye [2011]. Extracted from Le Gall et al. [2014]. Right: Calibrated antenna temperatures recorded during the radiometry IA49-3 experiment overlaid on an ISS base map of Iapetus (PIA08406). Extracted from Le Gall et al. [2014].

Table RADAR-7 lists all resolved scatterometry-radiometry observations of icy satellites during the Cassini mission and, when they exist, the published papers describing these observations.

Table RADAR-7. Cassini radar/radiometry spatially-resolved observations of Enceladus, Dione, Rhea, and Iapetus.

Target Distant Observation ID[g]	Date Start time End time M, D, Y h:m:s	Sub-spacecraft Point[a] (°E, °N)	Sub-solar Point[b] (°E, °N)	Beam size[c] Start End (Diameter)	$T_b^{disk^d}$ (K)	Comments and References
ENCELADUS EN120-3	2009 Nov 02 04:51:52 06:36:52	(34.3, −1.2)	(−179.9, 26.2)	0.50 0.39	N/A	SAR image and scatterometry analysis: Wye [2011]. The radiometry data cannot be calibrated.
ENCELADUS E16 In 1[#]	2011 Nov 06 03:38:37 03:48:15	(165.2, −0.2)	(11.8, 11.6)	0.47 0.33	N/A	The low-resolution SAR images acquired during E16 In 1, 2 and 3 are shown in the SI of Le Gall et al. [2017]. The concurrent radiometry data are contaminated by Saturn's emission.
ENCELADUS E16 In 2[#]	2011 Nov 06 03:59:49 04:20:23	(159.7, −0.5)	(7.1, 11.6)	0.23 0.22	N/A	
ENCELADUS E16 In 3	2011 Nov 06 04:24:29 04:51:26	(152.4, −1.8)	(2.2, 11.6)	0.19 0.04	N/A	
ENCELADUS E16 closest approach	2011 Nov 06 04:58:15 05:00:00	(60, 30)	(-1.5, 11.8)	0.019 0.023	N/A	Active (including high-res SAR) and passive data are shown and discussed in Le Gall et al. [2017].

Table RADAR-7. Cassini radar/radiometry spatially-resolved observations of Enceladus, Dione, Rhea, and Iapetus.

Target Distant Observation ID[g]	Date Start time End time M, D, Y h:m:s	Sub-spacecraft Point[a] (°E, °N)	Sub-solar Point[b] (°E, °N)	Beam size[c] Start End (Diameter)	$T_b^{disk^d}$ (K)	Comments and References
ENCELADUS E16 Out 1	2011 Nov 06 05:07:27 05:52:10	(−29.9, −1.9)	(−6.6, 11.6)	0.05 0.33	43.5±4.9	E16 Out 1 radiometry data are analyzed in Ries and Janssen [2015].
ENCELADUS E16 Out 2#	2011 Nov 06 05:57:10 06:10:22	(−37.3, −1.1)	(−12.8, 11.7)	0.33 0.41	42.5±2.3	E16 Out 2 and 3 radiometry data are shown in Ries and Janssen [2015].
E16 Out 3#	2011 Nov 06 06:22:30 06:31:42	(−41.3, −0.9)	(−16.9, 11.7)	0.48 0.53	40.5±1.5	
DIONE DI163-1	2012 Mar 28 02:01:07 03:36:07	(−16.2, −0.9)	(−135.3, 13.7)	0.56 0.49	57.3±1.7	None
DIONE DI163-2	2012 Mar 28 03:39:07 03:49:07	(−36.4, −1.0)	(−140.4, 13.7)	0.34 0.32	56.1±1.3	None
RHEA RH127-3	2010 Mar 02 15:50:04 16:50:30	(−166.9, 1.1)	(11.7, 3.1)	0.24 0.11	N/A	The SAR image and scatterometry observation are shown and analyzed in Wye [2011].
IAPETUS IA49-3	2007 Sep 10 11:19:42 12:17:47	(−76.9, 10.4)	(141.2, 1.5)	0.11 0.07	76.8±6.5	SAR image: Ostro et al. [2010]. Scatterometry analysis: Wye [2011]. Radiometry analysis : Le Gall et al. [2014].

a The planetographic coordinate of the apparent sub-spacecraft point is given at the center of the scan. L and T flag observations of the leading or trailing sides.

b The sub-solar point is given at the center of the raster scan. ☾ and ☼ flag observations of the day or night sides.

c The beam size at the center of the raster scan is expressed in satellite diameter.

d 2.2-cm absolute brightness temperature over the satellite disk. When possible, the values are derived as described in the section entitled Distant passive raster-scans.

e Observations marked with a # are observations that are preceded or followed in an observation of the same disk in the orthogonal polarization.

Note that flyby E16 was the only Enceladus' encounter dedicated to RADAR. The SAR image was acquired within 2 min centered around closest approach, while the spacecraft passed the moon at distance of about 500 km, has the highest spatial resolution (~50 m in the cross-track direction, ~200 m in the along-track direction) ever achieved for SAR imagery on any icy satellite. These high-resolution datasets and the concurrent radiometry were analyzed in Le Gall et al. [2017]. Medium-resolution radar/radiometry data were also acquired before and after the E16 closest approach—see the inbound and outbound low-resolution SAR images in Figure RADAR-39 and West et al. [2012]. Unfortunately, half of the concurrent radiometry data were contaminated by

emission from Saturn (and its rings), which was behind Enceladus' disk during the inbound leg of the observation [Ries and Janssen 2015].

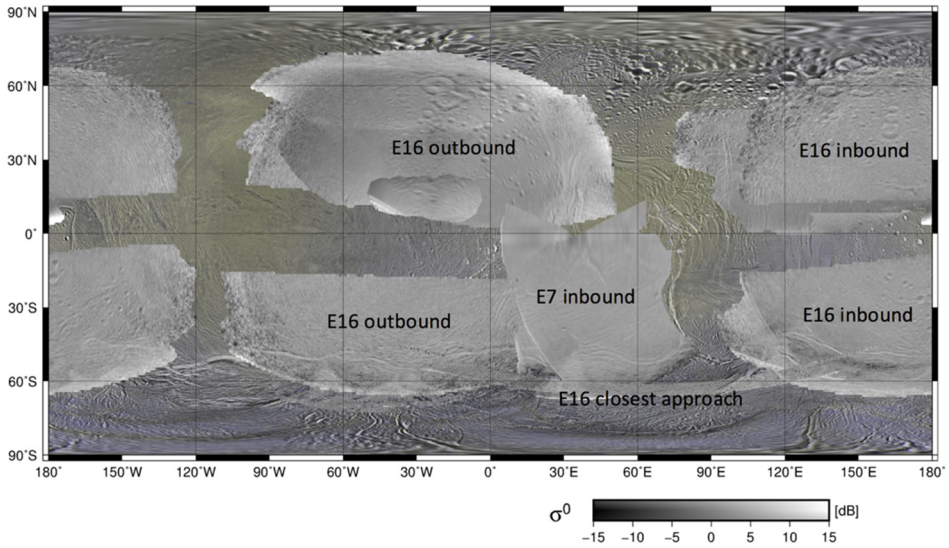

Figure RADAR-39. Mosaic of the EN120 (also called E7) and E16 SAR images of Enceladus overlaid on a color mosaic of Enceladus produced by the Cassini ISS (PIA18435). The measured normalized backscatter cross-sections are in dB and have been corrected for incidence-angle effects and biases due to thermal and quantization noises. Figure is extracted from the Supplementary Material of Le Gall et al. [2017].

Lastly, the first resolved observation of Enceladus was acquired during the inbound leg of the 7th targeted encounter of the moon (often referred to as E7 or EN120) that occurred on November 2, 2009. Following a distant observation, the spacecraft turned to offset the central beam to a suitable imaging area and RADAR collected high-altitude scatterometry imaging and radiometry data down to an altitude of about 30,000 km [Wye 2011]. The resulting low-resolution SAR image has some overlap with the E16 high-resolution SAR observation (see E7 inbound in Figure RADAR-39). However, the concurrent radiometry data cannot be properly calibrated because the receiver temperature was not stabilized during this observation.

Science results and open questions

In this section, we summarize the major science results obtained thanks to RADAR observations of Saturn's icy satellites. When possible, these observations are analyzed in light of observations at other wavelengths or by comparison with radio observations of other icy objects.

Measure of the degree of scattering in the subsurface

Among all the radar-detected planetary bodies in the solar system, the ice-rich satellites of both the Saturn and Jovian systems have the most unusual radar properties. Their reflectivities are very high and they exhibit peculiar polarization properties [Black et al. 2001]. The general understanding

gained so far about the radar properties of the Saturnian satellites icy surfaces, including Titan, at the Cassini 2.2 cm wavelength is that they are dominated by subsurface volume scattering [Ostro et al. 2006; Wye et al. 2007; Zebker et al. 2009a; Janssen et al. 2009].

More accurately, if refraction scattering from dielectric inclusions [Hagfors et al. 1985; Hagfors et al. 1997] or interface cracks [Goldstein and Green 1980] can play a role, the generally accepted explanation is that most icy satellites' radar behavior is related to an effect called the coherent backscatter effect [Hapke 1990; Ostro 1993; Black et al. 2001]. This effect is due to volume scattering from within the satellites' regolith, which, on icy satellites, can be regarded as an extremely low-loss and disordered random medium.

The high radar transparency of ice at temperatures as low as 100 K [Thompson and Squyres 1990; Matzler 1998; Lorenz 1998] compared with that of silicates indeed permits deeper radar sounding (10–100 wavelengths), longer photon path lengths, and thus higher order scattering from regolith heterogeneities (voids, rocks) producing large backscatter and reducing the emissivity (Figure RADAR-40). The purer and the more structurally complex the subsurface, the higher the radar albedo and the lower the emissivity. Both in its active and passive modes, the Cassini RADAR therefore measures quantities that are closely related to the degree of purity of the regolith and to its structural heterogeneity/complexity.

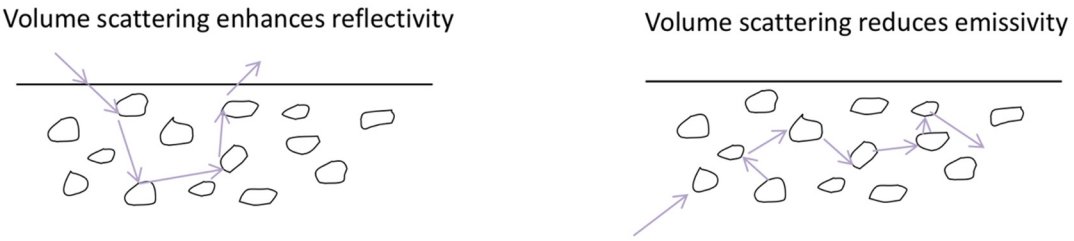

Figure RADAR-40. Effect of volume scattering on the measured reflectivity and emissivity. A low-loss and structurally complex regolith provides enhanced opportunity for scattering, which increases the reflectivity and reduces the emissivity (because it prevents the emitted waves from escaping the subsurface).

INTER-SATELLITE RADAR ALBEDO AND EMISSIVITY VARIATIONS

Figures RADAR-41, RADAR-42, and RADAR-43 show that active and passive signatures differ from one satellite to another—see also Black et al. [2007]; Ostro et al. [2006]—thus indicating various degrees of volume scattering in their subsurface, i.e., various degree of purity and/or complexity of their regolith and thus differences in their composition and/or the various processes that have modified their structure.

For Ostro et al. [2006], variations in terms of composition, rather than structure, is the main source of satellite-to-satellite variabilities. More specifically, they invoke an increase in surface contaminants of Saturnian satellites to explain the observed proportional decrease in radar albedo and the concurrent increase in emissivity in the order Enceladus/Tethys, Mimas, Rhea, Dione,

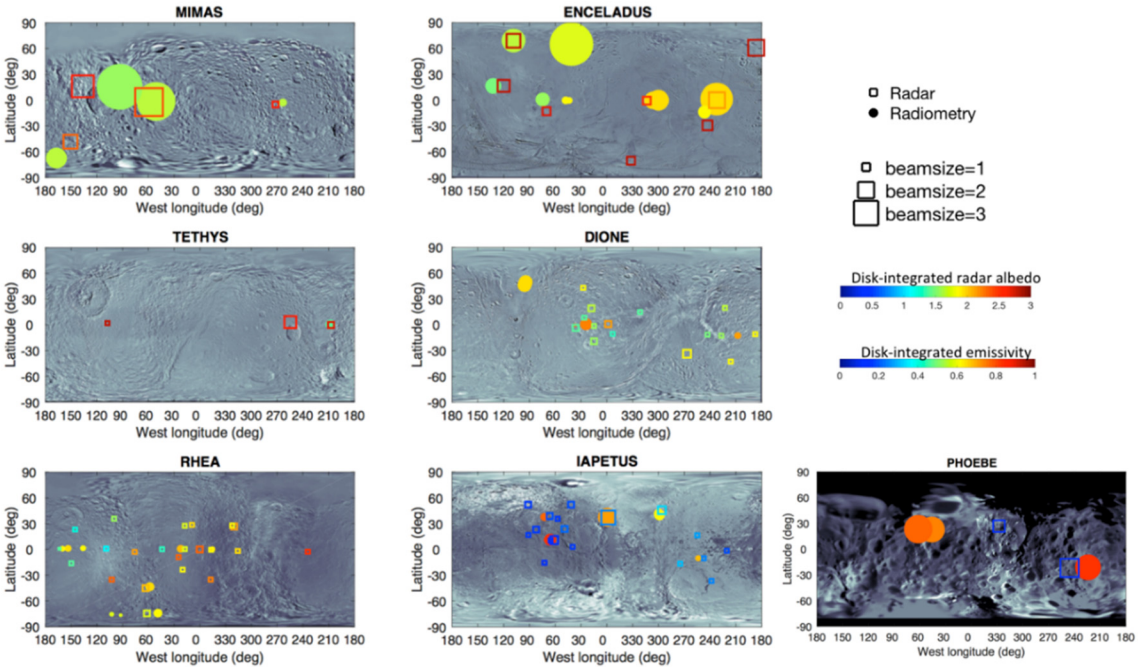

Figure RADAR-41. Sub-radar locations of distant active-radar and radiometry observations of Mimas, Tethys, Enceladus, Dione, Rhea, Iapetus, and Phoebe acquired during the Cassini mission, overlaid on the near-IR ISS mosaics of each satellite. The square symbols correspond to active stare observations while the circle symbols correspond to distant radiometry measurements. The color codes indicate the value of the derived disk-integrated radar albedo for the squares and that of the derived disk-integrated emissivity for the circles, respectively. The size of the symbols indicates the ratio between the beamwidth of the observation and the target angular diameter. The sub-Saturn longitude occurs at zero and the leading side is centered on 90° W longitude.

Iapetus, and Phoebe (see Figures. RADAR-42 and RADAR-43). An argument in favor of this hypothesis is the strong correlation between the radar and optical albedos of the satellites—see Figure 4 in Ostro et al. [2006]. This suggests that an increasing concentration of optically dark contaminant(s) in the near-surface leads to the attenuation of the high-order multiple scattering in the subsurface (water ice being transparent to radio wavelengths) and thus to smaller albedos and larger emissivities. Note that Phoebe, the dimmest of the targets, is nevertheless twice as radar bright as the Moon [Ostro et al. 2006]. The nature of the contaminant(s) remains unknown but Ostro et al. [2006] propose possible candidates including silicates, metallic oxides, and polar organics such as nitriles or complex tholins.

Taking a step further, the active radar and radiometry sequences shown in Figures RADAR-42 and RADAR-43 as well as the hemispheric dichotomies observed at 2.2 cm can be, at first order, explained by variations in term of surface contamination as the result of the competition between several effects including:

- The coating effect of the E-ring
- The coating effect of the vast debris ring from Phoebe

- The geological and thermal history of the icy satellite
- The efficiency of space weathering at the position of the icy satellite within Saturn's magnetosphere

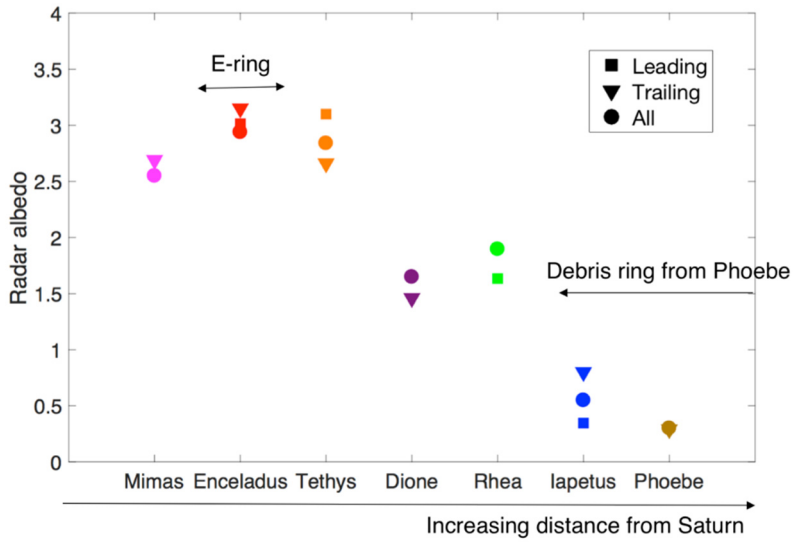

Figure RADAR-42. Radar albedos derived from Cassini active stare observations of Mimas, Enceladus, Tethys, Dione, Rhea Iapetus, and Phoebe. For each satellite, when available, values are shown separately for the leading and trailing sites (in the latitudinal band (−30°, 30°)) in order to reveal possible hemispheric dichotomy. The locations of the E-ring and the vast debris ring from Phoebe are indicated.

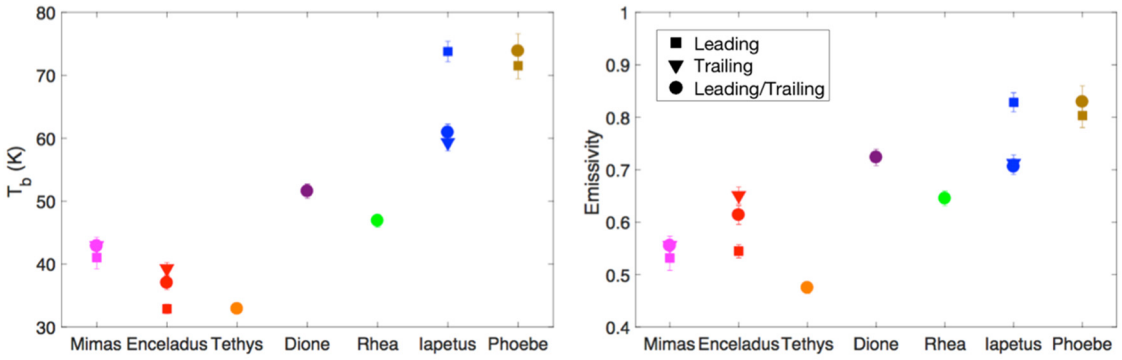

Figure RADAR-43. Disk-integrated brightness temperatures (left) and estimated emissivities (right) derived from Cassini passive distant observations of Mimas, Enceladus, Tethys, Dione, Rhea, Iapetus, and Phoebe. For each satellite, when available, values are shown separately for the leading and trailing sites (in the latitudinal band (−30°, 30°)) in order to reveal possible hemispheric dichotomy. Note that the error bars on the emissivity results only take into account the measurement errors, not the error related to the fact that the isothermal equilibrium temperature was taken as a proxy for the effective physical temperature of the near-surface. A more accurate method to constrain emissivity is described in Le Gall et al. [2014].

Around Enceladus, the E-ring guarantees the deposition at the surface of extremely clean water ice that may also be structurally complex and thus very favorable to volume scattering. The decrease in radar brightness from Enceladus outward would then be due to the outward decrease in E-ring flux [Verbiscer et al. 2007] and hence the endowment of the satellite surface with ultra-clean ice. At the other extreme (moving inward from Phoebe), on the contrary, the diffuse debris ring from Phoebe progressively coats surfaces with material of low reflectivity. Geological activity brings fresh water ice at the surface and, if not too ancient, should therefore be associated with especially high albedos. Lastly, the efficiency of space weathering decreases with the distance to Saturn, which may have various implications on the microwave signatures of the icy satellites. For instance, close to Saturn, the magnetospheric ion bombardment should favor ammonia depletion in the near-surface and thus a higher degree of a purity of the water-ice regolith [Lanzerotti et al. 1984; Ostro et al. 2006]. On the other hand, gravitational focusing enhances the meteoroid flux close to Saturn—for example, Morfill et al. [1983]—which should lead to a higher contamination by non-ice compounds.

The differences between Saturn's icy satellites at 2.2 cm wavelength are further discussed in the section entitled Intra-satellite variations: Hemispheric dichotomies.

VARIATIONS WITH WAVELENGTH/DEPTH

Hints on the vertical variations of the regolith can be inferred from comparison of radio observations at different wavelengths. The 13 cm wavelength radar albedos measured from the Arecibo radar system [Black et al. 2004, 2007], once converted into same-sense albedos—from total power albedos as described in Ostro et al. [2010]—are all lower than the albedos obtained with the Cassini radar instrument at 2.2 cm (see Figure RADAR-44).

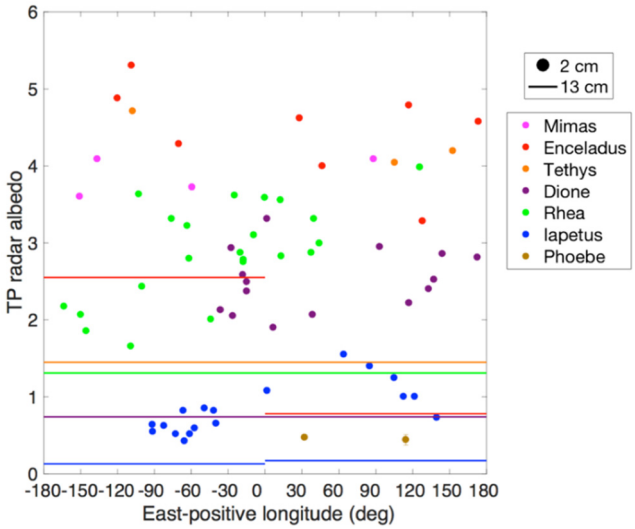

Figure RADAR-44. Total-power (TP) radar albedos of Saturn's icy satellites at the 2.2 cm (dots) and the 13 cm wavelengths (lines). The TP albedos at 2.2 cm were derived from the same-sense radar albedos measured by the Cassini radar as described in Ostro et al. [2010]. The TP albedos at 13 cm are Arecibo measurements averaged over the indicated longitude spans. See the caption of Figure 4 in Ostro et al. [2010] for more details.

The strong drop in radar albedo from 2.2 to 13 cm suggests that either the composition and/or structure is a function of depth everywhere (with e.g., electrical loss much greater at depths or a decrease with depth in the number density of efficient scatterers), or the regolith material is dispersive (with higher losses at higher wavelength). Ostro et al. [2010] favor the hypothesis of a decreasing ice cleanness with depth. Black and al. [2004] and Ostro et al. [2010] both invoke ammonia as the most likely contaminant: a lower abundance of ammonia within the upper one or two decimeters of the ice-rich regolith than at greater depths would account for the observations.

The specific cases of Enceladus and Iapetus for which Arecibo data show, respectively, a hemispheric dichotomy and no hemispheric dichotomy are discussed in the following subsections.

INTRA-SATELLITE VARIATIONS: HEMISPHERIC DICHOTOMIES

Almost all Saturnian icy satellites exhibit longitudinal variations in their microwave signatures, especially between their leading and trailing sides (see Figures RADAR-41, RADAR-42, and RADAR-43). These hemispheric dichotomies provide essential clues on the mechanisms that have primarily affected their near-surface.

IAPETUS' TWO-FACE

The most dramatic hemispheric dichotomy in the Saturnian system occurs at Iapetus, whose trailing side and poles are about an order of magnitude optically brighter than most of its leading hemisphere. The origin of this two-tone coloration has long been controversial, but there seems to now be a consensus toward an exogenic deposition of low-albedo materials probably originated in the region of Phoebe, or the vast debris ring from Phoebe, that crosses Iapetus' orbit—for example, Cruikshank et al. [1983], Buratti et al. [2002], Verbiscer et al. [2009], and Tosi et al. [2010b]. It has also been proposed that the darkening of the leading hemisphere is enhanced by the thermal segregation of water ice leaving behind a darker remnant material in the relatively warm equatorial region [Dalle Ore et al. 2012].

At 2.2 cm, the satellite's radar albedo and emissivity mimic the optical dichotomy, which implies that the leading side's optically dark contaminant must be present to depths of at least one to several decimeters [Ostro et al. 2006, 2010; Le Gall et al. 2014] (see Figures RADAR-41, RADAR-42, RADAR-43, and RADAR-44). On the other hand, at 13 cm, values of the radar albedo from the Arecibo radar system show no significant longitudinal pattern [Black et al. 2004] (see Figure RADAR-44). This strongly suggests that the thickness of the dark layer is no more than a few meters, which is also consistent with the discovery of small bright-ray and bright-floor craters within the dark terrain.

As a further argument, the thermal inertia of Iapetus' dark terrains inferred from Cassini IA49-3 resolved radiometry observations (see Table RADAR-6 and Figure RADAR-38) is much higher than that inferred from CIRS measurements [Howett et al. 2010], which sense only the uppermost layers of the surface [Le Gall et al. 2014]. This suggests a gradient in density with depth or, more

likely, that the radiometer has probed the icy substrate underlying the dark layer. Radiometry measurements also indicate a progressive thinning of the dark layer away from the equator.

In addition, Le Gall et al. [2014] show that the measured thermal emission during IA49-3 arises from several meters of the subsurface, which points to tholins, rather than iron oxide compounds, as the primary contaminants of the dark material. They also find that the dark terrains of Iapetus exhibit a 2.2 cm emissivity close to the emissivity of Phoebe (see Figure RADAR-43), which brings a further argument in favor of a common origin of their darkening agent.

ENCELADUS' YOUNG LEADING HEMISPHERE

Enceladus' 2.2 cm active observations show no dramatic leading/trailing asymmetry (see Figures RADAR-39 and RADAR-42), but passive observations, both unresolved (see Figure RADAR-43) and resolved (see Figure RADAR-45) do. Radiometry observations indeed show that the leading side of Enceladus is about 30% less emissive than its trailing side [Ries and Janssen 2015]. Such a dichotomy is also observed in Arecibo 13 cm measurements, which reveal a much brighter leading side [Black et al. 2007] (see Figure RADAR-44.)

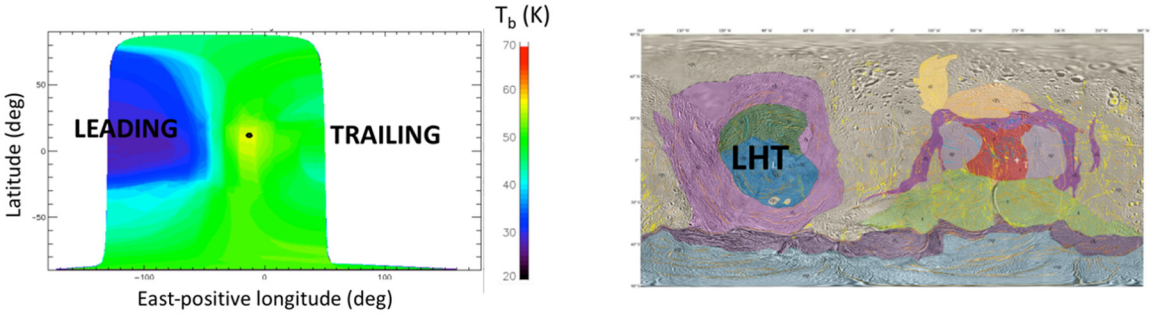

Figure RADAR-45. Resolved passive observations. Left: Deconvolved brightness temperatures measured during E16-Out1 (see Table RADAR-6). Credits: L. Bonnefoy. Right: Structural units of Enceladus as mapped by Crow-Willard and Pappalardo [2015].

Ries and Janssen [2015] propose that the leading side anomaly is an anomaly of scattering, associated with a seemingly young tectonized terrain called the Leading Hemisphere Terrain (LHT)—see Figure RADAR-44 and Crow-Willard and Pappalardo [2015]. In this picture, the LHT would be young enough (75–200 million years) to have been reprocessed (e.g., by micrometeoritic bombardment) only down to a depth shallower than the electrical skin depth at 2.2 cm (a few meters at most) contrary to the trailing side. This would be the reason why the leading/trailing dichotomy is not visible in 2.2 cm active data, which probe the subsurface down to a smaller depth than concurrent passive measurements and observations at 13 cm.

Alternatively, we note in Figure RADAR-42 that the trailing side of Enceladus is actually slightly brighter at 2.2 cm than its leading side. This suggests that, at the depth sensed by RADAR in active mode, the coating effect of the E-ring (which should be more widespread on the trailing side of Enceladus [Kempf et al. 2010]) prevails over the effect of space weathering and/or over the detection of the underneath leading-side young terrain. This would imply that the deposition rate of plume

particles at the surface of Enceladus is larger than estimated by Kemp et al. [2010] and, more specifically, larger than the reprocessing rate by micrometeoritic gardening [Cooper et al. 2001].

AROUND THE E-RING

The coating effect of the E-ring may also be responsible for the clear leading/trailing radar albedo dichotomy observed on Tethys and the hint of similar asymmetry observed on Mimas (see Figure RADAR-42).

We recall that for Rhea, Dione, and Tethys, which lie outside the densest part of Saturn's E-ring, the deposition of icy particles from Enceladus' plumes should be preferentially on the leading side. But Mimas and Enceladus, which are inside the E-ring, should be bombarded on their trailing side [Hamilton and Burns 1994; Buratti et al. 1998]. This is consistent with Figure RADAR-42, which shows a brighter leading hemisphere for Tethys while it is Mimas' trailing side that is brighter.

Cassini active observations also support the idea that the Pac-Man anomalies detected by the CIRS instrument are shallow. We recall that the CIRS instrument has detected, first on the leading side of Mimas and then of that of Tethys, a thermally anomalous extensive region shaped like the 1980s video game icon Pac-Man [Howett et al. 2011, 2012]. Both on Mimas and Tethys, the anomalous region coincides, in shape and location, with a region of preferential bombardment by high-energy electrons from Saturn's magnetosphere. The anomaly occurs because the MeV electrons penetrate into the subsurface gluing the water grains along their path and thus enhancing the thermal inertia. Evidence for a similar surface alteration by high-energy electrons was also detected on the leading side of Dione [Howett et al. 2014] but with a more tenuous expression as expected since the efficiency of the alteration must decrease with increasing distance to Saturn.

Given the small penetration depths of the MeV electrons into the subsurface (a few cm), the Pac-Man effect should not be detectable at 2.2 cm wavelength and the fact that we observe opposite albedo dichotomies on Mimas and Tethys (Figure RADAR-42) is a further argument for the dominant effect of coating by plume particles around Enceladus.

However, the Pac-Man effect may explain why slightly higher disk-integrated brightness temperatures were measured on the trailing side of Mimas (Figure RADAR-43). This can be confirmed or refuted by comparison of the radiometry data with a thermal model that accounts for the season and local hour of passive observations. In addition, the E-ring coating scenario implies the presence of at least a few meters of fresh water-ice material at the surface, which must be validated by model predictions of the deposition rate of particles from the plumes at the surface of Enceladus' neighbors.

DIONE'S PAST GEOLOGICAL ACTIVITY

The leading side of Dione is much brighter than its trailing side (see Figures RADAR-42 and RADAR-46). As for Enceladus, this is most likely the result of past geologic activity and the resultant resurfacing by fresh water ice. Most of Dione's leading side is indeed covered by smooth terrains [Schenk and Moore 2009] and must have a long resurfacing history [Kirchoff and Schenk 2015].

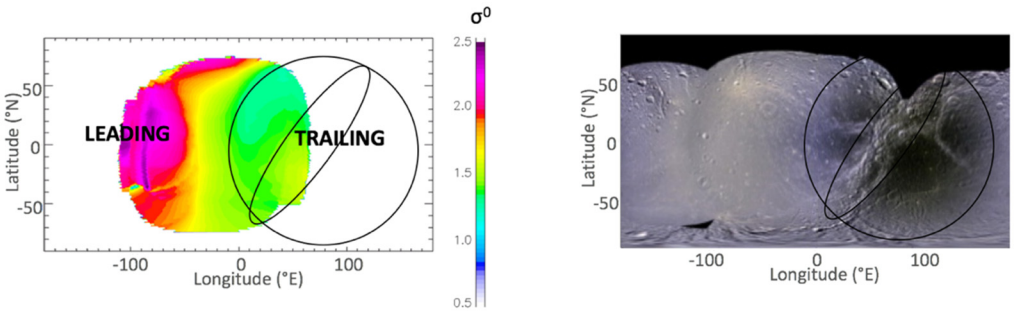

Figure RADAR-46. Trailing side of Dione. Left: Normalized backscattering cross-sections measured during DI 163-1. Credits: L. Bonnefoy. Right: Global mosaic of Dione composed of Cassini Imaging Science Subsystem images [Schenk et al. 2011].

RHEA'S PUZZLING HEMISPHERIC DICHOTOMY AND ENHANCED BRIGHTNESS

Figure RADAR-42, as well as the spatially resolved observations acquired during RH 127-3 (see Table RADAR-6), suggest that Rhea's leading side is radar-darker than its trailing side. Interestingly, Rhea has an optically brighter leading side—so, contrary to Tethys and Dione, there is an opposite correlation between the radar and the optical albedos. In addition, Rhea is surprisingly brighter (and concurrently less emissive) than Dione (see Figures RADAR-42 and RADAR-43). Rhea is also brighter than Dione at 13 cm (see Figure RADAR-44). The cause of this enhanced brightness is not well understood but it could be related to the weaker efficiency of space weathering at the location of Rhea's orbit as suggested by Scipioni et al. [2014] to explain VIMS observations.

Figure RADAR-47 summarizes the likely origins of the inter- and intra-satellites' radar albedo and emissivity variations.

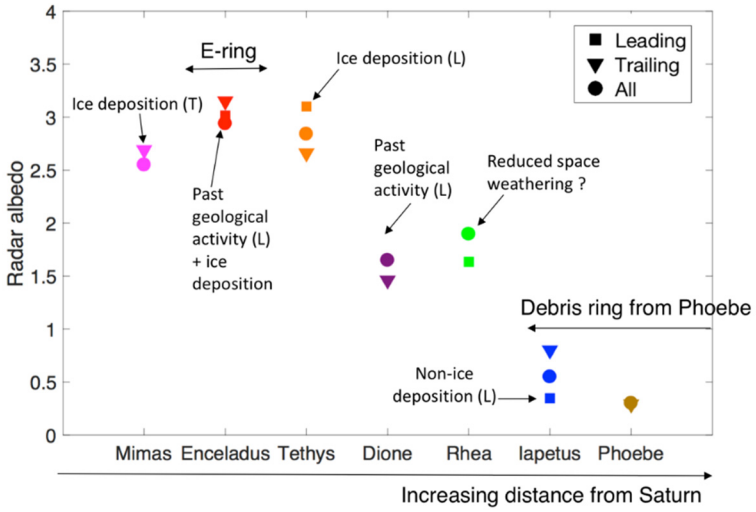

Figure RADAR-47. Radar albedos derived from Cassini active stare observations of Mimas, Enceladus, Tethys, Dione, Rhea, Iapetus, and Phoebe. (See section Distant Active Stares). For each satellite, when available, values are shown separately for the leading and trailing sites (in the latitudinal band (−30°, 30°)) in order to reveal possible hemispheric dichotomy. The possible mechanisms at the origin of the observed inter- and intra-satellite radar albedo and emissivity variations are indicated.

ENCELADUS' SOUTH POLE THERMAL ANOMALY

In 2005, the Cassini spacecraft witnessed for the first time water-rich jets venting from four anomalously warm fractures (also called sulci) near its South Pole [Porco et al. 2006; Spencer et al. 2009]. Since then, several observations have provided evidence that the source of the materials ejected from Enceladus is a large-scale underground ocean whose depth is still debated [Iess et al. 2014; Thomas et al. 2016].

In November 2011, during the closest approach of the 16th Enceladus encounter (flyby E16), RADAR had its first and only opportunity to closely observe Enceladus' south polar terrain (SPT), a few tens of km north of the active sulci (see Figure RADAR-48). At a distance of ~500 km from the surface, the instrument acquired a SAR image (see Figure RADAR-39) and recorded the 2.2 cm wavelength thermal emission of a ~500 km long, ~25 km wide, arc-shaped region centered at 63° S and 295° W and located 30–50 km north of the thermally active sulci identified as the sources of Enceladus' jets.

Le Gall et al. [2017] demonstrate that the brightness temperatures measured during E16 are too high for a purely exogenic explanation, with implications for endogenic processes and heat transport in the Enceladus' SPT. More specifically, they report the detection of prominent thermal anomalies that had not been identified before in the South Pole of Saturn's moon Enceladus (Figure RADAR-48). These anomalies coincide with large fractures, similar or structurally related to the four faults from which Enceladus jets are venting. Their presence implies a broadly distributed heat production and transport system below the south polar terrain of the icy moon with plate-like features. It also suggests that a liquid reservoir could exist at a depth of only a few kilometers under the ice shell at the South Pole—as also supported by interpretation of the libration, topography,

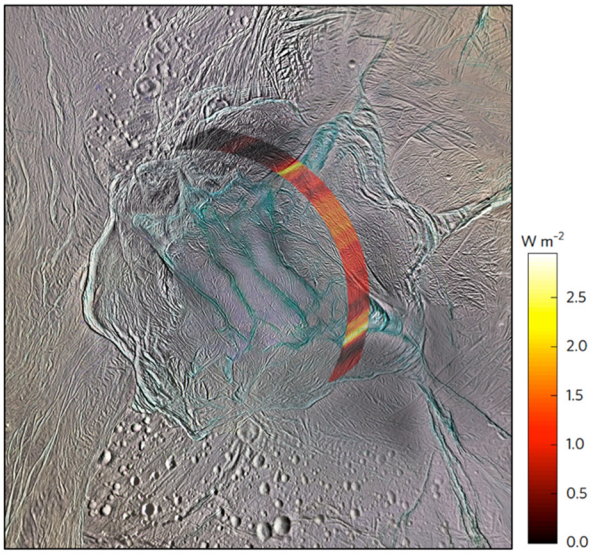

Figure RADAR-48. Minimum flux in excess in the region of Enceladus' SPT observed by the Cassini radar during the closest approach of E16. These values were derived from the E16 resolved radiometry observations by comparison with a thermal + radiative transfer model.

and gravity data [Čadek et al. 2016]—which has important implications for the search of habitable worlds in the solar system.

WHY ARE THEY SO BRIGHT?

Despite our good first-order understanding of the origins of the observed satellite-to-satellite variations and hemispheric dichotomies, an open question persists: why are these icy objects so bright at centimetric wavelengths? In the following subsection, we show that the radar albedos measured over most of Saturn's moons are enhanced beyond what can be explained by random scattering models commonly invoked for icy solar system surfaces. We then propose some explanations.

BACKGROUND: RELATIONSHIP BETWEEN RADAR ALBEDO AND EMISSIVITY FOR SATELLITES WITH IDEAL UNIFORM SURFACES

Radar reflectivity and thermal radiometry for any surface are related through Kirchhoff's law of thermal radiation, and the comparison of these quantities offers an approach to understanding the nature of planetary surfaces that is complementary to that using either radar or radiometry alone.

The emissivity of a surface at a given wavelength and its reflectivity at the same wavelength are related through the Kirchhoff's law of thermal radiation combined with the principle of conservation of energy, as follows:

$$e_p(\theta,\varphi) = 1 - A_p(\theta,\varphi). \quad \text{Eq. 4}$$

A_p is the reflectivity of the surface, i.e., the hemispheric albedo obtained by integrating the reflectivity of a wave incident from the direction (θ,φ) and for the polarization p over the hemisphere.

With radar applications specifically in mind, Peake [1959]—see also Ulaby et al. [1981, 1982]—derived an expression that relates the reflectivity of the surface to its bistatic radar cross-sections:

$$A_p(\theta,\varphi) = \frac{1}{4\pi}\iint_{upper\ hemisphere}\left(\frac{\sigma^0_{pp}(\theta,\varphi;\theta_s,\varphi_s)+\sigma^0_{pq}(\theta,\varphi;\theta_s,\varphi_s)}{\cos\theta}\right)\sin\theta_s d\theta_s d\varphi_s, \quad \text{Eq. 5}$$

where σ^0_{pp} and σ^0_{pq} are the bistatic cross-sections for the scattering of the incident wave into the direction (θ_s,φ_s) in respective orthogonal polarizations p and q.

The Cassini RADAR, like most radars, only measures the cross-section in the backscattering direction (i.e., for $\theta=\theta_s$ and $\varphi=\varphi_s+\pi$) in same-sense polarization (i.e., σ^0_{pp}). However, Janssen et al. [2011] show that for an idealized diffuse scattering surface following a cosine power law (i.e., $\sigma^0_{pp}(\theta,\varphi;\theta,\varphi)=Acos^n\theta$), the emissivity viewed in the (θ,φ) direction can be obtained from:

$$e_p(\theta,\varphi) = 1-\left(\frac{1+\mu_L(\theta,\varphi)}{2n}\right)A, \quad \text{Eq. 5}$$

where $\mu_L$is the linear polarization ratio : $\mu_L(\theta,\varphi) = \sigma^0_{pp}(\theta,\varphi;\theta,\varphi)/\sigma^0_{pq}(\theta,\varphi;\theta,\varphi)$. By definition, $\mu_L$is between 0 (no depolarization) and 1 (full depolarization).

Further, if the coherent backscattering effect [Hapke 1990] is considered:

$$e_p(\theta,\varphi) = 1 - \left(\frac{1+\mu_L(\theta,\varphi)}{2f_{cbe}n}\right)A, \quad \text{Eq. 6}$$

where f_{cbe} is between 1 (no coherent backscattering effect) and 2 (maximum coherent backscattering effect).

The disk-integrated radar albedo $A^{\text{disk}}_{\text{SL}-2}$ was derived from distant active stares based on the same assumption of a purely diffuse scattering surface (see the section entitled Distant Active Stares) and according to Eq. 2:

$$A = \frac{(n+1)}{2}A^{\text{disk}}_{\text{SL}-2}. \quad \text{Eq. 7}$$

The disk-integrated emissivity is thus related to the disk-integrated radar albedo as follows:

$$e^{disk} = 1 - \left(\frac{1+\mu_L(\theta,\varphi)}{2f_{cbe}n}\right)\frac{(n+1)}{2}A^{\text{disk}}_{\text{SL}-2}. \quad \text{Eq. 8}$$

It follows that if the surface is isotropic ($n = 1$) and fully depolarizing ($\mu_L(\theta,\varphi) = 1$):

$$1 - A^{\text{disk}}_{\text{SL}-2} \leq e^{disk} \leq 1 - \frac{A^{\text{disk}}_{\text{SL}-2}}{2}. \quad \text{Eq. 9}$$

If the surface is Lambertian ($n = 2$) and fully depolarizing ($\mu_L(\theta,\varphi) = 1$):

$$1 - \frac{3}{4}A^{\text{disk}}_{\text{SL}-2} \leq e^{disk} \leq\leq 1 - \frac{3}{8}A^{\text{disk}}_{\text{SL}-2}. \quad \text{Eq. 10}$$

Distant active and passive data acquired over icy satellites are discussed in the following subsection in light of this purely random-scattering model.

RADAR VERSUS RADIOMETRY, MODEL VERSUS OBSERVATIONS

Even if there is some variability that is primarily indicative of various degrees of cleanness of the water-ice regolith. Figure RADAR-49 shows that all Saturnian icy satellites, except maybe for Phoebe and Iapetus, are anomalously radar-bright.

Indeed, generic scattering models that depend on purely random scattering processes alone cannot explain the combined radiometric and radar distant observations of Mimas, Enceladus, Tethys, Dione, and Rhea. The distribution of the observed emissivities show an approximately linear relationship with the radar albedo as predicted by the modeling, but with a slope a factor of two larger than the most extreme model considered. The factor of two discrepancy between model expectation and observation already allows for maximum coherent scattering, and is well beyond the range that could be accommodated by any conceivable imbalance in the distribution of bistatic

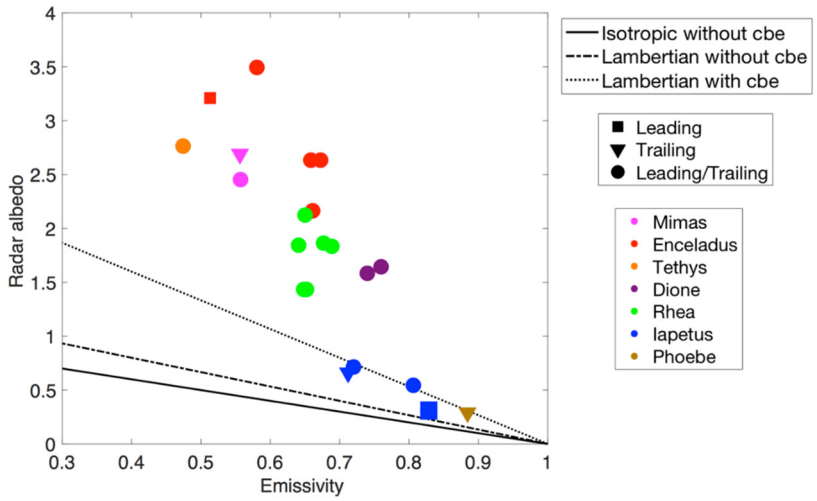

Figure RADAR-49. Disk-integrated same-sense radar albedos versus disk-integrated emissivities derived from the Cassini distant observations of Mimas, Enceladus, Tethys, Dione, Rhea, Iapetus, and Phoebe. When available, the values are shown separately for the leading and trailing sites (in the latitudinal band (−30°, 30°)). The black lines are predictions from the purely random-scattering model described earlier. The measured radar albedos are much larger than expected.

polarization, which is assumed to be the equal in the model. Further, the absolute uncertainties in both emissivity (0.02) and radar albedo (1.4) would have to be seriously underestimated to accommodate the difference as well.

A similar discrepancy has been observed on Titan, on a radar-bright region called Xanadu. Janssen et al. [2011] argue that on Xanadu the mechanism responsible for the enhanced backscatter is related to the presence of ordered structures on or within the surface. There are many theoretical possibilities for such an enhancement, for example a layer of corner cube reflectors, while the challenge is to select those that are geologically plausible for all Saturnian icy satellites. For example, Le Gall et al. [2010] have explained the high radar brightness of some river channels on Titan as due to layers of rounded ice river rocks created by fluvial processes. Maybe more relevant to the surface of Saturn's atmosphereless icy satellites, the unusual radar cross-sections seen in the percolation zone of the Greenland ice sheet were modeled as due to ice cylinders/pipes [Rignot et al. 1993; Rignot 1995]. The presence of cracks or fissures with a preferred orientation in the icy crusts of the Saturnian airless moons is another possibility to be examined.

More recently, Mitchell et al. [2018] have advanced other explanations to accommodate the extreme brightness of Enceladus including the presence of ferroelectric Ice XI, which has unknown backscattering properties, and the sintering of fine particles, which creates larger subsurface particles and/or layering effects that could enhance volumetric radar backscatter. More modeling and laboratory work are required to place more detailed constraints on these hypotheses.

Open questions

RADAR has provided unique insights into the thermal, structural, and compositional properties of the near-surface of Saturn's airless satellites, namely Mimas, Enceladus, Tethys, Dione, Rhea, Hyperion, Iapetus, and Phoebe. It has revealed a number of regional anomalies and satellite-to-satellite variabilities. However, many questions remain about the origin and evolution of Saturn's moons and, in particular, about their respective geological history and interaction with Saturn and its rings. Until the Cassini mission, microwave observations of Saturnian satellites were rare. RADAR observations have set the stage for future researches using ground-based measurements at multiple frequencies in the radio domain—with, for example, the VLA and ALMA radio interferometers or the Institut de Radio Astronomie Millimétrique (IRAM) radio telescope. These measurements will nicely complement Cassini's observations by exploring the thermophysical and compositional properties of the regolith of Saturn's moons at different depths and epochs. Furthermore, future missions to Saturn could include an instrument sounder similar to Mars Advanced Radar for Subsurface and Ionosphere Sounding (MARSIS) /Mars Express, Shallow Radar (SHARAD) / Mars Reconnaissance Orbiter (MRO), or Radar for Europa Assessment and Sounding: Ocean to Near-surface (REASON) / Europa Clipper. Such a radar could, in particular, determine the vertical extent and structure of the dark cover of Iapetus's leading side and confirm the recently advanced hypothesis that the liquid ocean of Enceladus is only a few kilometers under the ice shell at the South Pole of the moon.

ACRONYMS

Note: For a complete list of Acronyms, refer to Cassini Acronyms – Attachment A.

ALMA	Atacama Large Millimeter/submillimeter Array
AO	Announcement of Opportunity
ASI	Italian Space Agency
CIRS	Composite Infrared Spectrometer
GCM	global circulation model
GCMS	Gas Chromatograph Mass Spectrometer
GhoSST	Grenoble Astrophysics and Planetology Solid Spectroscopy and Thermodynamics
HGA	high-gain antenna
IDS	Interdisciplinary Scientist
IR	infrared
IRAM	Institut de Radio Astronomie Millimétrique
ISS	Imaging Science Subsystem
JPL	Jet Propulsion Laboratory
MARSIS	Mars Advanced Radar for Subsurface and Ionosphere Sounding
MRO	Mars Reconnaissance Orbiter
PWA	Permittivity, Wave and Altimetry
RADAR	Titan Radar Mapper
REASON	Radar for Europa Assessment and Sounding: Ocean to Near-surface
RH	relative humidity
SAR	Synthetic Aperture Radar
SHARAD	Shallow Radar
TM	Traceability Matrix
VIMS	Visual and Infrared Mapping Spectrometer
VLA	very large array

REFERENCES

Disclaimer: The partial list of references below corresponds with in-text references indicated in this report. For all other Cassini references, refer to Attachment B – References & Bibliographies; Attachment C – Cassini Science Bibliographies; the sections entitled References contributed by individual Cassini instrument and discipline teams located in Volume 1 Sections 3.1 and 3.2 Science Results; and other resources outside of the Cassini Final Mission Report.

Aharonson, O., A. G. Hayes, J. I. Lunine, R. D. Lorenz, M. D. Allison, C. Elachi, (2009), An asymmetric distribution of lakes on Titan as a possible consequence of orbital forcing, Nature Geoscience, 2(12):851.

Andreotti, B., A. Fourriere, F. Ould-Kaddour, B. Murray, P. Claudin, (2009), Giant aeolian dune size determined by the average depth of the atmospheric boundary layer, Nature, 457(7233):1120.

Artemieva, N., J. I. Lunine, (2005), Numerical calculations of the longevity of impact oases on Titan, Icarus, 173:243–253.

Artemieva, N., J. Lunine, (2003), Cratering on Titan: Impact melt, ejecta, and the fate of surface organics, Icarus, 164:471–480.

Atreya, S. K., (2010), Atmospheric moons Galileo would have loved, in Galileo's Medicean Moons - Their Impact on 400 Years of Discovery, Chapter 16, Cambridge University Press, pp. 130–140.

Baillié, K., J. E. Colwell, J. J. Lissauer, L. W. Esposito, M. Sremčević, (2011), Waves in Cassini UVIS stellar occultations: 2. The C ring, Icarus, 216(1):292–308.

Barnes, J. W., C. Sotin, J. M. Soderblom, et al., (2014), Cassini/VIMS observes rough surfaces on Titan's Punga mare in specular reflection, Planetary Science, 3(17), doi: 10.1186/ s13535-014- 0 0 03-4.

Barnes, J. W., B. J. Buratti, E. P. Turtle, J. Bow, P. A. Dalba, J. Perry, R. H. Brown, S. Rodriguez, S. Le Mouélic, K. H. Baines, C. Sotin, R. D. Lorenz, M. J. Malaska, T. B. McCord, R. N. Clark, R. Jaumann, P. O. Hayne, P. D. Nicholson, J. M. Soderblom, L. A. Soderblom, (2013), Precipitation-induced surface brightenings seen on Titan by Cassini VIMS and ISS, Planetary Science, 2(1), doi: 10.1186/2191-2521-2-1.

Barnes, J. W., J. Bow, J. Schwartz, R. H. Brown, J. M. Soderblom, A. G. Hayes, G. Vixie, S. Le Mouelic, S. Rodriguez, C. Sotin, R. Jaumann, K. Stephan, L. A. Soderblom, R. N. Clark, B. J. Buratti, K. H. Baines, P. D. Nicholson, (2011a), Organic sedimentary deposits in Titan's dry lakebeds: Probable evaporate, Icarus, 216:136–140.

Barnes, J. W., J. M. Soderblom, R. H. Brown, (2011b), Wave constraints for Titan's Jingpo Lacus and Kraken Mare from VIMS specular reflection lightcurves, Icarus, 211:722–731, doi: 10.1016/j.icarus.2010.09.022.

Barnes, J. W., R. H. Brown, L. Soderblom, C. Sotin, S. Le Mouelic, S. Rodriguez, R. Jaumann, R. A. Beyer, R. Clark, P. Nicholson, (2008), Spectroscopy, morphometry, and photoclinometry of Titan's dunefields from Cassini/VIMS, Icarus, 195:400–414.

Barnes, J., J. Radebaugh, R. H. Brown, S. Wall, L. Soderblom, J. Lunine, D. Burr, C. Sotin, S. Le Mouelic, S. Rodriguez, B. J. Buratti, R. Clark, K. H. Baines, R. Jaumann, P. D. Nicholson, R. L. Kirk, R. Lopes, R. Lorenz, K. Mitchell, and C. A. Wood, (2007), Near-infrared spectral mapping of Titan's mountains and channels, Journal of Geophysical Research, 112(E11006), doi: 10.1029/2007JE002932.

Barnes, J. W., R. H. Brown, J. Radebaugh, B. J. Buratti, C. Sotin, S. Le Mouelic, S. Rodriguez, E. P. Turtle, J. Perry, R. Clark, K. H. Baines, P. D. Nicholson, (2006), Cassini observations of flow-like features in western Tui Regio, Titan, Geophysical Research Letters, 33(L16204), doi: 10.1029/2006GL026843.

Barnes, J. W., R. H. Brown, E. P. Turtle, A. S. McEwen, R. D. Lorenz, M. Janssen, E. L. Schaller, M. E. Brown, B. J. Buratti, C. Sotin, C. Griffith, R. Clark, J. Perry, S. Fussner, J. Barbara, R. West, C. Elachi, A. H. Bouchez, H. G. Roe, K. H. Baines, G. Bellucci, J. -P. Bibring, F. Capaccioni, P. Cerroni, M. Combes, A. Coradini, D. P. Cruikshank, P. Drossart, V. Formisano, R. Jaumann, Y. Langevin, D. L. Matson, T. B. McCord, P. D. Nicholson, B. Sicardy, (2005), A 5-micron-bright spot on Titan: evidence for surface diversity, Science, 310:92–95, doi: 10.1126/science.1117075.

Béghin, C., O. Randriamboarison, M. Hamelin, E. Karkoschka, C. Sotin, R. C. Whitten, J. -J. Berthelier, R. Grard, F. Simoes, (2012), Analytic theory of Titan's Schumann resonance: Constraints on ionospheric conductivity and buried water ocean, Icarus, 218:1028–1042.

Berge, G. L., S. Gulkis, (1976), Earth-based radio observations of Jupiter: millimeter to meter wave-lengths, in Jupiter, (ed.) T. Gehrels, University of Arizona Press, Tucson, pp. 621–692.

Bernard, J. -M., E. Quirico, O. Brissaud, G. Montagnac, B. Reynard, B. P. McMillan, P. Coll, M. -J. Nguyen, F. Raulin, B. Schmitt, (2006), Reflectance spectra and chemical structure of Titan's tholins: Application to the analysis of Cassini Huygens observations, Icarus, 185:301–307.

Bills, B.G., F. Nimmo, (2011), Rotational dynamics and internal structure of Titan, Icarus, 214(1):351–355.

Birch, S. P. D., A. G. Hayes, J. D. Hofgartner, (2018a), The raised rims of Titan's small lakes, 49th Lunar and Planetary Science Conference, March 19–23, 2018, The Woodlands, Texas, LPI Contribution No. 2083, id.2076.

Birch, S. P. D., A. G. Hayes, P. Corlies, E. R. Stofan, J. D. Hofgartner, R. M. C. Lopes, R. D. Lorenz, J. I. Lunine, S. M. MacKenzie, M. J. Malaska, C. A. Wood, (2018b), Morphological evidence that Titan's southern hemisphere basins are paleoseas, Icarus, 310:140–148.

Birch, S. P. D., A. G. Hayes, W. E. Dietrich, A. D. Howard, C. S. Bristow, M. J. Malaska, J. M. Moore, M. Mastrogiuseppe, J. D. Hofgartner, D. A. Williams, O. L. White, (2017), Geomorphologic mapping of Titan's polar terrains: Constraining surface processes and landscape evolution, Icarus, 282:214–236.

- - - - - - - - - - - - - -

Black, B. A., J. T. Perron, D. Hemingway, E. Bailey, F. Nimmo, H. Zebker, (2017), Global drainage patterns and the origins of topographic relief on Earth, Mars, and Titan, Science, 356:727–731.

Black, B. A., J. T. Perron, D. M. Burr, S. A. Drummond, (2012), Estimating erosional exhumation on Titan from drainage network morphology, Journal of Geophysical Research: Planets, 117(E08006).

Black, G. J., D. B. Campbell, L. M. Carter, (2007), Arecibo radar observations of Rhea, Dione, Tethys, and Enceladus, Icarus, 191:702–711.

Black, G. J., D. B. Campbell, L. M. Carter, S. J. Ostro, (2004), Radar detection of Iapetus, Science, 304:553.

Black, G. J., D. B. Campbell, P. D. Nicholson, (2001), Icy Galilean satellites: Modeling radar reflectivities as a coherent backscattering effect, Icarus, 151:167–180.

Bohren, C., D. R. Huffman, (1983), Absorption and scattering of light by small particles, John Wiley & Sons.

Bolton, S. J., A. Adriani, V. Adumitroaie, M. Allison, J. Anderson, S. Atreya, J. Bloxham, S. Brown, J. E. P. Connerney, E. DeJong, W. Folkner, (2017), Jupiter's interior and deep atmosphere: The initial pole-to-pole passes with the Juno spacecraft, Science, 356(6340):821–825.

Brassé, C., O. Munoz, P. Coll, F. Raulin, (2015), Optical constants of Titan aerosols and their tholins analogs: Experimental results and modeling/observational data, Planetary and Space Science, 109–110(159–174).

Brown, R. H., J. W. Barnes, H. J. Melosh, (2011), On Titan's Xanadu region, Icarus, 214:556–560.

Brown, R. H., L. A. Soderblom, J. M. Soderblom, R. N. Clark, R. Jaumann, J. W. Barnes, C. Sotin, B. Buratti, K. H. Baines, P. D. Nicholson, (2008), The identification of liquid ethane in Titan's Ontario Lacus, Nature, 454:607–610, doi: 10.1038/nature 07100.

Brown, R. H., K. H. Baines, G. Bellucci, J. -P. Bibring, B. J. Buratti, F. Capaccioni, et al., (2004), The Cassini Visual And Infrared Mapping Spectrometer (VIMS) investigation, Space Science Reviews, 115:111–168, doi: 10.1007/s11214-004-1453-x.

Buratti, B. J., C. Sotin, K. Lawrence, R. H. Brown, S. Le Mouélic, J. M. Soderblom, et al., (2012), A newly discovered impact crater in Titan's Senkyo Cassini VIMS observations and comparison with other impact features, Planetary and Space Science, 60:18–25.

Buratti, B. J., M. D. Hicks, K. A. Tryka, M. S. Sittig, R. L. Newburn, (2002), High-resolution 0.33–0.92 μm spectra of Iapetus, Hyperion, Phoebe, Rhea, Dione, and D-type asteroids: how are they related?, Icarus, 155:375–381.

Buratti, B. J., J. A. Mosher, P. D. Nicholson, C. A. McGhee, R. G. French, (1998), Near-infrared photometry of the Saturnian satellites during ring plane crossing, Icarus, 136:223–231.

Burr, D. M., N. T. Bridges, J. R. Marshall, J. K. Smith, B. R. White, J. P. Emery, (2015), Higher-than-predicted saltation threshold wind speeds on Titan, Nature, 517(7532):60.

Burr, D. M., S. A. Drummond, R. Cartwright, B. A. Black, J. T. Perron, (2013), Morphology of fluvial networks on Titan: Evidence for structural control, Icarus, 226:742–759.

Burr, D. M., R. E. Jacobsen, D. L. Roth, C. B. Phillips, K. L. Mitchell, D. Viola, (2009), Fluvial network analysis on Titan: Evidence for subsurface structures and west-to-east wind flow, southwestern Xanadu, Geophysical Research Letters, 36(L22203).

Burr, D. M., J. P. Emery, R. D. Lorenz, G. C. Collins, P. A. Carling, (2006), Sediment transport by liquid surficial flow: Application to Titan, Icarus, 181:235–242.

Čadek, O., G. Tobie, T. Van Hoolst, M. Massé, G. Choblet, A. Lefèvre, G. Mitri, R. -M. Baland, M. Behounková, O. Bourgeois, A. Trinh, (2016), Enceladus's internal ocean and ice shell constrained from Cassini gravity, shape, and libration data, Geophysical Research Letters, 43, 5653–5660.

Campbell, D. B., G. J. Black, L. M. Carter, and S. J. Ostro, (2003), Radar evidence for liquid surfaces on Titan, Science, 302:431–434.

Cartwright, R., J. A. Clayton, R. L. Kirk, (2011), Channel morphometry, sediment transport, and implications for tectonic activity and surficial ages of Titan basins, Icarus, 214(2):561–570.

Castillo-Rogez, J. C., J. I. Lunine, (2010), Evolution of Titan's rocky core constrained by Cassini observations, Geophysical Research Letters, 37(L20205), doi: 10.1029/2010GL044398.

Charnay, B., E. Barth, S. Rafkin, C. Narteau, S. Lebonnois, S. Rodriguez, S. C. Du Pont, A. Lucas, (2015), Methane storms as a driver of Titan's dune orientation, Nature Geoscience, 8(5):362.

Charnay, B., F. Forget, G. Tobie, C. Sotin, R. Wordsworth, (2014), Titan's past and future: 3D modeling of a pure nitrogen atmosphere and geological implications, Icarus, 241:269–279.

Charnay, B., S. Lebonnois, (2012), Two boundary layers in Titan's lower troposphere inferred from a climate model, Nature Geoscience, 5(2):106–109.

Charnoz, S. et al., (2009), Origin and evolution of Saturn's ring system, in Saturn after Cassini-Huygens, (eds.) M. K. Dougherty, L. W. Esposito, S. M. Krimigis, Springer-Verlag Press, pp. 537–576.

Choukroun, M., S. Sotin, (2012), Is Titan's shape caused by its meteorology and carbon cycle?, Geophysical Research Letters, 39(L04201), doi: 10.1029/2011GL050747.

Clark, R. N., J. M. Curchin, J. W. Barnes, R. Jaumann, L. Soderblom, D. P. Cruikshank, R. H. Brown, S. Rodriguez, J. Lunine, K. Stephan, T. M. Hoefen, (2010), Detection and mapping of hydrocarbon deposits on Titan, Journal of Geophysical Research: Planets, 115(E10), doi: 10.1029/2009JE003369.

Clark, R. N., et al., (1986), Surface composition of natural satellites, in Satellites, (eds.) J. Burns, M.S. Mathews, University of Arizona Press, Tucson, pp. 437–491.

- - - - - - - - - - - - - -

Collins, G. C., (2005), Relative rates of flucial bedrock incision on Titan and Earth, Geophysical Research Letters, 32(22), CiteID L22202.

Colwell, J. E., et al., (2009), The structure of Saturn's rings, in Saturn From Cassini-Huygens, (eds.) M. K. Dougherty, L. W. Esposito, S. M. Krimigis, Springer-Verlag Press, pp. 375–412.

Cook-Hallett, C., J. W. Barnes, S. A. Kattenhorn, T. Hurford, J. Radebaugh, B. Stiles, M. Beuthe, (2015), Global contraction/expansion and polar lithospheric thinning on Titan from patterns of tectonism, Journal of Geophysical Research: Planets, 120(6):1220–1236.

Cooper, J. F., R. E. Johnson, B. H. Mauk, H. B. Garrett, N. Gehrels, (2001), Energetic ion and electron irradiation of the icy Galilean satellites, Icarus, 149(1):133–159.

Cordier, D., F. García-Sánchez, D. N. Justo-García, G. Liger-Belair, (2017), Bubble streams in Titan's seas a product of liquid N_2 +CH_4 + C_2H_6 cryogenic mixture, Nature Astronomy, 1:1–4, doi: 10.1038/s415550017-0102.

Cordier, D., O. Mousis, J. I. Lunine, S. Lebonnois, P. Rannou, P. Lavvas, L. Q. Lobo, A. G. M. Ferreira, (2012), Titan's lakes chemical composition: Sources of uncertainties and variability, Planetary and Space Science, 61(1):99–107.

Cordier, D., O. Mousis, J. I. Lunine, P. Lavvas, V. Vuitton, (2009), An estimate of the chemical composition of Titan's lakes, The Astrophysical Journal, 707(L128–L131), doi: 10.1088/0004-637X/707/2/L128.

Corlies, P., A. G. Hayes, S. P. D. Birch, R. D. Lorenz, B. Stiles, R. L. Kirk, V. Poggiali, H. Zebker, L. Iess, (2017), Titan's topography and shape at the end of the Cassini mission, Geophysical Research Letters, 44:11754–1176.

Cornet, T., C. Fleurant, B. Signovert, D. Cordier, O. Bourgois, S. Le Mouélic, S. Rodriguez, A. Lucas, (2017), Landscape formation through dissolution on Titan: A 3D landscape evolution model, Lunar and Planetary Science 2017, abstract 1835.

Cornet, T., D. Cordier, T. Le Bahers, O. Bourgeois, C. Fleurant, S. Le Mouélic, N. Altobelli, (2015), Dissolution on Titan and on Earth: Toward the age of Titan's karstic landscapes, Journal of Geophysical Research: Planets, 120:1044–1074, doi: 10.1002/2014JE004738.

Cornet, T., O. Bourgeois, S. Le Mouélic, S. Rodriguez, T. Lopez Gonzalez, C. Sotin, G. Tobie, C. Fleurant, J. W. Barnes, R. H. Brown, (2012), Geomorphological significance of Ontario Lacus on Titan: Integrated interpretation of Cassini VIMS, ISS and RADAR data and comparison with the Etosha Pan (Namibia), Icarus, 218(2):788–806.

Cottini, V., C. A. Nixon, D. E. Jennings, R. de Kok, N. A. Teanby, P. G. J. Irwin, F. M. Flasar, (2012), Spatial and temporal variations in Titan's surface temperatures from Cassini CIRS observations, Planetary Space Science, 60(1):62–71, doi: 10.1016/j.pss.2011.03.015.

Courrech du Pont, S., C. Narteau, X. Gao, (2014), Two modes for dune orientation, Geology, doi: 10.1130/G35657.1.

Crow-Willard, E. N., R. T. Pappalardo, (2015), Structural mapping of Enceladus and implications for formation of tectonized regions, Journal of Geophysical Research: Planets, 120:928–950.

- - - - - - - - - - - - - -

Cruikshank, D. P., J. F. Bell, M. J. Gaffey, R. H. Brown, R. Howell, C. Beerman, M. Rognstad, (1983), The dark side of Iapetus, Icarus, 53:90–104.

Cuzzi, J. N., et al., (2014), Utilitarian opacity model for aggregate particles in protoplanetary nebulae and exoplanet atmospheres, The Astrophysical Journal Supplement, 210(2), article id. 21.

Cuzzi, J. N., et al., (2009), Ring particle composition and size distribution, in Saturn From Cassini-Huygens, (eds.) M. K. Dougherty, L. W. Esposito, S. M. Krimigis, Springer-Verlag Press, pp. 459.

Cuzzi, J. N., P. R. Estrada, (1998), Compositional evolution of Saturn's rings due to meteoroid bombardment, Icarus, 132:1–35.

Cuzzi, J. N., et al., (1984), Saturn’s rings: Properties and processes; in Planetary Rings, (eds.) R. Greenberg, A. Brahic, University of Arizona Press, Tucson.

Cuzzi, J. N., J. B. Pollack, A. L. Summers, (1980), Saturn's rings - Particle composition and size distribution as constrained by observations at microwave wavelengths, II - Radio interferometric observations, Icarus, 44:683–705.

Dalle, O., et al., (2012), Infrared spectroscopic characterization of the low-albedo materials on Iapetus, Icarus, 221(2):735–743.

Davies, M. E., T. R. Colvin, P. G. Rogers, P. W. Chodas, W. L. Sjogren, E. L. Akim, V. A. Stepaniants, Z. P. Vlasova, A. I. Zakharov, (1992), The rotation period, direction of the North Pole, and geodetic control network of Venus, Journal of Geophysical Research, 97(E8):13,141–13,151.

Davies, M. E., et al., (1989), Report of the IAU/IAG/COSPAR working group on cartographic coordinates and rotational elements of the planets and satellites, Celestial Mechanics and Dynamical Astronomy, 46:187–204.

de Pater, I., J. R. Dickel, (1991), Multifrequency radio observations of Saturn at ring inclination angles between 5 and 26 degrees, Icarus, 94:474.

de Pater, I., (1990), Radio images of the planets, Annual Review of Astronomy and Astrophysics, 28:347–399.

de Pater, I., R. A. Brown, J. R. Dickel, (1984), VLA observations of the Galilean satellites, Icarus, 57:93–101.

de Pater, I., J. R. Dickel, (1982), VLA observations of Saturn at 1.3, 2, and 6 cm, Icarus, 50(1):88–102.

Deveraj, K., (2011), The centimeter- and millimeter-wavelength ammonia absorption spectra under Jovian conditions, Ph.D. thesis, Georgia Institute of Technology, Atlanta.

Dones, L., et al., (1993), Voyager photometry of Saturn’s A-ring, Icarus, 105:184–215.

Dougherty, M. K., et al., (2009), Saturn from Cassini-Huygens, Springer-Verlag Press.

- - - - - - - - - - - - - -

Dunn, D. E., et al., (2005), High-Quality BIMA-OVRO images of Saturn and its rings at 1.3 and 3 millimeters, The Astronomical Journal, 129:1109.

Dunn, D. E., et al., (2002), More microwave observations of Saturn: Modeling the ring with a Monte Carlo radiative transfer code, Icarus, 160:132.

Durisen R. H., P. W. Bode, J. N. Cuzzi, S. E. Cederbloom, B. W. Murphy, (1992), Ballistic transport in planetary ring systems due to particle erosion mechanisms. II - Theoretical models for Saturn's A- and B-ring inner edges, Icarus, 100(2):364–393, doi.org/10.1016/0019-1035(92)90106-H.

Elachi, C., M. D. Allison, L. Borganelli, P. Encrenaz, E. Im, M. A. Janssen, W. T. K. Johnson, R. L. Kirk, R. D. Lorenz, J. I. Lunine, D. O. Muhleman, S. J. Ostro, G. Picardi, F. Posa, C. G. Rapley, L. E. Roth, S. Seu, L. A. Soderblom, S. Vetrella, S. D. Wall, C. A. Wood, H. A. Zebker, (2004), RADAR: The Cassini Titan radar mapper, Space Science Reviews, 115(1–4):71–110.

Elachi, C., et al., (2005), Cassini Radar Views the Surface of Titan, Science, 308:970–974.

Elliot J. P., L. W. Esposito, (2011), Regolith depth growth on an icy body orbiting Saturn and evolution of bidirectional reflectance due to surface composition changes, Icarus, 212.

Esposito, L. W., et al., (1984), Saturn’s rings: Structure, dynamics, and particle properties, in Saturn, (eds.) T. Gehrels, M. Matthews, University of Arizona Press, Tucson.

Estrada, P. R., et al., (2015), Combined structural and compositional evolution of planetary rings due to micrometeoroid impacts and ballistic transport, Icarus, 252:415–439.

Ewing, R. C., A. G. Hayes, A. Lucas, (2015), Sand dune patterns on Titan controlled by long-term climate cycles, Nature Geoscience, 8(1):15–19.

Fletcher, L. N., K. H. Baines, T. W. Momary, A. P. Showman, P. G. J. Irwin, G. S. Orton, M. Roos-Serote, C. Merlet, (2011), Saturn’s tropospheric composition and clouds from Cassini/VIMS 4.6–5.1 μm nightside spectroscopy, Icarus, 214:510–533.

French, R. G., P. D. Nicholson, (2000), Saturn's rings II. Particle sizes inferred from stellar occultation data, Icarus, 145:502–523.

Fryberger, S. G., G. Dean, (1979), Dune forms and wind regime, in A study of global sand seas, (ed.) E. D. McKee, U.S. Geological Survey Professional Paper, 1052:137–169.

Glein, C. R., E. L. Shock, (2013), A geochemical model of non-ideal solutions in the methane-ethane-propane-nitrogen-actylene system on Titan, Geochemica et Cosmochimica Acta, 115:217–240, doi: 10.1016/j.gca.2013.03.030.

Goldstein, R. M., R. R. Green, (1980), Ganymede: Radar surface characteristics, Science, 207:179–180.

Greeley, R., J. D. Iversen, (1987), Wind as a geological process: on Earth, Mars, Venus and Titan, Vol. 4, Cambridge University Press.

Griffith, C. A., L. Doose, M. G. Tomasko, P. F. Penteado, C. See, (2012), Radiative transfer analyses of Titan's tropical atmosphere, Icarus, 218(2):975–988.

- - - - - - - - - - - - - -

Grima, C., M. Mastrogiuseppe, A. G. Hayes, S. D. Wall, R. D. Lorenz, J. D. Hofgartner, B. C. Stiles, C. Elachi, the Cassini RADAR Team, (2017), Surface roughness of Titan's hydrocarbon seas, Earth and Planetary Science Letters, 474:20–24.

Grossman, A. W., (1990), Microwave imaging of Saturn's deep atmosphere and rings, Ph.D. thesis, California Institute of Technology, Pasadena.

Grossman, A. W., D. O. Muhleman, G. L. Berge, (1989), High resolution microwave observations of Saturn, Science, 245:1211–1215.

Gulkis, S., et al., (2015), Subsurface properties and early activity of comet 67P/Churyumov-Gerasimenko, Science, 347(6220), doi: 10.1126/science.aaa0709.

Gulkis, S., et al., (2007), MIRO: Microwave instrument for Rosetta Orbiter, Space Science Reviews, 128-1:561–597.

Gulkis, S., R. Poynter, (1972), Thermal radio emission from Jupiter and Saturn, Physics of the Earth and Planetary Interiors, 6:36–43.

Gulkis, S., T. R. McDonough, H. Craft, (1969), The microwave spectrum of Saturn, Icarus, 10:421.

Güttler, C., et al., (2010), The outcome of protoplanetary dust growth: pebbles, boulders or planetesimals? I. Mapping the zoo of laboratory collision experiments, Astronomy & Astrophysics, 513, id.A56.

Hagfors, T., I Dahlstrom, T. Gold, S. -E. Hamran, R. Hansen, (1997), Refraction scattering in the anomalous reflections from icy surfaces, Icarus, 130:313–322.

Hagfors, T., T. Gold, H. M. Ierkic, (1985), Refraction scattering as origin of the anomalous radar returns of Jupiter's satellites, Nature, 315:637–640.

Hamilton, D. P., J. A. Burns, (1994), Origin of Saturn's E ring: Self-sustained, naturally, Science, 264(5158):550–553.

Hanley, T. R., P. G. Steffes, B. M. Karpowicz, (2009), A new model of the hydrogen and helium broadened microwave opacity of ammonia based on extensive laboratory measurements, Icarus, 202:316–335.

Hapke, B., (1990), Coherent backscatter and the radar characteristics of outer planet satellites, Icarus, 88:407–417.

Harbison, R. A., et al., (2013), The smallest particles in Saturn's A and C rings, Icarus, 226(2).

Harper, J. M., G. D. McDonald, J. Dufek, M. J. Malaska, D. M. Burr, A. G. Hayes, J. McAdams, J. J. Wray, (2017), Electrification of sand on Titan and its influence on sediment transport, Nature Geoscience, 10(4):260.

Hayes, A. G., R. D. Lorenz, J. I. Lunine, (2018), A post-Cassini view of Titan's methane-based hydrologic cycle, Nature Geoscience, 11(5):306.

- - - - - - - - - - - - - -

Hayes, A. G., S. P. D. Birch, W. E. Dietrich, A. D. Howard, R. L. Kirk, V. Poggiali, M. Mastrogiuseppe, R. J. Michaelides, P. M. Corlies, J. M. Moore, et al., (2017), Topographic constraints on the evolution and connectivity of Titan's lacustrine basins, Geophysical Research Letters, 44(23):11,745–11,753.

Hayes, A. G., (2016), The lakes and seas of Titan, Annual Review of Earth and Planetary Sciences, 44:57–83.

Hayes, A. G., R. D. Lorenz, M. A. Donelan, et al., (2013), Wind driven capillary-gravity waves on Titan’s lakes: Hard to detect or non-existent?, Icarus, 225:403–412, doi: 10.1016/j.icarus.2013.04.004 .

Hayes, A. G., O. Aharonson, J. I. Lunine, R. L. Kirk, H. A. Zebker, L. C. Wye, R. D. Lorenz, E. P. Turtle, P. Paillou, G. Mitri, et al., (2011), Transient surface liquid in Titan's polar regions from Cassini, Icarus, 211(1):655–671.

Hayes, A. G., A. S. Wolf, O. Aharonson, H. Zebker, R. Lorenz, R. L. Kirk, P. Paillou, J. Lunine, L. Wye, P. Callahan, et al., (2010), Bathymetry and absorptivity of Titan's Ontario Lacus, Journal of Geophysical Research, 115(E9), citeID E09009.

Hayes, A., O. Aharonson, P. Callahan, C. Elachi, Y. Gim, R. Kirk, K. Lewis, R. Lopes, R. Lorenz, J. Lunine, et al., (2008), Hydrocarbon lakes on Titan: Distribution and interaction with a porous regolith, Geophysical Research Letters, 35(9), citeID L09204.

Hedman, M. M., P. D. Nicholson, (2016), The B-ring’s surface mass density from hidden density waves: Less than meets the eye?, Icarus, 279:109–124.

Hedman M. M., P. D. Nicholson, (2013), Kronoseismology: Using density waves in Saturn’s C ring to probe the planet’s interior, The Astronomical Journal, 146.

Hedman, M. M., et al., (2011), Saturn’s curiously corrugated C ring, Science, 332(6030).

Hemingway, D., F. Nimmo, H. Zebker, L. Iess, (2013), A rigid and weathered ice shell on Titan, Nature, 500:550–552.

Hirtzig, M., B. Bézard, E. Lellouch, A. Coustenis, C. de Bergh, P. Drossart, A. Campargue, V. Boudon, V. Tyuterev, P. Rannou, T. Cours, S. Kassi, A. Nikitin, D. Mondelain, S. Rodriguez, S. Le Mouélic, (2013), Titan’s surface and atmosphere from Cassini/VIMS data with updated methane opacity, Icarus, 226:470–486.

Hoffman, J. P., P. G. Steffes, D. R. DeBoer, (2001), Laboratory measurements of the microwave opacity of phosphine: Opacity formalism and application to the atmospheres of the outer planets, Icarus, 152:172–184.

Hofgartner, J. D., A. G. Hayes, J. I. Lunine, et al., (2016), Titan’s “Magic Islands”: Transient features in a hydrocarbon sea, Icarus, 271:338–349.

Hofgartner, J. D., A. G. Hayes, J. I. Lunine, et al., (2014a), Transient features in a Titan sea, Nature Geoscience, 7(7):493–496, doi: 10.1038/ngeo2190.

Hofgartner, J. D., D. B. Campbell, A. Hayes, J. I. Lunine, (2014b), Specular reflections from Titan's equatorial region: Solving the decade old mystery, American Geophysical Union Fall Meeting 2014, abstract P42B-06.

Hörst, S. M., (2017), Titan's atmosphere and climate, Journal of Geophysical Research: Planets, 122(3):432–482.

Howard, M., S. Bastea, L. E. Fried, B. Khare, C. P. McKay, (2009), Titans' interior chemical composition: A thermo-chemical assessment, American Astronomical Society DPS meeting #41, id.7.03.

Howett, C. J. A., J. R. Spencer, T. Hurford, A. Verbiscer, M. Segura, (2014), Thermophysical property variations across Dione and Rhea, Icarus, 241:239–247.

Howett, C. J. A., J. R. Spencer, T. A. Hurford, A. Verbiscer, M. Segura, (2012), PacMan returns: an electron-generated thermal anomaly on Tethys, Icarus, 221(2):1084–1088.

Howett, C. J. A., J. R. Spencer, P. Schenk, R. E. Johnson, C. Paranicas, T. A. Hurford, A. Verbiscer, M. Segura, (2011), A high-amplitude thermal inertia anomaly of probable magnetospheric origin on Saturn's moon Mimas, Icarus, 216:221–226.

Howett, C. J. A., J. R. Spencer, J. Pearl, M. Segura, (2010), Thermal inertia and bolometric bond albedo values for Mimas, Enceladus, Tethys, Dione, Rhea and Iapetus as derived from Cassini/CIRS measurements, Icarus, 206:573–593.

Hyodo, R., K. Ohtsuki, (2014), Collisional disruption of gravitational aggregates in the tidal environment, The Astrophysical Journal, 787:56.

Iess, L., et al., (2014), The gravity field and interior structure of Enceladus, Science, 344:78–80.

Iess, L., et al., (2012), The tides of Titan, Science, 337:457, doi: 10.1126/ Science.1219631.

Iess, L., et al., (2010), Gravity field, shape, and moment of inertia of Titan, Science, 327:1367, doi:10.1126/science.1182583.

Janssen, M. A., J. E. Oswald, S. T. Brown, S. Gulkis, S. M. Levin, S. J. Bolton, M. D. Allison, S. K. Atreya, D. Gautier, A. P. Ingersoll, J. I. Lunine, (2017), MWR: Microwave radiometer for the Juno mission to Jupiter, Space Science Reviews, 213(1–4):139–185.

Janssen, M. A., A. Le Gall, M. J. Malaska, R. M. Lopes, A. Solomonidou, R. D. Lorenz, C. D. Neish, K. L. Mitchell, J. Radebaugh, P. J. Encrenaz, M. Mastrogiuseppe, (2016), Titan's surface at 2.2-cm wavelength imaged by the Cassini RADAR radiometer: Results and interpretations through the first ten years of observation, Icarus, 270:443–459.

Janssen, M. A., A. Ingersoll, M. D. Allison, S. Gulkis, A. Laraia, K. Baines, S. Edgington, Y. Anderson, K. Kelleher, (2013), Saturn's thermal emission at 2.2-cm wavelength as imaged by the Cassini radar radiometer, Icarus, 226:522–535.

Janssen, M. A., A. Le Gall, L. C. Wye, (2011), Anomalous radar backscatter from Titan's surface?, Icarus, 212:321–328.

- - - - - - - - - - - - - -

Janssen, M. A., R. D. Lorenz, R. West, F. Paganelli, R. M. Lopes, R. L. Kirk, C. Elachi, S. D. Wall, W. T. K. Johnson, Y. Anderson, R. A. Boehmer, P. Callahan, Y. Gim, G. A. Hamilton, K. D. Kelleher, L. Roth, B. Stiles, A. Le Gall, the Cassini Radar Team, (2009), Titan's Surface at 2.2-cm wavelength imaged by the Cassini RADAR Radiometer: Calibration and first results, Icarus, 200:222–239.

Jaumann, R., R. H. Brown, K. Stephan, J. W. Barnes, L. A. Soderblom, C. Sotin, S. Le Mouélic, R. N. Clark, J. Soderblom, B. J. Buratti, et al., (2008), Fluvial erosion and post-erosional processes on Titan, Icarus, 197(2):526–538.

Jennings, D. E., et al., (2016), Surface temperatures on Titan during northern winter and spring, The Astrophysical Journal Letters, 816(L17).

Jennings, D. E., F. M. Flasar, V. G. Kunde, R. E. Samuelson, J. C. Pearl, C. A. Nixon, R. C. Carlson, A. A. Mamoutkine, J. C. Brasunas, E. Guandique, R. K. Achterberg, (2009), Titan's surface brightness temperatures, The Astrophysical Journal Letters, 691(2):L103.

Johnson, T. V., J. I. Lunine, (2005), Saturn's moon Phoebe as a captured body from the outer solar system, Nature, 435(7038).

Karkoschka, E., A. McEwen, J. Perry, (2017), Creating the best global mosaic of Titan's surface albedo using cassini Images, American Astronomical Society Division for Planetary Sciences Meeting, abstract #49, 301.06.

Kempf, S., U. Beckmann, J. Schmidt, (2010), How the Enceladus dust plume feeds Saturn's E ring, Icarus, 206(2):446–457.

Kirchoff, M., P. Schenk, (2015), Dione's resurfacing history as determined from a global impact crater database, Icarus, 256:78–89.

Kirk, R. L., E. Howington-Kraus, A. G. Hayes, R. M. C. Lopes, R. D. Lorenz, J. I. Lunine, K. L. Mitchell, E. R. Stofan, S. D. Wall, (2010), La Sotra y los otros: Topographic evidence for (and against) cryovolcanism on Titan, Eos: Transactions American Geophysical Union, 91(52), abstract P22A-03.

Klein, M. J., S. Gulkis, (1978), Jupiter's atmosphere: Observations and interpretation of the microwave spectrum near 1.25-cm wavelength, Icarus, 35:44–60.

Kofman, W., A. Herique, Y. Barbin, J. P. Barriot, V. Ciarletti, S. Clifford, P. Edenhofer, C. Elachi, C. Eyraud, J. P. Goutail, E. Heggy, (2015), Properties of the 67P/Churyumov-Gerasimenko interior revealed by CONSERT radar, Science, 349(6247), aab0639.

Korycansky, D. G., K. J. Zahnle, (2005), Modeling crater populations on Venus and Titan, Planetary and Space Science, 53:695–710.

Langhans, M. H., R. Jaumann, K. Stephan, R. H. Brown, B. J. Buratti, R. N. Clark, K. H. Baines, P. D. Nicholson, R. D. Lorenz, L. A. Soderblom, et al., (2012), Titan's fluvial valleys: Morphology, distribution, and spectral properties, Planetary and Space Science, 60(1):34–51.

Lanzerotti, L. J., W. L. Brown, K. J. Marcantonio, R. E. Johnson, (1984), Production of ammonia-depleted surface layers on the Saturnian satellites by ion sputtering, Nature, 312:139–140.

Laraia, A. L., A. P. Ingersoll, M. A. Janssen, S. Gulkis, F. A. Oyafuso, M. D Allison, (2013), Analysis of Saturn's thermal emission at 2.2-cm wavelength: Spatial distribution of ammonia vapor, Icarus, 226:641–654.

Le Gall, A., C. Leyrat, M. A. Janssen, G. Choblet, G. Tobie, O. Bourgeois, A. Lucas, C. Sotin, C. Howett, R. Kirk, R. D. Lorenz, (2017), Thermally anomalous features in the subsurface of Enceladus's south polar terrain, Nature Astronomy, 1(4):0063.

Le Gall, A., M. J. Malaska, R. D. Lorenz, M. A. Janssen, T. Tokano, A. G. Hayes, M. Mastrogiuseppe, J. I. Lunine, G. Veyssière, P. Encrenaz, O. Karatekin, (2016), Composition, seasonal change and bathymetry of Ligeia Mare, Titan, derived from its microwave thermal emission, Journal of Geophysical Research: Planets, 121:233–251.

Le Gall, A., C. Leyrat, M. A. Janssen, S. Keihm, L. C. Wye, R. West, R. D. Lorenz, F. Tosi, (2014), Iapetus' near surface thermal emission modeled and constrained using Cassini RADAR radiometer microwave observations, Icarus, 241:221–238.

Le Gall, A., A. G. Hayes, R. Ewing, M. A. Janssen, J. Radebaugh, C. Savage, P. Encrenaz, the Cassini RADAR Team, (2012), Latitudinal and altitudinal controls on Titan's dune field morphometry, Icarus, 217:231–242.

Le Gall, A., M. A. Janssen, L. C. Wye, A. G. Hayes, J. Radebaugh, C. Savage, H. Zebker, R. D. Lorenz, J. I. Lunine, R. L. Kirk, R. M. C. Lopes, S. Wall, P. Callahan, E. R. Stofan, T. Farr, the Cassini Radar Team, (2011), Cassini SAR, radiometry, scatterometry and altimetry observations of Titan's dune fields, Icarus, 213:608–624.

Le Gall, A., M. A. Janssen, P. Paillou, R. D. Lorenz, S. D. Wall, the Cassini RADAR Team, (2010), Radar-bright channels on Titan, Icarus, 207:948–958.

Le Mouelic, S., P. Paillou, M. A. Janssen, J. W. Barnes, S. Rodriguez, C. Sotin, R. H. Brown, K. H., Baines, B. J. Buratti, R. N. Clark, M. Crapeau, P. J. Encrenaz, R. Jaumann, D. Geudtner, F. Paganelli, L. Soderblom, G. Tobie, S. Wall, (2008), Mapping and interpretation of Sinlap crater on Titan using Cassini VIMS and RADAR data, Journal of Geophysical Research, 113(E04003), doi: 10.1029/2007JE002965.

Lellouch, E., R. Moreno, T. Müller, S. Fornasier, P. Santos-Sanz, A. Moullet, M. Gurwell, J. Stansberry, R. Leiva, B. Sicardy, B. Butler, (2017), The thermal emission of Centaurs and trans-Neptunian objects at millimeter wavelengths from ALMA observations, Astronomy & Astrophysics, 608:A45.

Lellouch, E., (2006), Titan's zoo of clouds, Science, 311:186–187.

Lemmon, M. T., E. Karkoschka, M. Tomasko, (1993), Titan's rotation – Surface feature observed, Icarus, 103(2):329–332.

Lewis, J. S., (1971), Satellites of the outer planets: Their physical and chemical nature, Icarus, 15:174–185.

Li, C., A. P. Ingersoll, (2015), Moist convection in hydrogen atmospheres and the frequency of Saturn's giant storms, Nature Geoscience, 8:398–403, doi: 10.1038/ngeo2405.

- - - - - - - - - - - - - -

Liu, Z. Y. -C., J. Radebaugh, R. A. Harris, E. H. Christiansen, C. D. Neish, R. L. Kirk, R. D. Lorenz, the Cassini RADAR Team, (2016a), The tectonics of Titan: Global structural mapping from Cassini RADAR, Icarus, 270:14–29.

Liu, Z. Y. -C., J. Radebaugh, R. A. Harris, E. H. Christiansen, S. Rupper, (2016b), Role of fluids in the tectonic evolution of Titan, Icarus, 270:2–13.

Lopes, R. M.C., S. D. Wall, C. Elachi, et al., (2019), Titan as revealed by the Cassini Radar, Space Science Review, 215(33), doi: 10.1007/s11214-019-0598-6.

Lopes, R. M. C., M. J. Malaska, A. Solomonidou, A. LeGall, M. A. Janssen, C. Neish, E. P. Turtle, S. P. D. Birch, A. G. Hayes, J. Radebaugh, A. Coustenis, A. Schoenfeld, B. W. Stiles, R. L. Kirk, K. L. Mitchell, E. R. Stofan, K. J. Lawrence, the Cassini RADAR Team, (2016), Nature, distribution, and origin of Titan's undifferentiated plains ("blandlands"), Icarus, 270:162–182.

Lopes, R. M. C., R. L. Kirk, K. L. Mitchell, A. LeGall, J. W. Barnes, A. Hayes, J. Kargel, L. Wye, J. Radebaugh, E. R. Stofan, M. Janssen, C. Neish, S. Wall, C. A. Wood, J. I. Lunine, M. Malaska, (2013), Cryovolcanism on Titan: New results from Cassini RADAR and VIMS, Journal of Geophysical Research: Planets, 118:1–20, doi: 10.1002/jgre.20062.

Lopes, R. M. C., E. R. Stofan, R. Peckyno, J. Radebaugh, K. L. Mitchell, G. Mitri, C. A. Wood, R. L. Kirk, S. D. Wall, J. I. Lunine , A. Hayes , R. Lorenz, T. Farr, L. Wye, J. Craig, R. J. Ollerenshaw, M. Janssen, A. LeGall, F. Paganelli, R. West, B. Stiles, P. Callahan, Y. Anderson, P. Valora, L. Soderblom, the Cassini RADAR Team, (2010), Distribution and Interplay of geologic processes on Titan from Cassini RADAR data, Icarus, 205:540–588, doi: 10.1016/j.icarus.2009.08.010.

Lopes, R. M. C., K. L. Mitchell, E. R. Stofan, J. I. Lunine, R. Lorenz, F. Paganelli, R. L. Kirk, C. A. Wood, S. D. Wall, L. E. Robshaw, A. D. Fortes, C. D. Neish, J. Radebaugh, E. Reffet, S. J. Ostro, C. Elachi, M. D. Allison, Y. Anderson, R. Boehmer, G. Boubin, P. Callahan, P. Encrenaz, E. Flamini, G. Francescetti, Y. Gim, G. Hamilton, S. Hensley, M. A. Janssen, W. T. K. Johnson, K. Kelleher, D. O. Muhleman, G. Ori, R. Orosei, G. Picardi, F. Posa, L. E. Roth, R. Seu, S. Shaffer, L. A. Soderblom, B. Stiles, S. Vetrella, R. D. West, L. Wye, H. A. Zebker, (2007), Cryovolcanic features on Titan's surface as revealed by the Cassini Titan radar mapper, Icarus, 186:395–412.

Lora, J. M., J. I. Mitchell, (2015), Titan's asymmetric lake distribution mediated by methane transport due to atmospheric eddies, Geophysical Research Letters, 42(15):6213–6220.

Lora, J. M., J. I. Lunine, J. L. Russell, A. G. Hayes, (2014), Simulations of Titan's paleoclimate, Icarus, 243:264–273.

Lorenz, R. D., E. P. Turtle, J. W. Barnes, M. G. Trainer, D. S. Adams, K. E. Hibbard, C. Z. Sheldon, K. Zacny, P. N. Peplowski, D. J. Lawrence, M. A. Ravine, (2018), Dragonfly: a Rotorcraft Lander Concept for scientific exploration at Titan, Johns Hopkins APL Technical Digest.

Lorenz, R. D., (2014), Physics of saltation and sand transport on Titan: A brief review, Icarus, 230:162–167.

Lorenz, R. D., J. R. Zimbelman, (2014), Dune worlds: How windblown sand shapes planetary landscapes, Springer Science & Business Media.

Lorenz, R.D., B. W. Stiles, O. Aharonson, A. Lucas, A. G. Hayes, R. L. Kirk, H. A. Zebker, E. P. Turtle, C. D. Neish, E. R. Stofan, J. W. Barnes, (2013), A global topographic map of Titan, Icarus, 225(1):367–377.

Lorenz, R. D., P. Claudin, B. Andreotti, J. Radebaugh, T. Tokano, (2010), A 3 km atmospheric boundary layer on Titan indicated by dune spacing and Huygens data, Icarus, 205(2):719–721.

Lorenz, R. D., J. Radebaugh, (2009), Global pattern of Titan's dunes: Radar survey from the Cassini prime mission, Geophysical Research Letters, 36(3).

Lorenz, R. D., B. Stiles, R. L. Kirk, M. Allison, P. Persi del Marmo, L. Iess, J. I. Lunine, S. J. Ostro S. Hensley, (2008a), Titan's rotation reveals an internal ocean and changing zonal winds, Science, 319:1649–1651.

Lorenz, R. D., K. L. Mitchell, R. L. Kirk, A. G. Hayes, H. A. Zebker, P. Paillou, J. Radebaugh, J. I. Lunine, M. A. Janssen, S. D. Wall, R. M. Lopes, B. Stiles, S. Ostro, G. Mitri, E. R. Stofan, the Cassini RADAR Team, (2008b), Titan’s Inventory of Organic Surface Materials, Geophysical Research Letters, 35(L02206), doi: 10.1029/2007GL032118.

Lorenz, R. D., R. M. Lopes, F. Paganelli, J. I. Lunine, R. L. Kirk, K. L. Mitchell, L. A. Soderblom, E. R. Stofan, G. Ori, M. Myers, H. Miyamoto, J. Radebaugh, B. Stiles, S. D. Wall, C. A. Wood, the Cassini RADAR Team, (2008c), Fluvial channels on Titan: Initial Cassini RADAR observations, Planetary and Space Science, 56:1132–1144.

Lorenz, R. D., C. A. Wood, J. I. Lunine, S. D. Wall, R. M. Lopes, K. L. Mitchell, F. Paganelli, Y. Z. Anderson, L. Wye, C. Tsai, H. Zebker, E. R. Stofan, (2007), Titan's young surface: Initial impact crater survey by Cassini RADAR and model comparison, Geophysical Research Letters, 34(L07204).

Lorenz, R. D., S. Wall, J. Radebaugh, G. Boubin, E. Reffet, M. Janssen, E. Stofan, R. Lopes, R. Kirk, C. Elachi, J. Lunine, (2006), The sand seas of Titan: Cassini RADAR observations of longitudinal dunes, Science, 312(5774):724–727.

Lorenz, R. D., C. A. Griffith, J. I. Lunine, C. P. McKay, N. O. Rennò, (2005), Convective plumes and the scarcity of Titan's clouds, Geophysical Research Letters, 32(1).

Lorenz, R. D., G. Biolluz, P. Encrenaz, M. A. Janssen, R. D. West, D. O. Muhleman, (2003), Cassini RADAR: prospects for Titan surface investigations using the microwave radiometer, Planetary and Space Science, 51(4–5):353–364.

Lorenz, R. D., (2000), Post-Cassini exploration of Titan: Science rationale and mission concepts, Journal-British Interplanetary Society, 53(7/8):218–234.

Lorenz, R. D., (1998), Preliminary measurements of the cryogenic dielectric properties of water–ammonia ices: Application to radar observations of icy satellites, Icarus, 136:344–348.

Lorenz, R. D., C. P. McKay, J. I. Lunine, (1997), Photochemically driven collapse of Titan’s atmosphere, Science, 275:642–644.

- - - - - - - - - - - - - -

Lorenz, R. D., (1996), Pillow lava on Titan: expectations and constraints on cryovolcanic processes, Planetary and Space Science, 44(9):1021–1028.

Lorenz, R. D., J. I. Lunine, (1996), Erosion on Titan: Past and present, Icarus, 196:79–91.

Lorenz, R. D., J. I. Lunine, J. A. Grier, M. A. Fisher, (1995), Prediction of aeolian features on planets: Application to Titan paleoclimatology, Journal of Geophysical Research: Planets, 100(E12):26377–26386.

Lorenz, R. D., (1993), The surface of Titan in the context of ESA's Huygens probe, ESA Journal, 17:275–292.

Lucas, A., S. Rodriguez, C. Narteau, B. Charnay, S. C. Pont, T. Tokano, A. Garcia, M. Thiriet, A. G. Hayes, R. D. Lorenz, O. Aharonson, (2014), Growth mechanisms and dune orientation on Titan, Geophysical Research Letters, 41(17):6093–6100, doi: 10.1002/2014GL060971.

Lunine, J. I., R. D. Lorenz, (2009), Rivers, lakes, dunes, and rain: Crustal processes in Titan's methane cycle, Annual Review of Earth and Planetary Sciences, 37(1):299–320.

Lunine, J. I., C. Elachi, S. D. Wall, M. A. Janssen, M. D. Allison, Y. Anderson, et al., (2008), Titan's diverse landscapes as evidenced by Cassini RADAR's third and fourth looks, Icarus, 195:415–433.

Lunine, J. I., R. D. Lorenz, W. K. Hartmann, (1998), Some speculations on Titans past, present and future, Planetary and Space Science, 46(9–10):1099–1107.

MacKenzie, S. M., J. W. Barnes, C. Sotin, J. M. Soderblom, S. Le Mouélic, S. Rodriguez, K. H. Baines, B. J. Buratti, R. N. Clark, P. D. Nicholson, T. B. McCord, (2014), Evidence of Titan's climate history from evaporite distribution, Icarus, 243:191–207.

Malaska, M. J., R. M. C. Lopes, K. L. Mitchell, J. Radebaugh, T. Verlander, A. Schoenfeld, (2017a), Classification of labyrinth terrains on Titan, Lunar and Planetary Science Conference, abstract 2406.

Malaska, M. J., R. Hodyss, J. I. Lunine, A. G. Hayes, J. D. Hofgartner, G. Hollyday, R. D. Lorenz, (2017b), Laboratory measurements of nitrogen dissolution in Titan lake fluids, Icarus, 289:94–105, doi: 10.1016/j.icarus.2017.01.033.

Malaska, M. J., R. M. Lopes, A. G. Hayes, J. Radebaugh, R. D. Lorenz, E. P. Turtle, (2016a), Material transport map of Titan: The fate of dunes, Icarus, 270:183–196, doi: 10.1016/j.icarus.2015.09.029.

Malaska, M. J., R. M. C. Lopes, D. A. Williams, C. D. Neish, A. Solominidou, J. M. Soderblom, A. M. Schoenfeld, S. P. D. Birch, A. G. Hayes, A. Le Gall, M. A., Janssen, T. G. Farr, R. D. Lorenz, J. Radebaugh, E. P. Turtle, (2016b), Geomorphological map of the Afekan Crater region, Titan: Terrain relationships in the equatorial and mid-latitude regions, Icarus, 270:130–161, doi: 10.1016/j.icarus.2016.02.021.

Malaska, M. J., R. Hodyss, (2014), Dissolution of benzene, naphthalene, and biphenyl in a simulated Titan lake, Icarus, 242:74–81, doi: 10.1016/j.icarus.2014.07.022.

Malaska, M., J. Radebaugh, K. Mitchell, R. Lopes, S. Wall, R. Lorenz, (2011a), Surface dissolution model for Titan karst, First International Planetary Cave Research Workshop, October 2011, abstract 8018.

Malaska, M., J. Radebaugh, A. Le Gall, K. Mitchell, R. Lopes, S. Wall, (2011b), High-volume meandering channels in Titan's south polar region, Lunar and Planetary Science Conference, abstract 1562.

Malaska, M., J. Radebaugh, R. Lorenz, K. Mitchell, T. Farr, E. Stofan, (2010), Identification of Karst-like terrain on Titan from valley analysis, Lunar and Planetary Science Conference, 41, abstract 1544.

Marouf, E., R. French, N. Rappaport, C. McGhee, K. Wong, F. Thomson, A. Anabtawi, (2008), Structure and physical properties of Saturn's rings from Cassini radio occultations, in Abstracts for ''Saturn after Cassini–Huygens'' Symposium, 28:113, Imperial College London, UK.

Mastrogiuseppe, M., A. G. Hayes, V. Poggiali, J. I. Lunine, R. D. Lorenz, R. Seu, A. Le Gall, C. Notarnicola, K. L. Mitchell, M. Malaska, S. P. D. Birch, (2018), Bathymetry and composition of Titan's Ontario Lacus derived from Monte Carlo-based waveform inversion of Cassini RADAR altimetry data, Icarus, 300:203–209.

Mastrogiuseppe, M., A. Hayes, V. Poggiali, R. Seu, J. I. Lunine, J. D. Hofgartner, (2016), Radar sounding using the Cassini altimeter: Waveform modeling and Monte Carlo approach for data inversion of observations of Titan's seas, IEEE Transactions on Geoscience and Remote Sensing, 54(10):5646–5656.

Mastrogiuseppe M., V. Poggiali, A. Hayes, R. Lorenz, J. Lunine, G. Picardi, R. Seu, E. Flamini, G. Mitri, C. Notarnicola, P. Paillou, H. Zebker, (2014), The bathymetry of a Titan sea, Geophysical Research Letters, 41(5):1432–1437.

Matzler C., (1998), Microwave properties of ice and snow, in Solar System Ices, (eds.) B. Schmitt, C. De Bergh, M. Festou, Astrophysics and Space Science Library, Vol. 227, Springer, Dordrecht, doi.org/10.1007/978-94-011-5252-5_10.

Mayer, C. H., T. P. McCullough, R. M. Sloanaker, (1958), Observations of Mars and Jupiter at a wave length of 3.15 cm, The Astrophysical Journal, 127:11.

McCord, T. B., G. B. Hansen, B. J. Buratti, R. N. Clark, D. P. Cruikshank, E. D'Aversa, C. A. Griffith, E. K. H. Baines, R. H. Brow, C. M. Dalle Ore, G. Filacchione, V. Formisano, C. A. Hibbitts, R. Jaumann, J. I. Lunine, R. M. Nelson, C. Sotin, the Cassini VIMS Team, (2006), Composition of Titan's surface from Cassini VIMS, Planetary and Space Science, 54(15):1524–1539, doi:10.1016/j.pss.2006.06.007.

McDonald, G. D., A. G. Hayes, R. C. Ewing, J. M. Lora, C. E. Newman, T. Tokano, A. Lucas, A. Soto, G. Chen, (2016), Variations in Titan's dune orientations as a result of orbital forcing, Icarus, 270:197–210.

Méndez-Harper, J., G. D. McDonald, J. Dufek, M. J. Malaska, D. M. Burr, A. G. Hayes, J. McAdams, J. J. Wray, (2017), The electrified sands of Titan, Nature Geoscience, 10:260–265, doi: 10.1038/ngeo2921.

- - - - - - - - - - - - - -

Meriggiola, R., L. Iess, B. W. Stiles, J. I. Lunine, G. Mitri, (2016), The rotational dynamics of Titan from Cassini RADAR images, Icarus, 275:183–192.

Mitchell, K. L., R. Hodyss, M. Choukroun, J. Molaro, A. Le Gall, (2018), Enceladus' brilliant surface 2: Rationalizing Cassini RADAR and optical remote sensing, in Lunar and Planetary Science Conference, 49.

Mitchell, J. L., J. M. Lora, (2016), The climate of Titan, Annual Review of Earth and Planetary Sciences, 44.

Mitchell, K. L., M. B. Barmatz, C. S. Jamieson, R. D. Lorenz, J. I. Lunine, (2015), Laboratory measurements of cryogenic liquid alkane microwave absorptivity and implications for the composition of Ligeia Mare, Titan, Geophysical Research Letters, 42.

Mitchell, J. L., (2008), The drying of Titan's dunes: Titan's methane hydrology and its impact on atmospheric circulation, Journal of Geophysical Research, 113(E8), citeID E08015.

Mitri, G., J. I. Lunine, M. Mastrogiuseppe, V. Poggiali, (2019), Possible explosion crater origin of small lake basins with raised rims on Titan, Nature Geoscience, 1–6.

Mitri, G., et al., (2014), Shape, topography, gravity anomalies and tidal deformation of Titan, Icarus, 236:169–177.

Mitri, G., M. T. Bland, A. P. Showman, J. Radebaugh, B. Stiles, R. M. C. Lopes, M. C. Rosaly, J. I. Lunine, R. T. Pappalardo, (2010), Mountains on Titan: Modeling and observations, Journal of Geophysical Research, 115(E10), citeID E10002.

Mohammed, P., (2004), Laboratory measurements of the W band (3.2 mm) properties of phosphine (PH_3) and ammonia (NH_3) under simulated conditions of the outer planets, Journal of Geophysical Research, 109:1–9.

Moore, J. M., A. D. Howard, A. M. Morgan, (2014), The landscape of Titan as witness to its climate evolution, Journal of Geophysical Research: Planets, 119, doi: 10.1002/2014JE004608.

Moore, J. M., R. T. Pappalardo, (2011), Titan: An exogenic world?, Icarus, 212:790–806.

Moore, J. M., A. D. Howard, (2010), Are the basins of Titan's Hotei Regio and Tui Regio sites of former low latitude seas?, Geophysical Research Letters, 37(22).

Morfill, G. E., H. Fechtig, E. Grun, C. K. Goertz, (1983), Some consequences of meteoroid impacts on Saturn’s rings, Icarus, 55:439–447.

Muhleman, D. O., G. L. Berge, (1991), Observations of Mars, Uranus, Neptune, Io, Europa, Ganymede, and Callisto at a wavelength of 2.66 mm, Icarus, 92:263–71.

Muhleman, D., A. Grossman, B. Butler, M. Slade, (1990), Radar reflectivity of Titan, Science, 248:975−980.

Neish, C. D., J. L. Molaro, J. M. Lora, A. D. Howard, R. L. Kirk, P. Schenk, et al., (2016), Fluvial erosion as a mechanism for crater modification on Titan, Icarus, 270:114–129.

- - - - - - - - - - - - - -

Neish, C. D., J. W. Barnes, C. Sotin, S. MacKenzie, J. M. Soderblom, S. Le Mouélic, et al., (2015), Spectral properties of Titan's impact craters imply chemical weathering of its surface, Geophysical Research Letters, 42:3746–3754.

Neish, C. D., R. D. Lorenz, (2014), Elevation distribution of Titan's craters suggests extensive wetlands, Icarus, 228:27–34.

Neish, C. D., R. L. Kirk, R. D. Lorenz, V. J. Bray, P. Schenk, B. W. Stiles, et al., (2013), Crater topography on Titan: Implications for landscape evolution, Icarus, 223:82–90.

Neish, C. D., R. D. Lorenz, (2012), Titan's global crater population: A new assessment, Planetary and Space Science, 60(1):26–33.

Neish, C. D., R. D. Lorenz, R. L. Kirk, L. C. Wye (2010), Radarclinometry of the sand seas of Africa's Namibia and Saturn's moon Titan, Icarus, 208:385–394.

Nicholson P. D., et al., (2008), A close look at Saturn's rings with Cassini VIMS, Icarus, 193(1).

Niemann, H. B., S. K. Atreya, J. Demick, D. Gautier, J. Haverman, D. Harpold, W. Kasprzak, J. Lunine, T. Owen, F. Raulin, (2010), Composition of Titan's lower atmosphere and simple surface volatiles as measured by the Cassini-Huygens probe gas chromatograph mass spectrometer experiment, Journal of Geophysical Research, 115(E12006).

Niemann, H. B., S. K. Atreya, S. J. Bauer, G. R. Carignan, J. E. Demick, R. L. Frost, D. Gautier, J. A. Haberman, D. N. Harpold, D. M. Hunten, G. Israel, J. I. Lunine, W. T. Kasprzak, T. C. Owen, M. Paulkovich, F. Raulin, E. Raaen, S. H. Way, (2005), Huygens Probe Gas Chromatograph Mass Spectrometer: The atmosphere and surface of Titan, Nature, doi: 10.1038/nature04122.

Nimmo, F., B. G. Bills, (2010), Shell thickness variations and the long-wavelength topography of Titan, Icarus, 208:896–904.

Nixon, C. A., R. D. Lorenz, R. K. Achterberg, A. Buch, P. Coll, R. N. Clark, R. Courtin, A. Hayes, L. Iess, R. E. Johnson, R. M. C. Lopes, (2018), Titan's cold case files-Outstanding questions after Cassini-Huygens, Planetary and Space Science, 155:50–72.

Northrup, D., J. Radebaugh, E. H. Christiansen, S. Tass, L. Kerber, (2018), Yardang and dune classification on Titan through length, width, and sinuosity, Lunar and Planetary Science Conference, 49.

Ostro, S. J., R. D. West, L. C. Wye, H. A. Zebker, M. A. Janssen, B. Stiles, K. Kelleher, Y. Z. Anderson, R. A. Boehmer, P. Callahan, Y. Gim, G. A. Hamilton, W. T. K. Johnson, C. Veeramachaneni, R. D. Lorenz, the Cassini Radar Team, (2010), New Cassini RADAR results for Saturn's icy satellites, Icarus, 206:498–506.

Ostro, S. J., R. D. West, M. A. Janssen, R. D. Lorenz, H. A. Zebker, G. J. Black, J. I. Lunine, L. C. Wye, R. M. Lopes, S. D. Wall, C. Elachi, L. Roth, S. Hensley, K. Kelleher, G. A. Hamilton, Y. Gim, Y. Z. Anderson, R. A. Boehmer, W. T. K. Johnson, (2006), Cassini RADAR observations of Enceladus, Tethys, Dione, Rhea, Iapetus, Hyperion, and Phoebe, Icarus, 183(2):479-490.

- - - - - - - - - - - - - -

Ostro, S. J., 1993, Planetary radar astronomy, Reviews of Modern Physics, 65:1235–1279.

Paganelli, F., M. A. Janssen, R. M. Lopes, E. Stofan, S. D. Wall, R. D. Lorenz, J. I. Lunine, R. L. Kirk, L. Roth, C. Elachi, the Cassini Radar Team, (2008), Titan's surface from the Cassini RADAR radiometry data during SAR mode, Planetary and Space Science 56:100–108.

Paganelli, F., M. A. Janssen, B. Stiles, R. West, R. D. Lorenz, J. I. Lunine, S. D. Wall, P. Callahan, R. M. Lopes, E. Stofan, R. L. Kirk, W. T. K Johnson, L. Roth, C. Elachi, the Cassini RADAR Team, (2007), Titan's surface from the Cassini Radar SAR and high resolution radiometry data of the first five flybys, Icarus, 191:211–222.

Paillou, P., B. Seignovert, J. Radebaugh, S. Wall, (2016), Radar scattering of linear dunes and mega-yardangs: Application to Titan, Icarus, 270:211–221.

Paillou, P., D. Bernard, J. Radebaugh, R. Lorenz, A. Le Gall, T. Farr, (2014), Modeling the SAR backscatter of linear dunes on Earth and Titan, Icarus, 230:208–214.

Paillou, P., J. I. Lunine, G. Ruffié, P. Encrenaz, S. D. Wall, R. D. Lorenz, M. A. Janssen, (2008a), Microwave dielectric constant of Titan-relevant materials, Geophysical Research Letters, 35(L18202).

Paillou, P., K. L. Mitchell, S. D. Wall, G. Ruffié, C. A. Wood, R. D. Lorenz, E. R. Stofan, J. I. Lunine, R. M. Lopes, P. Encrenaz, (2008b), Microwave dielectric constant of liquid hydrocarbons: Application to the depth estimation of Titan's lakes, Geophysical Research Letters, 35(L05202).

Paillou, P., M. Crapeau, C. Elachi, S. Wall, P. Encrenaz, (2006), Models of SAR backscattering for bright flows and dark spots on Titan, Journal of Geophysical Research, 111(E11011), doi: 10.1029/2006JE002724.

Peake, W. H., (1959), Interaction of electromagnetic waves with some natural surfaces, IRE Transactions on Antennas and Propagation, 7:324–329.

Perron, J. T., M. P. Lamb, C. D. Koven, I. Y. Fung, E. Yager, M. Adamkovics, (2006), Valley formation and methane precipitation rates on Titan, Journal of Geophysical Research, 111(E11001).

Poggiali, V., M. Mastrogiuseppe, A. G. Hayes, R. Seu, S. P. D. Birch, R. Lorenz, C. Grima, J. D. Hofgartner, (2016), Liquid-filled canyons on Titan, Geophysical Research Letters, 43:7887–7894.

Porco, C. C., J. W. Weiss, D. C. Richardson, L. Dones, T. Quinn, H. Throop, (2008), Simulations of the dynamical and light-scattering behavior of Saturn's rings and the derivation of ring particle and disk properties, The Astronomical Journal, 136(5):2172.

Porco, C. C., et al., (2006), Cassini observes the active south pole of Enceladus, Science, 311:1393–1401.

Porco, C. C., E. Baker, J. Barbara, K. Beurle, A. Brahic, J. A. Burns, S. Charnoz, N. Cooper, D. D. Dawson, A. D. Del Genio, T. Denk, L. Dones, U. Dyudina, M. W. Evans, S. Fussner, B. Giese, K. Grazier, P. Helfenstein, A. P. Ingersoll, R. A. Jacobson, T. V. Johnson,

A. McEwen, C. D. Murray, G. Neukum, W. M. Owen, J. Perry, T. Roatsch, J. Spitale, S. Squyres, P. Thomas, M. Tiscareno, E. P. Turtle, A. R. Vasavada, J. Veverka, R. Wagner. R. West, (2005), Imaging of Titan from the Cassini spacecraft, Nature, 434:159–168, doi: 10.1038/nature03436.

Porco, C. C., R. A. West, S. Squyres, A. McEwen, P. Thomas, C. D. Murray, A. Del Genio, A. P. Ingersoll, T. V. Johnson, G. Neukum, et al., (2004), Cassini Imaging Science: Instrument characteristics and anticipated scientific investigations at Saturn, Space Science Reviews, 115(1–4):363–497, doi: 10.1007/s11214-004-1456-7.

Poulet, F., et al., (2003), Compositions of Saturn's rings A, B, and C from high resolution near-infrared spectroscopic observations, Astronomy and Astrophysics, 412:305–316.

Poulet, F., J. N. Cuzzi, (2002), The composition of Saturn's rings, Icarus, 160:350–358.

Radebaugh, J., R. C. Lewis, B. Bishop, E. H. Christiansen, L. Kerber, S. Rodriguez, C. Narteau, A. A. Le Gall, A. Lucas, M. Malaska, (2017), Aeolian landscapes of Titan from Cassini RADAR reveal winds, elevation constraints and sediment characteristics, American Geophysical Union Fall Meeting Abstracts.

Radebaugh, J., D. Ventra, R. D. Lorenz, T. Farr, R. Kirk, A. Hayes, M. J. Malaska, S. Birch, Z. Y. -C. Liu, J. Lunine, J. Barnes, A. Le Gall, R. Lopes, E. Stofan, S. Wall, P. Paillou, (2016), Alluvial and fluvial fans on Saturn's moon Titan reveal processes, materials and regional geology, in Geology and Geomorphology of Alluvial and Fluvial Fans: Terrestrial and Planetary Perspectives, (eds.) D. Ventra, L. E. Clarke, Geological Society, London, Special Publications, 440, doi: 10.1144/SP440.6.

Radebaugh, J., (2013), Dunes on Saturn's moon Titan at the end of the Cassini Equinox Mission, Aeolian Research, 11:23–41.

Radebaugh, J., R. D. Lorenz, S. D. Wall, R. L. Kirk, C. A. Wood, J. I. Lunine, E. R. Stofan, R. M. C. Lopes, P. Valora, T. G. Farr, A. G. Hayes, B. Stiles, G. Mitri, H. Zebker, M. Janssen, L. Wye, A. Le Gall, K. L. Mitchell, F. Paganelli, R. D. West, E. L. Schaller, the Cassini RADAR Team, (2011), Regional geomorphology and history of Titan's Xanadu province, Icarus, 211:672–685.

Radebaugh, J., R. Lorenz, T. Farr, P. Paillou, C. Savage, C. Spencer, (2010), Linear dunes on Titan and Earth: Initial remote sensing comparisons, Geomorphology 121:122–132, doi: 10.1016/j.geomorph.2009.02.022.

Radebaugh, J., R. Lorenz, J. Lunine, S. Wall, G. Boubin, E. Reffet, R. Kirk, R. Lopes, E. Stofan, L. Soderblom, M. Allison, M. Janssen, P. Paillou, P. Callahan, the Cassini RADAR Team, (2008), Dunes on Titan observed by Cassini RADAR, Icarus, 194:690–703, doi: 10.1016/j.icarus.2007.10.015.

Radebaugh, J., R. Lorenz, R. Kirk. J. Lunine, E. Stofan, R. Lopes, S. Wall, the Cassini RADAR Team, (2007), Mountains on Titan observed by Cassini Radar, Icarus, 192:77–91, doi: 10.1016/j.icarus.2007.06.020.

Rannou, P., F. Montmessin, F. Hourdin, S. Lebonnois, (2006), The latitudinal distribution of clouds on Titan, Science, 311(5758):201–205.

Raulin, F., (1987), Organic chemistry in the oceans of Titan, Advances in Space Research, 7(5):71–81.

Reffet, E., S. Courrech du Pont, P. Hersen, S. Douady, (2010), Formation and stability of transverse and longitudinal sand dunes, Geology, 38:491–494.

Reh, K., (2007), Titan and Enceladus $1B mission feasibility study report, JPL D-37401 B.

Richardson, L. A., J. W. Hartwig, J. W. Leachman, (2018), Fluid phase equilibria, 462:38–43, doi: 10.1016/j.fluid.2018.01.023.

Ries, P. A., M. A. Janssen, (2015), A large-scale anomaly in Enceladus microwave emission, Icarus, 257:88–102.

Rignot, E., (1995), Backscatter model for the unusual radar properties of the Greenland ice sheet, Journal of Geophysical Research, 100(E5):9389–9400.

Rignot, E., S. J. Ostro, J. J. Van Zyl, K. C. Jezek, (1993), Unusual radar echoes from the Greenland ice sheet, Science, 261:1710–1713.

Robbins, S. J., et al., (2010), Estimating the masses of Saturn's A and B rings from high-optical depth N-body simulations and stellar occultations, Icarus, 206:431–445.

Rodriguez, S., A. Garcia, A. Lucas, T. Appéré, A. Le Gall, E. Reffet, L. Le Corre, S. Le Mouélic, T. Cornet, S. Courrech du Pont, C. Narteau, O. Bourgeois, J. Radebaugh, K. Arnold, J. W. Barnes, K. Stephan, R. Jaumann, C. Sotin, R. H. Brown, R. D. Lorenz, E. P. Turtle, (2014), Global mapping and characterization of Titan's dune fields with Cassini: Correlation between RADAR and VIMS observations, Icarus, 230:168–179.

Roe, H. G., I. de Pater, S. G. Gibbard, B. A Macintosh, C. E. Max, E. F. Young, M. E. Brown, A. H. Bouchez, (2004), A new 1.6 micron map of Titan's surface, Geophysical Research Letters, 31(L17S03).

Rubin, D. M., P. A. Hesp, (2009), Multiple origins of linear dunes on Earth and Titan, Nature Geoscience, 2(9):653.

Sagan, C., S. F. Dermott, (1982), The tide in the seas of Titan, Nature, 300:731–733.

Savage, C. J., J. Radebaugh, E. H. Christiansen, R. D. Lorenz, (2014), Implications of dune pattern analysis for Titan's surface history, Icarus, 230:180–190.

Sayanagi, K., U. A. Dyudina, S. P. Ewald, G. Fischer, A. P. Ingersoll, W. S. Kurth, G. D. Muro, C. C. Porco, R. A. West, (2013), Dynamics of Saturn's great storm of 2010–2011 from Cassini ISS and RPWS, Icarus, 223:460–478.

Schaller, E. L., M. E. Brown, H. G. Roe, A. H. Bouchez, (2006), A large cloud outburst at Titan's south pole, Icarus,182(1):224–229.

Schenk, P., D. P. Hamilton, R. E. Johnson, W. B. McKinnon, C. Paranicas, J. Schmidt, M. R. Showalter, (2011), Plasma, plumes and rings: Saturn system dynamics as recorded in global color patterns on its midsize icy satellites, Icarus, 211(1):740-–57.

Schenk, P. M., J. M. Moore, (2009), Eruptive volcanism on saturn's icy moon Dione, Lunar and Planetary Science Conference, 40.

Schloerb, F. P., D. O. Muhleman, G. L. Berge, (1979), Interferometric observations of Saturn and its rings at a wavelength of 3 3.71 cm, Icarus, 39(2):214–231.

Schurmeier, L. R., A. J. Dombard, (2018), Crater relaxation on Titan aided by low thermal conductivity sand infill, Icarus, 305:314–323.

Schurmeier, L., A. J. Dombard, J. Radebaugh, M. Malaska, (2018), Intrusive and extrusive cryovolcanism and the composition of Titan’s icy crust, Lunar and Planetary Science Conference, 49, abstract 2934.

Schurmeier, L., A. J. Dombard, M. Malaska, J. Radebaugh, (2017), Are Titan’s radial labyrinth terrains surface expressions of large laccoliths?, American Geophysical Union Fall Meeting, New Orleans.

Scipioni, F., F. Tosi, K. Stephan, G. Filacchione, M. Ciarniello, F. Capaccioni, P. Cerroni, the VIMS Team, (2014), Spectroscopic classification of icy satellites of Saturn II: Identification of terrain units on Rhea, Icarus, 234:1–16.

Scipioni, F., F. Tosi, K. Stephan, G. Filacchione, M. Ciarniello, F. Capaccioni, P. Cerroni, the VIMS Team, (2013), Spectroscopic classification of icy satellites of Saturn I: Identification of terrain units on Dione, Icarus, 226(2):1331–1349.

Sears, W. D., (1995), Tidal dissipation in oceans on Titan, Icarus, 113:39–56.

Sears, W. D., (1992), Tidal dissipation and the giant impact origin for the Moon, Lunar and Planetary Science Conference, 23.

Sierks, H., et al., (2015), On the nucleus structure and activity of comet 67P/Churyumov-Gerasimenko, Science, 347(6220).

Smith, P. H., M. T. Lemmon, R. D. Lorenz, L. A. Sromovsky, J. J. Caldwell, M. D. Allison, (1996), Titan's surface, revealed by HST imaging, Icarus, 119(2):336–349.

Soderblom, J. M., J. W. Barnes, R. H. Brown, V. Chevrier, K. Farnsworth, L. A. Soderblom, (2016), Evidence for frozen hydrocarbons on Titan, American Astronomical Society, DPS meeting #48, id.502.04.

Soderblom, J. M., R. H. Brown, L. A. Soderblom, J. W. Barnes, R. Jaumann, S. Le Mouélic, C. Sotin, K. Stephan, K. H. Baines, B. J. Buratti, R. N. Clark, (2010), Geology of the Selk crater region on Titan from Cassini VIMS observations, Icarus, 208(2):905–912.

Soderblom, L. A., R. H. Brown, J. M. Soderblom, J. W. Barnes, R. L. Kirk, C. Sotin, R. Jaumann, D. J. Mackinnon, D. W. Mackowski, K. H. Baines, B. J. Buratti, (2009), The geology of Hotei Regio, Titan: correlation of Cassini VIMS and RADAR, Icarus, 204(2):610–618.

- - - - - - - - - - - - - -

Soderblom, L., J. Anderson, K. Baines, J. Barnes, J. Barrett, R. Brown, B. Buratti, R. Clark, D. Cruikshank, C. Elachi, M. Janssen, R. Jaumann, R. Kirk, E. Karkoschka, S. Lemouelic, R. Lopes, R. Lorenz, J. Lunine, T. McCord, P. Nicholson, J. Radebaugh, B. Rizk, C. Sotin, E. Stofan, T. Sucharski, M. Tomasko, S. Wall, (2007), Correlations between Cassini VIMS spectra and RADAR SAR images: Implications for Titan's surface composition and the character of the Huygens Probe landing site, Planetary and Space Science, 55:2025–2036.

Sohl, F., A. Solomonidou, F. W. Wagner, A. Coustenis, H. Hussmann, D. Schulze-Makuch, (2014), Tidal stresses on Titan and implications for its geology and habitability, Journal of Geophysical Research, 119:1013–1036.

Sohl, F., H. Hussmann, B. Schwentker, T. Spohn, R. D. Lorenz, (2003), Interior structure models and tidal Love numbers of Titan, Journal of Geophysical Research, 108(E12):5130, doi: 10.1029/2003JE002044.

Solomonidou, A., A. Coustenis, R. M. Lopes, M. J. Malaska, S. Rodriguez, P. Drossart, C. Elachi, B. Schmitt, S. Philippe, M. Janssen, M. Hirtzig, (2018), The spectral nature of Titan's major geomorphological units: constraints on surface composition, Journal of Geophysical Research: Planets, 123(2):489–507.

Solomonidou, A., A. Coustenis, M. Hirtzig, S. Rodriguez, K. Stephan, R. M. C. Lopes, P. Drossart, C. Sotin, S. Le Mouélic, K. Lawrence, E. Bratsolis, R. Jaumann, R. H. Brown, (2016), Temporal variations of Titan's surface with Cassini/VIMS, Icarus, 270:85–99.

Solomonidou, A., et al., (2014), Surface albedo spectral properties of geologically interesting areas on Titan, Journal of Geophysical Research, 119:1729–1747.

Sotin, C., R. Jaunmann, B. J. Buratti, R. H. Brown, R. N. Clark, L. A. Soderblom, K. H. Baines, G. Bellucci, J. -P. Bribing, F. Capaccioni, P. Cerroni, A. Coradini, D. P. Cruikshank, P. Drossart, V. Formisano, Y. Langevin, D. L. Matson, T. B. McCord, R. M. Nelson, P. D. Nicholson, B. Sicardy, S. LeMouelic, S. Rodriguez, K. Stephan, C. K. Scholz, (2005), Release of volatiles from a possible cryovolcano from near-infrared imaging of Titan, Nature, 435:786–789.

Spencer, J. R., A. C. Barr, L. W. Esposito, P. Helfenstein, A. P. Ingersoll, R. Jaumann, C. P. McKay, F. Nimmo, J. H. Waite, (2009), Enceladus: An active cryovolcanic satellite, in Saturn from Cassini-Huygens,, Springer, Dordrecht, pp. 683–724.

Spencer, J. R., J. C. Pearl, M. Segura, F. M. Flasar, A. Mamoutkine, P. Romani, B. J. Buratti, A. R. Hendrix, L. J. Spilker, R. M. C. Lopes, (2006), Cassini encounters Enceladus: Background and the discovery of a south polar hot spot, Science, 311(5766):1401–1405.

Stephan, K., et al., (2010), Specular reflection on Titan: Liquids in Kraken Mare, Geophysical Research Letters, 37(L07104), doi: 10.1029/2009GL042312.

Stiles, B., R. Kirk, R. Lorenz, S. Hensley, E. Lee, S. Ostro, M. Allison, P. Callahan, Y. Gim, L. Iess, P. Perci del Marmo, G. Hamilton, W. Johnson, R. West, the Cassini RADAR Team, (2010), Determining Titan's spin State from Cassini radar images, The Astronomical Journal, 139(1):311.

Stiles, B. W., S. Hensley, Y. Gim, D. M. Bates, R. L. Kirk, A. Hayes, J. Radebaugh, R. D. Lorenz, K. L. Mitchell, P. S. Callahan, H. Zebker, W. T. K. Johnson, S. D. Wall, J. I. Lunine, C. A. Wood, M. Janssen, F. Pelletier, R. D. West, C. Veeramacheneni, (2009), Determining Titan surface topography from Cassini SAR data, Icarus, 102:584–598, doi: 10.1016/j.icarus.2009.03.032.

Stiles, B. W., R. L. Kirk, R. D. Lorenz, S. Hensley, E. Lee, S. J. Ostro, M. D. Allison, P. S. Callahan, Y. Gim, L. Iess, (2008), Determining Titan's spin state from Cassini radar images, The Astronomical Journal, 135(5).

Stofan, E. R., C. Elachi, J. I. Lunine, R. D. Lorenz, B. Stiles, K. L. Mitchell, S. Ostro, L. Soderblom, C. Wood, H. Zebker, S. Wall, M. Janssen, R. Kirk, R. Lopes, F. Paganelli, J. Radebaugh, L. Wye, Y. Anderson, M. Allison, R. Boehmer, P. Callahan, P. Encrenaz, E. Flamini, G. Francescetti, Y. Gim, G. Hamilton, S. Hensley, W. T. K. Johnson, K. Kelleher, D. Muhleman, P. Paillou, G. Picardi, F. Posa, L. Roth, R. Seu, S. Shaffer, S. Vetrella, R. West, (2007), The lakes of Titan, Nature, 445:61–64, doi: 10.1038/nature05438.

Stofan, E. R., J. I. Lunine, R. Lopes, F. Paganelli, R. D. Lorenz, C. A. Wood, R. Kirk, S. Wall, C. Elachi, L. A. Soderblom, S. Ostro, M. Janssen, J. Radebaugh, L. Wye, H. Zebker, Y. Anderson, M. Allison, R. Boehmer, P. Callahan, P. Encrenaz, E. Flamini, G. Francescetti, Y. Gim, G. Hamilton, S. Hensley, W. T. K. Johnson, K. Kelleher, D. Muhleman, G. Picardi, F. Posa, L. Roth, R. Seu, S. Shaffer, B. Stiles, S. Vetrella, R. West, (2006), Mapping of Titan: Results from the first Titan radar passes, Icarus, 185:443–456.

Thomas, P. C., R. Tajeddine, M. S. Tiscareno, J. A. Burns, J. Josepth, T. J. Loredo, P. Helfenstein, C. C. Porco, (2016), Enceladus’s measured physical libration requires a global subsurface ocean, Icarus, 264:37–47.

Thomas, P.C., et al., (2007), Hyperion's sponge-like appearance, Nature, 448:50–56.

Thompson, W. D., S. W. Squyres, (1990), Titan and other icy satellites: Dielectric properties of constituent materials and implications for radar sounding, Icarus, 86:336–354.

Thornton, D. D., W. J. Welch, (1963), 8.35 mm radio emission from Jupiter, Icarus, 2:228–232.

Tobie, G., J. I. Lunine, J. Monteux, O. Mousis, F. Nimmo, (2014), The origin and evolution of Titan, in Titan Interior, Surface, Atmosphere, and Space Environment, (eds.) I. Müller-Wodarg, C. A. Griffith, E. Lellouch, T. E. Cravens, Cambridge University Press, doi.org/10.1017/CBO9780511667398, pp. 29–62.

Tobie, G., J. I. Lunine, C. Sotin, (2006), Episodic outgassing as the origin of atmospheric methane on Titan, Nature, 440:61–64.

Tokano, T., (2010), Relevance of fast westerlies at equinox for the eastward elongation of Titan’s dunes, Aeolian Research, 2(2–3):113–127.

Tokano, T., (2008), Dune-forming winds on Titan and the influence of topography, Icarus, 194(1):243–262.

- - - - - - - - - - - - - -

Tokano T., (2005), Meteorological assessment of the surface temperatures on Titan: constraints on the surface type, Icarus, 173:222–42.

Tokano, T., F. M. Neubauer, (2005), Wind-induced seasonal angular momentum exchange at Titan's surface and its influence on Titan's length-of-day, Geophysical Research Letters, 32(24), doi: 10.1029/2005GL024456.

Tomasko, M., B. Archinal, T. Becker, B. Bézard, M. Bushroe, M. Combes, D. Cook, A. Coustenis, C. de Bergh, L. Dafoe, L. Doose, S. Douté, A. Eibl, S. Engel, F. Gliem, B. Grieger, K. Holso, E. Howington-Kraus, E. Karkoschka, H. Keller, R. Kirk, R. Kramm, M. Küppers, P. Lanagan, E. Lellouch, M. Lemmon, J. Lunine, E. McFarlane, J. Moores, M. Prout, B. Rizk, M. Rosiek, P. Rueffer, S. Schröder, B. Schmitt, C. See, P. Smith, L. Soderblom, N. Thomas, R. West, (2005), Rain, winds, and haze during the Huygens probe descent to Titan’s surface, Nature, 438:765–778.

Tosi, F., R. Orosei, R. Seu, A. Coradini, J. I. Lunine, G. Filacchione, A. I. Gavrishin, F. Capaccioni, P. Cerroni, A. Adriani, et al., (2010a), Correlations between VIMS and RADAR data over the surface of Titan: Implications for Titan’s surface properties, Icarus, 208(1):366–384.

Tosi, F., D. Turrini, A. Coradini, G. Filacchione, (2010b), Probing the origin of the dark material on Iapetus, Monthly Notices of the Royal Astronomical Society, 403:1113–1130.

Tsoar, H., (1983), Dynamic processes acting on a longitudinal (seif) dune, Sedimentology, 30:567–578.

Turtle, E. P., J. E. Perry, A. G. Hayes, R. D. Lorenz, J. W. Barnes, A. S. McEwen, R. A. West, A. D. Del Genio, J. M. Barbara, E. L. Schaller, T. L. Ray, J. I. Lunine, R. M. C. Lopes, E. R. Stofan, (2011), Rapid and extensive surface changes near Titan’s equator: evidence of April showers, Science, 331(1414), doi: 10.1126/science.1201063.

Turtle, E. P., J. E. Perry, A. S. McEwen, A. D. Del Genio, J. Barbara, R. A. West, D. D. Dawson, C. C. Porco, (2009), Cassini imaging of Titan's high-latitude lakes, clouds, and south-polar surface changes, Geophysical Research Letters, 36(2), citeID L02204.

Ulaby, F. T., R. K. Moore, A. K. Fung, (1982), Microwave remote sensing, active and passive, Vol. II: Radar remote sensing and surface scattering and emission theory, Addison-Wesley Publishing Company Advanced Book Program/World Science Division.

Ulaby, F. T., R. K. Moore, A. K. Fung, (1981), Microwave remote sensing active and passive-Volume I: Microwave remote sensing fundamentals and radiometry, Addison-Wesley Publishing Company Advanced Book Program/World Science Division.

van der Tak, F., et al., (1999), Time variability in the radio brightness distribution of Saturn, Icarus, 142:125.

Ventura, B., C. Notarnicola, D. Casarano, F. Posa, A. G. Hayes, L. Wye, (2012), Electromagnetic models and inversion techniques for Titan’s Ontario Lacus depth estimation from Cassini RADAR data, Icarus, 221:960–969.

Verbiscer, A. J., M. F. Skrutskie, D. P. Hamilton, (2009), Saturn’s largest ring, Nature, 461:1098.

Verbiscer, A., R. French, M. Showalter, P. Helfenstein, (2007), Enceladus: Cosmic graffiti artist caught in the act, Science, 315:815.

Vixie, G., J. W. Barnes, B. Jackson, S. Rodriguez, S. Le Mouélic, C. Sotin, S. MacKenzie, P. Wilson, (2015), Possible temperate lakes on Titan, Icarus, 257:313–323.

Wall, S., A. Hayes, C. Bristow, R. Lorenz, E. Stofan, J. Lunine, A. Le Gall, M. Janssen, R. Lopes, L. Wye, L. Soderblom, P. Paillou, O. Aharonson, H. Zebker, T. Farr, G. Mitri, R. Kirk, K. Mitchell, C. Notarnicola, D. Casarano, B. Ventura, (2010), Active shoreline of Ontario Lacus, Titan: A morphological study of the lake and its surroundings, Geophysical Research Letters, 37(L05202), doi: 10.1029/2009GL041821.

Wall, S. D., R. M. Lopes, E. R. Stofan, C. A. Wood, J. L. Radebaugh, B. W. Stiles, R. M. Nelson, L. W. Kamp, M. A. Janssen, R. L. Lorenz, J. I. Lunine, T. G. Farr, G. Mitri, P. Paillou, F. Paganelli, K. L. Mitchell, (2009), Cassini RADAR images at Hotei Arcus and Western Xanadu, Titan: Evidence for recent cryovolcanic activity, Geophysical Research Letters, 36(L04203), doi: 1029/2008GL036415.

Wei, H. Y., C. T. Russell, M. K. Dougherty, F. M. Neubauer, Y. J. Ma, (2010), Upper limits on Titan's magnetic moment and implications for its interior, Journal of Geophysical Research, 115(E10007).

West, R., K. Mitchell, B. Stiles, Y. Anderson, A. Le Gall, A. Hayes, M. Janssen, R. Kirk, R. Lopes, R. Lorenz, S. Wall, (2012), Observation design and early results from Cassini Radar SAR imaging of Enceladus, Lunar and Planetary Science Conference, 43.

Wood, C. A., (2018), Titan’s great crustal thickening event and recent geologic history, Lunar and Planetary Science Conference, 49:1343.

Wood, C. A., R. Lorenz, R. Kirk, R. Lopes, K. Mitchell, E. Stofan, (2010), Impact craters on Titan, Icarus, 206:334–344.

Wood, C. A., K. L. Mitchell, R. M. C. Lopes, J. Radebaugh, E. Stoffan, J. Lunine, the Cassini RADAR Team, (2007), Volcanic calderas in the north polar region of Titan, Lunar and Planetary Science Conference, abstract 1454.

Wrixon, G. T., W. J. Welch, (1970), The millimeter wave spectrum of Saturn, Icarus, 13(2):163–172.

Wye, L., (2011), Radar scattering from Titan and Saturn's icy satellites using the Cassini spacecraft, Ph.D. Thesis, Stanford University, Faculty of Engineering, 316.

Wye, L. C., H. A. Zebker, the Cassini RADAR Team, (2011), Backscatter analysis of Saturn's icy moons with Cassini RADAR, American Geophysical Union Fall Meeting 2011, abstract id.P11E-1624.

Wye, L. C., H. A. Zebker, R. D. Lorenz, (2009), Smoothness of Titan’s Ontario Lacus: Constraints from Cassini RADAR specular reflection data, Geophysical Research Letters, 36:16201, doi: 10.1029/2009GL039588.

Wye, L. C., H. A. Zebker, S. J. Ostro, R. D. West, Y. Gim, R. D. Lorenz, the Cassini RADAR Team, (2007), Electrical properties of Titan's surface from Cassini RADAR scatterometer measurements, Icarus, 188:367–385.

Yu, X., S. M. Hörst, C. He, N. T. Bridges, D. M. Burr, J. A. Sebree, J. K. Smith, (2017), The effect of adsorbed liquid and material density on saltation threshold: Insight from laboratory and wind tunnel experiments, Icarus, 297:97–109.

Yung, Y. L., M. Allen, J. P. Pinto, (1984), Photochemistry of the atmosphere of Titan: comparison between model and observations, The Astrophysical Journal Supplement, 55:465–506.

Zahnle, K., P. Schenk, H. Levison, L. Dones, (2003), Cratering rates in the outer solar system, Icarus, 163:263–289.

Zebker, K., Y. -Q. Wong, (2016), Shape of Titan from Cassini radar elevation measurements and implications for interior structure and composition, American Geophysical Union Fall Meeting, Dec. 12–16, San Francisco, CA, paper no. P33F-01.

Zebker, H., A. Hayes, M. Janssen, A. Le Gall, R. Lorenz, L. Wye, (2014), Surface of Ligeia Mare, Titan, from Cassini altimeter and radiometer analysis, Geophysical Research Letters, 41:308–313, doi: 10.1002/2013GL058877.

Zebker, H. A., B. Stiles, S. Hensley, R. Lorenz, R. L. Kirk, J. I. Lunine, (2009a), Size and shape of Saturn’s moon Titan, Science, 324:921–923.

Zebker, H. A., Y. Gim, P. Callahan, S. Hensley, R. D. Lorenz, the Cassini RADAR Team, (2009b), Analysis and interpretation of Cassini Titan radar altimeter echoes, Icarus, 200:240–255.

Zebker, H., L. Wye, M. Janssen, the Cassini RADAR Team, (2008), Titan's surface from reconciled Cassini microwave reflectivity and emissivity observations, Icarus, 194(2):704–710.

Zebker, H. A., E. A. Marouf, G. L. Tyler, (1985), Saturn's rings: Particle size distributions for thin layer models, Icarus, 64(3):531–548.

Zhang, Z., et al., (2017a), Cassini microwave observations provide clues to the origin of Saturn's C ring, Icarus, 281:297–321.

Zhang, Z., A. G. Hayes, M. A. Janssen, P. D. Nicholson, J. N. Cuzzi, I. de Pater, D. E. Dunn, (2017b), Exposure age of Saturn's A and B rings, and the Cassini Division as suggested by their non-icy material content, Icarus, 294:14–42.